Metamaterial Enhanced Near-Field Thermophotovoltaic Energy Conversion

by

Payam Sabbaghi

A Dissertation Presented in Partial Fulfillment
of the Requirements for the Degree
Doctor of Philosophy

Approved November 2019 by the
Graduate Supervisory Committee:

Liping Wang, Chair
Patrick Phelan
Huei-Ping Huang
Robert Wang
Hongbin Yu

ARIZONA STATE UNIVERSITY

December 2019

ABSTRACT

It is well known that radiative heat transfer rate can exceed that between two blackbodies by several orders of magnitude due to the coupling of evanescent waves. One promising application of near-field thermal radiation is thermophotovoltaic (TPV) devices, which convert thermal energy to electricity. Recently, different types of metamaterials with excitations of surface plasmon polaritons (SPPs)/surface phonon polaritons (SPhPs), magnetic polaritons (MP), and hyperbolic modes (HM), have been studied to further improve near-field radiative heat flux and conversion efficiency. On the other hand, near-field experimental demonstration between planar surfaces has been limited due to the extreme challenge in the vacuum gap control as well as the parallelism.

The main objective of this work is to experimentally study the near-field radiative transfer and the excitation of resonance modes by designing nanostructured thin films separated by nanometer vacuum gaps. In particular, the near-field radiative heat transfer between two parallel plates of intrinsic silicon wafers coated with a thin film of aluminum nanostructure is investigated. In addition, theoretical studies about the effects of different physical mechanisms such as SPhP/SPP, MPs, and HM on near-field radiative transfer in various nanostructured metamaterials are conducted particularly for near-field TPV applications. Numerical simulations are performed by using multilayer transfer matrix method, rigorous coupled wave analysis, and finite difference time domain techniques incorporated with fluctuational electrodynamics. The understanding gained here will undoubtedly benefit the spectral control of near-field thermal radiation for energy-harvesting applications like thermophotovoltaic energy conversion and radiation-based thermal management.

ACKNOWLEDGEMENTS

I am indebted to many individuals and organizations for making this research possible. First and foremost, I am deeply grateful to my advisor, Prof. Liping Wang, for the continuous support of my PhD study, his encouragement, motivation, and immense knowledge. His expertise in my research topics, his positive attitude and excellent guidance have made these past five years a memorable fruitful working experience. Beside my advisor, I am deeply grateful to the members of my dissertation committee, Dr. Patrick Phelan, Dr. Huei-Ping Huang, Dr. Robert Wang, and Dr. Hongbin Yu, for their great support and valuable advices. Sincere appreciation is also expressed to my former and current labmates Dr. Linshuang Long, Dr. Yue Yang, Dr. Jui-Yung Chang, Dr. Qing Ni, Dr. Hao Wang, Dr. Hassan Alshehri, Sydney Taylor, Xiaoyan Ying, Rajagopalan Ramesh, Lee Lambert, and Christian Messner. I benefited a lot by collaborating and interacting with them during my PhD study. I also acknowledge numerous financial grants provided by National Science Foundation and Air Force Office of Scientific Research in addition to fellowships from Arizona State University that helped me complete this dissertation.

Last but not the least, my PhD study would not have been possible without the love and encouragement of my family. I acknowledge and thank my parents, Ahmad and Homa, and my sister, Parisa, who have been always supportive of me. Most importantly, I wish to thank my wife and my best friend, Behnaz, for all the sacrifice she made for me and for all love and strength she gave me during the last six years.

TABLE OF CONTENTS

Page

LIST OF TABLES

Table Page

LIST OF FIGURES

Figure Page

CHAPTER 1

INTRODUCTION

This Chapter reviews the state-of-the-art research on near-field radiative heat transfer and its application in energy conversion systems. In Section 1.1, an overview of thermophotovoltaic systems is given. Section 1.2 looks into the fundamentals of near-field thermal radiation. Finally, the objectives of the PhD research are discussed in Section 1.3.

1.1 Overview of Thermophotovoltaic Systems

Thermophotovoltaic (TPV) system, which consists of a thermal emitter and a PV cell, is an energy conversion unit that generates electric power directly from thermal radiation, as illustrated in Fig. 1.1. The advantages of a TPV system over other energy conversion devices includes portability, absence of moving parts, low maintenance cost, and quiet operation with a great promise for aerospace, military, and civilian applications.

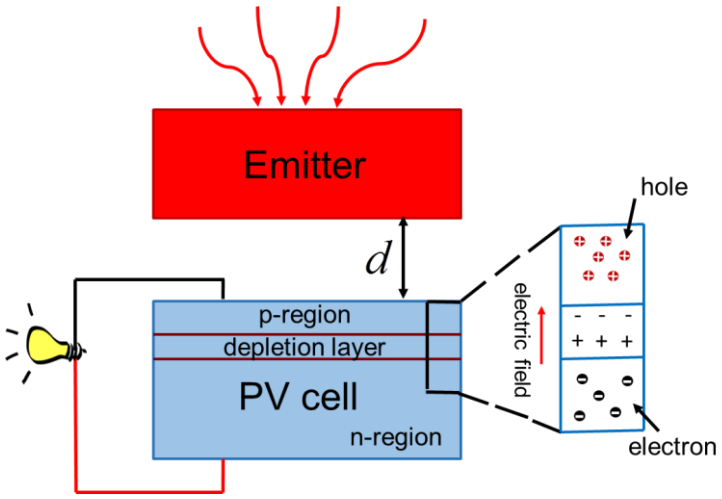

Figure 1.1 Schematic of a near-field thermophotovoltaic system and illustration of p-n junction of the semiconductor.

A TPV system typically consists of a semiconductor cell such as InGaSb, with a narrow bandgap energy (E_g) that operates on the principle of photovoltaic effect. In fact, only photons (from a high-temperature source or emitter) with energies greater than the bandgap of the semiconductor cell ($E > E_g$) can generate free electrical charges due to the creation of electron-hole pairs inside the PV cell. As a result, the enhanced absorption above the PV cell bandgap is required to improve the electrical power output and TPV performance. The main question here is whether the emission spectrum can be spectrally tuned and enhanced in order to improve the conversion efficiency of TPV devices? It should be noted that it is critical to control the spectral distributions of thermal emission and maximize the emittance in a narrow band above the bandgap energy of PV cell. Hence, tailoring the radiative properties of metamaterial selective absorbers and emitters is essential to achieve high-emittance band. A number of designs have been proposed and demonstrated for wavelength-selective TPV emitter based on surface engineering, including complex grating, 2D microcavity and photonic crystals structures[1-6]. Hence, material design, sample fabrication and experimental measurements are needed to gain a deep understanding of near-field thermal radiation between nanostructured selective metasurfaces particularly for TPV applications.

In addition, it is well known that the radiative heat flux between two bodies can be greatly enhanced in near-field regime due to the contribution of evanescent waves. In particular, the near-field radiation (NFR) enhancement could be several orders of magnitude over the blackbody limit when surface plasmon or phonon polaritons (SPPs/SPhPs) are excited. This near-field enhancement has been theoretically and

experimentally proposed to improve TPV conversion. This effect is a promising way to improve the total radiative heat flux and possibly improve the conversion efficiency.

1.2 Fundamentals of Near-Field Thermal Radiation

It is numerically and experimentally shown that the near-field radiative transfer could be greatly enhanced when the distance between two objects becomes smaller than the characteristic thermal wavelength due to resonant coupling of evanescent waves[7-11]. Hence, photon tunneling in the near-field can enhance radiative heat transfer to overcome the blackbody limit governed by Planck's law[8,12]. In particular, near-field radiative flux could far exceed the blackbody limit by the resonant coupling of surface plasmon/phonon polaritons (SPP/SPhP)[9,13-15], epsilon-near-zero/pole (ENZ/ENP) modes[16-18], and hyperbolic modes[7,19-27]. Very recently, magnetic polaritons (MP), which indicate a strong coupling of external electromagnetic waves with the magnetic resonance, have been employed to achieve spectral near-field heat flux enhancement. Potential applications of near-field radiation (NFR) include but are not limited to: near-field thermophotovoltaics[19,28-35], thermal rectification[36-38], and radiative refrigeration[39,40], which have been widely discussed in recent years. Here, the study of engineered surfaces with desired thermal radiative characteristics and employing the near-field effect in energy conversion systems are the main focus of this dissertation.

1.3 Objectives

The main objective of this PhD proposal is to study the near-field radiation and design metamaterial emitters including multilayers, and gratings in energy conversion

applications. The proposed research aims to address several fundamental questions in the following:

- How to experimentally validate the impact of near-field radiation and apply it to near-field thermophotovoltaic devices?
- How to compute the absorption distribution in a PV cell in energy harvesting applications?
- Could hyperbolic metamaterials such as multilayered and grating emitters, spectrally tune the near-field radiation and achieve enhanced conversion efficiency in thermophotovoltaic applications?
- How to enhance the efficiency of a TPV system by employing tandem cell?
- Could magnetic polaritons increase the radiative heat transfer just above the energy bandgap in thermophotovoltaic systems?
- Could magnetic polaritons be excited in polar materials such as SiC? What would be the impact of this excitation?

Two tasks are proposed to accomplish the proposed research.

1. **Modeling.** The near-field heat transfer will be predicted to investigate the impact of hyperbolic metamaterials, resonance modes, and absorption distribution in a PV cell through Rigorous Coupled-Wave Analysis (RCWA), effective medium theory (EMT) and finite-difference time-domain (FDTD) method.
2. **Measurement.** The near-field heat flux will be measured in submicron gap distances experimentally. The results are expected to confirm the theoretical computations and demonstrate the significance of the near-field radiation and its application in energy harvesting devices.

Chapter 2 provides a literature review of near-field radiation and magnetic polartions and their application in energy conversion systems. The following Chapter 3 will discuss the experimental demonstration of near-field thermal radiation. In Chapter 4, the spectrally selective radiative transfer between the multilayer emitter and PV cell is numerically studied. The application of a tandem cell in a near-field thermophotovoltaic system is also proposed for the first time. Next, Chapter 5 will study the geometry of a Drude grating emitter on the excitation of magnetic polaritons across the vacuum gap and inside the PV cell in a TPV system. The effect of magnetic polaritons excited inside the groove of SiC grating on near-field radiation will be investigated in Chapter 6. The numerical near-field radiative heat transfer between a microsphere and a planar substrate will be also discussed. Finally, Chapter 7 summarizes this PhD dissertation and recommends some future works with proposed methods and potential difficulties.

CHAPTER 2

LITERATURE REVIEW

This Chapter provides an overview of previous research on near-field radiative heat transfer and its applications. In Section 2.1, previous experimental studies exploring the effect of near-field radiative heat transfer are discussed. Section 2.2, studies the fundamentals of magnetic polaritons (MPs) and its role in near-field regime. In the end, Section 2.3 focuses on the application of near-field radiation in thermophotovoltaic systems.

2.1 Experimental Investigations of Near-Field Radiative Heat Transfer

In the near-field, contribution from evanescent waves can exceed the blackbody limit by orders of magnitude when two objects are brought within a distance smaller than the characteristic thermal wavelength[7,8,10,11,13,41,42]. Recent experimental investigations further demonstrated the near-field radiative heat flux enhancement over the blackbody limit by several order of magnitude[14,15,43,44]. In addition to evanescent waves, surface plasmon/phonon polaritons (SPP/SPhP) propagating along the interface between two media[8,41,45-47], epsilon-near-zero/pole (ENZ/ENP) modes[16-18], hyperbolic modes[7,19-27], cavity resonance[48-50], and magnetic polariton (MP)[51-56] can further increase the near-field thermal radiation.

Most reported near-field experiments used polar materials[44,57,58] whose optical phonons in the infrared greatly enhanced the near-field radiative heat transfer near room temperature due to an adequate frequency match between SPhP and Planck oscillator to demonstrate super-Planckian radiative heat transfer with different configurations and

vacuum gap distances. Atomic force microscope (AFM) tip-based techniques have also demonstrated the enhanced near-field radiation heat transfer breaking Planck's law down to 100 nm gap between a silica sphere with diameter of 50 μm and a glass microscope slide due to surface phonon polariton[11]. With plate-plate configuration, where the creation of nanometer gaps and parallelism across mesoscale lateral size is one major challenge, Hu *et al.*[13] experimentally demonstrated a near-field enhancement of 50% over blackbody limit due to SPhP coupling between two closely spaced glass plates separated by microscale polystyrene particles. Ito *et al.*[59] experimentally measured the radiative heat transfer between a pair of diced fused quartz substrates at a vacuum gap distance of 0.5 μm with a temperature differences up to 20 K. St-Gelais *et al.*[60] experimentally demonstrated a heat transfer enhancement approximately two orders of magnitude higher than the far-field limit at 100 nm gap distance between parallel SiC nanobeams with a temperature gradient of 260 K. Ghashami *et al.*[15] observed more than 40 times enhancement of thermal radiation compared to blackbody radiation when two 5×5 mm^2 quartz plates were separated by a vacuum gap distance of 200 nm and with a thermal gradient near to 156 K. Silicon has also been used for NFR measurements. For example, Shi *et al.*[61] tuned the nanoscale radiation between bulk silicon and a glass microsphere at a gap of ~60 nm by changing the carrier concentration of silicon. In addition, Lim *et al.*[62] measured the near-field thermal radiation between doped-Si parallel plates with a doping concentration of 8.33×10^{19} cm^{-3} by employing a MEMS-based platform. The near-field radiative heat transfer coefficient was found to be 2.91 times greater than the blackbody limit at a 400-nm vacuum gap. Watjen *et al.*[63] used SiO_2 posts between 1×1 cm^2 lightly doped silicon samples with a doping concentration of 2×10^{18} cm^{-3}. The largest radiative

heat flux was found to be 11 times higher than the blackbody limit at a vacuum gap distance of 200 nm, which was mainly attributed to the excitation of coupled surface plasmon polaritons. Bernardi *et al*.[64] demonstrated a radiative heat transfer enhancement of 8.1 times relative to the blackbody limit between two 5×5 mm^2 intrinsic silicon planar surfaces at a vacuum gap distance of 200 nm, which is due to the additional contribution of frustrated modes in the near-field.

The super-Planckian radiation between metals is also studied in a few experimental studies. Shen *et al*.[9] measured the enhanced thermal radiation due to the tunneling of non-resonant evanescent waves between a 50 μm diameter glass microsphere nominally coated with a 100 nm-thick gold film and a substrate coated with a thick gold film at a vacuum gap distance of 30 nm. Kralik *et al*.[65] observed a one hundred fold enhancement of the blackbody radiation when the plane-parallel tungsten layers were separated by a vacuum gap distance of 1 μm. In this work, the temperature of the cold sample was near 5 K and the temperature of the hot sample was in the range of 10-40 K. Lim *et al*. [14] measured the radiative heat flux between metallo-dielectric multilayers at a vacuum gap distance of 160 nm, achieving a net radiative heat flux more than 100 times larger than the calculated far-field value and about seven times larger than the blackbody limit due to coupled SPPs at metal-dielectric interfaces. Song *et al*.[57] also reported the near-field enhancement between silicon microdevices at a size of 48×48 μm^2 coated with 100 nm-thick gold layer. The near-field thermal conductance at a gap distance of 60 nm was found to be ~10 times larger than the blackbody limit. The plasma frequencies of metals typically occur in the ultra-violet to the visible wavelength range[66], which cannot facilitate the NFR enhancement around room temperature, therefore NFR

between metallic surfaces is much weaker than that between polar materials. In addition, metals are typically known as bad thermal emitters in the far field due to their very low emissivity of just a few percent. However, the super-Planckian radiation heat transfer, enhanced by the near-field effect is significantly greater than the far-field transfer, which can facilitate its application in many near-field heat transfer systems.

2.2 The Role of Magnetic Polaritons in Near-Field Regime

Magnetic polaritons (MPs), which account for the strong coupling of external electromagnetic waves with the magnetic resonance excited inside the nanostructure, is a powerful mechanism that can be used to achieve selective emission[2,3,67] specifically in energy conversion systems. In addition, excitation of magnetic polaritons plays a significant role in tailoring far-field radiative properties. However, it usually requires the structure of metal-insulator-metal to excite MP[53-55,67-69]. Phonon-mediated MP has also been demonstrated in polar materials according to the metallic behavior of such materials within the phonon absorption band[56]. A tunable infrared emitter was designed by covering graphene on top of SiC deep grating and exciting MP inside the grating[70]. Applying the phase transition material of vanadium dioxide, the same group also achieved a tunable thermal emitter via MP excitation for both phases[3].

Although phonon-mediated MP has been extensively applied to control far-field radiative properties[71,72], its effect on near-field radiative transport needs to be identified. Recently, the effect of MP on near-field radiative heat transfer between two metallic gratings is numerically investigated by our group[51]. Different from that work, which considered the excitation of MP within the nanometer vacuum gap between the emitter

and receiver, the effect of MP excited in the SiC grating grooves is also investigated in a numerical project[52]. Besides, the excitation of MP can enhance the heat flux absorption above the PV cell bandgap, and thus improve the conversion efficiency of a thermophotovoltaic system with micro- or nanostructured metamaterials. Hence, the spectral selectivity improvement of a TPV system via MP excitation across the vacuum gap and inside the PV cell is demonstrated by employing a Drude grating emitter and a lossless metal backside reflector[73].

2.3 Near-Field Energy Conversion Systems

Thermophotovoltaic (TPV) energy conversion system, which consists of two main components of thermal emitter and TPV cell, is a direct energy conversion process from heat to electricity through electron-hole pair generation from absorbed thermal radiation. The advantages of TPV systems including versatile thermal sources, high power output in addition to relatively huge conversion efficiency make it a suitable choice for space, civilian, industrial, military, and microelectronics applications. However, one of the major challenges for current TPV systems is to further enhance the power output and conversion efficiency. Hence, previous efforts have been made to design selective emitters for far-field TPV systems to improve the conversion efficiency. Due to the narrowband radiation, rare-earth oxides were the earliest selective emitters[74,75]. Benefiting from the improvement of micro/nanoscale fabrication technique, micro/nanostructured surfaces were also used to achieve selective emission. The grating and multilayered structures with different dimensions were considered as the most widely applicable selective emitters and filters[1,76,77]. Narayanaswamy and Chen[5] showed that a

stack of alternate tungsten and alumina layers could be applied as the selective emitter of far-field TPV systems.

On the other hand, the near-field radiation can be utilized to enhance the performance of a thermophotovoltaic (TPV) energy conversion system[29,32-35,78-81]. Whale and Cravalho[82,83] introduced the concept of a near-field TPV device in 2002 by placing the emitter and PV cell by a subwavelength distance in which blackbody emitter and extra recombination loss were considered. Laroche et al.[84] also developed a model of near-field TPV considering a tungsten emitter with TPV cell of 100% quantum efficiency. Basu et al.[28] conducted a review on the near-field TPV systems in 2007, and Park et al.[85] analyzed a near-field TPV system with plain tungsten thermal emitter, and with the consideration of energy absorption and charge transport in different regions of the TPV cell. Later, Francoeur et al.[86] investigated the thermal impacts on the performance of a near-field TPV system by solving coupled near-field thermal radiation, charge transport, and heat transport formulations in TPV cell, and concluded that the cell temperature will greatly affect the TPV performance. Bright et al.[87] studied the effect of a gold reflector added at the cell backside, which leads to enhanced conversion efficiency by reflecting the useless long-wavelength energy back to emitter. In addition, it has been theoretically studied that the performance of near-field TPV devices can be improved by using hyperbolic metamaterial emitters and the excitation of SPPs[29,88]. Recently, the metamaterials using epsilon-near-zero (ENZ) or epsilon-near-pole (ENP) have also been proposed as selective emitter[18]. Besides, the excitation of trapped optical modes in thin-film emitters and PV cells supported by backside reflectors was also numerically shown as a promising mechanism to improve the conversion efficiency of near-field TPV

systems[30]. This should be noted that the resonant coupling usually cannot be supported in near-field TPV devices due to the mismatched resonance frequencies of the emitter and PV cell. MP on the other hand, is advantageous since it does not require both the emitter and receiver to support the resonance at similar frequencies. In addition to MP, researchers have employed graphene on either the emitter or on the surface of TPV cell to tune the surface plasmon resonance frequency for better matching above the cell bandgap and thereby a higher conversion efficiency[34,89]. The Drude radiator, which supports surface polaritons in near infrared region, was also considered as the emitter of near-field TPV system for achieving quasi-monochromatic radiative heat flux[90]. Narayanaswamy and Chen[91] also presented a similar idea to improve the performance of a near-field TPV system by exciting SPhP coupling between dielectric emitter and optimized TPV cell. Tungsten nanowire based hyperbolic metamaterial emitters were also studied to improve the near-field TPV performance with supported hyperbolic modes[19]. It is also possible to match the cell bandgap by shifting the SPP resonance frequency with metamaterial emitters such as tungsten grating emitter[92] and photonic crystals[6] to obtain improved efficiency. Besides, recent theoretical studies demonstrated that rectangular gratings, nanowire and nanohole arrays can be used to tailor the spectral absorption of GaSb anti-reflection in conversion systems[93,94]. It is also theoretically shown that thermal emission, with its frequency and amplitude can be further modulated by the Fabry-Perot resonances in the dielectric layer of emitter[32].

It should be also noticed that a TPV system with a single PV junction cell cannot make an excellent use of the emitted spectrum from the thermal source. The reason is that the photons with energies less than the bandgap of PV cell cannot generate electron-hole

pairs and consequently provide the electrical energy output. In addition, each photon with higher energy can only excite one electron-hole pair meaning only one electron contributes to the current, while the rest of energy exceeding the bandgap ends up as a heat loss. Tandem cells are multiple p–n junctions made of different semiconductor materials in which each cell will produce electric current in response to the absorbed photons with energies greater than the band gap of that cell meaning a better use of the photon energies. Hence, stacking of individual PV cells into a tandem structure seems an efficient way to increase the total electrical power output and conversion efficiency mainly in solar TPV applications[95-98]. Wilt *et al.*[99] studied a monolithic interconnected modules (MIMs) by series-interconnected photovoltaic cells to reduced resistive losses, achieve higher output power density, and improve thermal coupling and ultimately higher system efficiency. In the simplest structure of a tandem cell, two PV cells are placed in a way that photons first strike the one with higher energy bandgap and photons with lower energy can pass through the first PV cell and contribute to the electron-hole pair generation in the second PV cell. Sahoo *et al.*[100] proposed an alternative approach based on a lower-bandgap GaAs/GaSb dual-junction solar cell that predicts a conversion efficiency of 54%. It should be noted that as the number of PV cells increases, the efficiency of the stack potentially increases while this efficiency improvement is achieved at the cost of increased complexity and manufacturing price. Their higher price have limited their use to specific applications such as aerospace where their high power-to-weight ratio is desirable[101]. Although tandem structures have been extensively employed in far-field TPV systems, its role on near-field TPV systems has yet to be identified.

CHAPTER 3

EXPERIMENTAL DEMONSTRATION OF SUPER-PLANCKIAN NEAR-FIELD THERMAL RADIATION WITH METALLIC SURFACES

In this Chapter, we experimentally demonstrate that the radiative heat transfer between metallic planar surfaces exceeds the blackbody limit by employing the near-field and thin-film effects. Nanosized polystyrene particles were used to create a nanometer gap between aluminum thin-films of different thicknesses coated on 5 × 5 mm^2 diced silicon chips. The experimental results are validated by theoretical calculation based on fluctuational electrodynamics. The reasonable agreement between the experimental results and theoretical prediction from fluctuational electrodynamics suggests the contribution of reduced reflectivity at the interface and SPP coupling inside the Al thin-film layers to the near-field energy transfer. Section 3.1 explains on how to prepare the samples for the near-field radiation measurement. Section 3.2 gives the near-field and far-field theoretical models and Section 3.3 discusses the experimental setup. Evaluation of heat conduction and vacuum gap determination are presented in Section 3.4 and 3.5, respectively. Finally, the near-field radiation measurement results are given in Section 3.6 and the main physical mechanisms are discussed in Section 3.7.

3.1 Sample Preparation and Characterization of Al Thin Films

First, a careful cleaning process using isopropanol alcohol, deionized water, and oxygen plasma, is needed to prepare the lightly doped Si chips (Ted Pella Inc., 1-30 ohm-cm resistivity, 500±30 μm thick) for Al deposition. Then, Al thin-films of different thicknesses were coated on 5×5 mm^2 lightly doped Si samples via an electron beam

evaporation method with the deposition rate of 0.5 Å/s. The thickness of the aluminum thin-film on silicon samples is characterized using a home-built atomic force microscope (AFM) with a resolution of 0.2 nm. The AFM scan is a two dimensional array that can precisely measure the roughness of the surface as well as the height of Al thin-film. The roughness average of silicon sample coated by Al is measured to be about 0.4 nm. The thickness of the Al layer is also measured by scanning the height of a step created on the Si sample during the Al deposition at a step size of 300 nm to confirm the high accuracy of electron beam evaporation method.

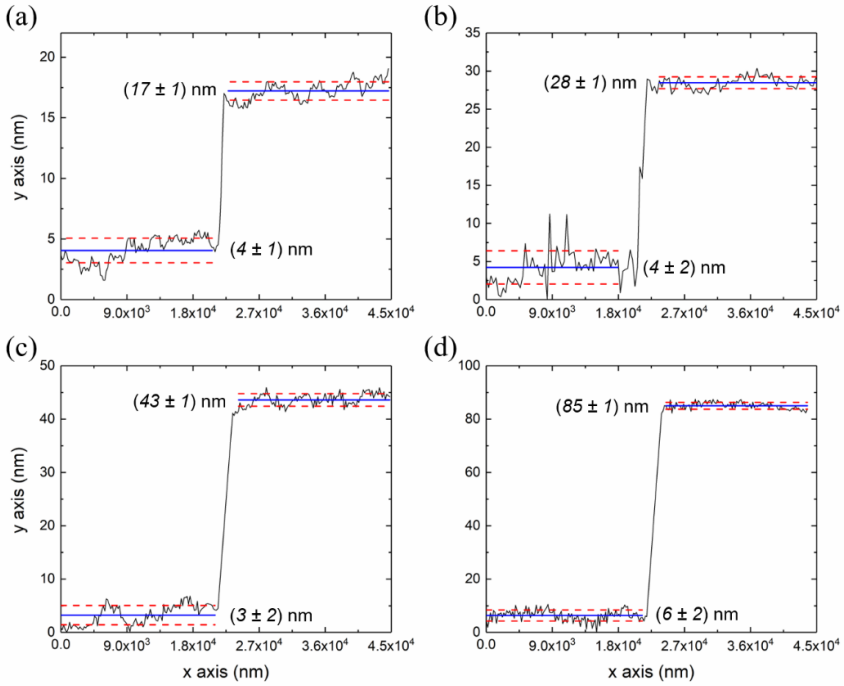

Figure. 3.1 AFM measurements to determine the height of aluminum thin-film deposited on lightly doped silicon samples with thickness of (a) 13 ± 2 nm, (b) 24 ± 3 nm, (c) 40 ± 3 nm, and (d) 79 ± 3 nm.

The thicknesses of the deposited aluminum thin-films were characterized to be 13±2 nm, 24±3 nm, 40±3 nm, and 79±3 nm by an atomic force microscope across a step

created by masking part of the sample surface on a spare Si chip during the same deposition (Fig. 3.1) along with surface roughness of 0.4 nm. The bow of the Si chip was measured to be 75±19 nm with a profilometer. Nanosized polystyrene (PS) particles were used to create a nanometer gap between aluminum thin-films of different thicknesses. The 200-nm-diameter PS particles (Sigma Aldrich with a calibrated particle diameter of 198 nm and standard deviation of 6 nm) were originally suspended in a solution of deionized water with a concentration of 2.4×10^{13} particles/mL. The suspension was sonicated at each intermediate dilution in an Elmasonic Bath Sonicator to ensure the uniformity of particle distribution. Due to a high initial concentration, nanoparticles are diluted with deionized water to ensure that only a monolayer of particles was deposited on the Si surface to minimize heat conduction between the emitter and the receiver. First, 0.02 mL of initial PS particles was diluted with 100 mL of deionized water and then, 0.1 mL of the intermediate suspension was diluted with 61 mL of deionized water. The final particle concentration was 7.8×10^{6} particles/mL. Next, 0.02 mL of the final suspension was deposited on the Si receiver using a syringe. The total number of polystyrene nano particles (PS-NP) on the substrate is estimated to be around 1.56×10^{5}. The Si receiver was then dried on a hotplate before being aligned with the Si emitter and placed in the vacuum chamber. The receiver samples were carefully inspected under an optical microscope to ensure that were no large particle aggregations before being loaded onto the experimental setup for near-field radiation measurements. The reason is that aggregate and dust particles can adversely affect the actual vacuum gap distance. For visual reference, four different locations of a lightly doped silicon sample with 200 nm-

diameter PS particles are observed under the microscope to ensure sample integrity as shown in Figs. 3.2 (a-d).

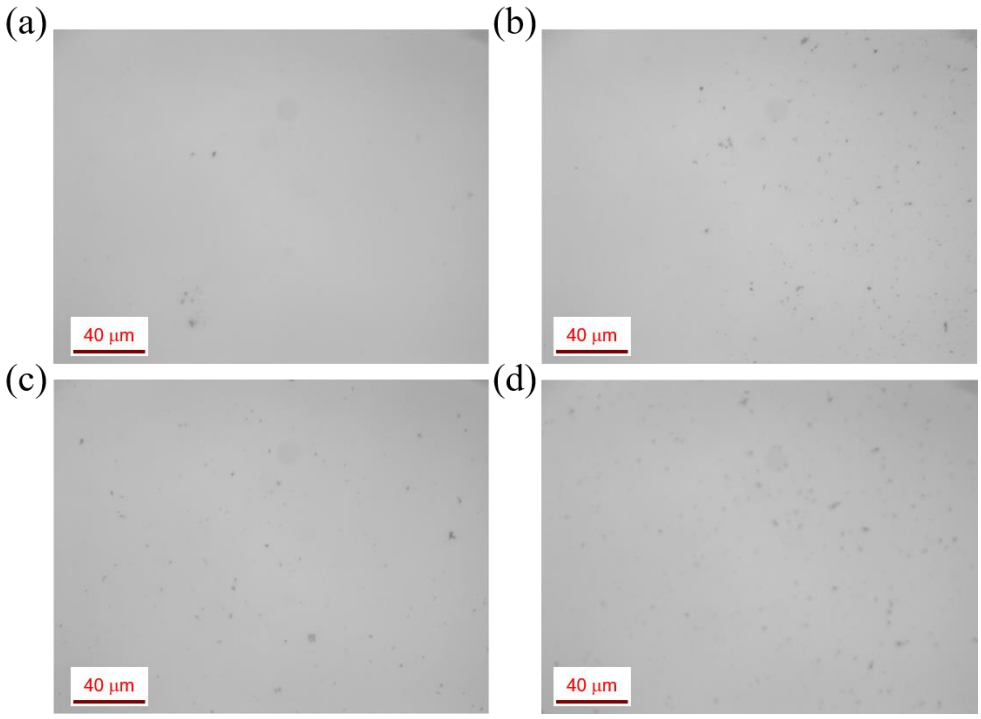

Figure 3.2 Images of prepared polystyrene nano-particles with a diameter of 200 nm over lightly doped silicon sample at locations (a) top left, (b) top right, (c) bottom left and (d) bottom right.

3.2 Theoretical Models of Radiative Heat Transfer between Al Thin Films

In this section, the optical properties of silicon sample and aluminum are presented and the theoretical near-field and far-field models are discussed. First, to verify that the Palik data[102] is a valid reference for the material properties of the Si wafers used in the near-field radiative measurements, the refraction index and the extinction coefficient are extracted from the measured radiative properties. Figs. 3.3(a) and (b) show the average spectral transmittance and reflectance (with 8° incident light) of a double-side

polished Si wafer with the same thickness and resistivity range were measured by a Fourier-transform infrared (FTIR) spectrometer in a wavelength range from 4 μm to 20 μm. Figs. 3.3(c) and (d) illustrate an excellent agreement between the extracted optical constant of lightly Si wafer using Ray-tracing method[12] and the Palik data[102] in a wavelength range from 4 μm to 20 μm.

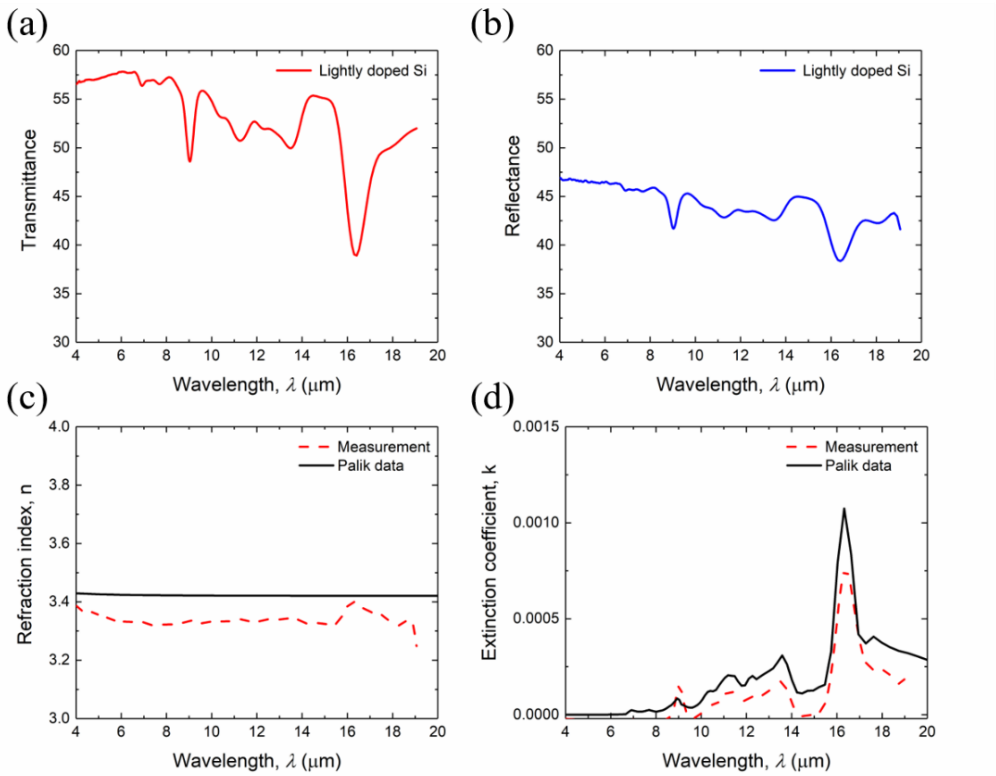

Figure 3.3 Spectral (a) reflectance and (b) transmittance of a lightly doped Si wafer measured by FTIR. (c) Refraction index and (d) extinction coefficient of a lightly doped Si wafer extracted from the measured radiative properties compared to the Palik data[102].

The refraction index (n) and extinction coefficient (k) of lightly doped silicon and aluminum are compared in Fig. 3.4 Since Palik data[102] for aluminum is not available for frequency values less than 9.4×10^{13} rad/s, the optical properties of aluminum at a given

angular frequency ω are described by a Drude model as $\varepsilon_{\text{Drude}}(\omega)=1-\frac{\omega_{\text{P}}^2}{\omega^2+i\Gamma\omega}$. The plasma frequency and the scattering rate for bulk aluminum are considered as $\omega_{\text{P-bulk}}$ = 1.93×10^{16} rad/s and Γ_{bulk} = 1.96×10^{14} rad/s, respectively[103]. The constant values in Drude model enable it to match well with Palik data[102] in the frequency range from 6×10^{14} rad/s down to 9.4×10^{13} rad/s. Note that the optical properties of lightly doped silicon are obtained from the Palik data[102] in the frequency range from 6×10^{14} rad/s down to 5.6×10^{12} rad/s. Besides, the refraction index (n) and extinction coefficient (k) in shorter frequencies are considered constant at the same values as the ones for frequency of 5.6×10^{12} rad/s.

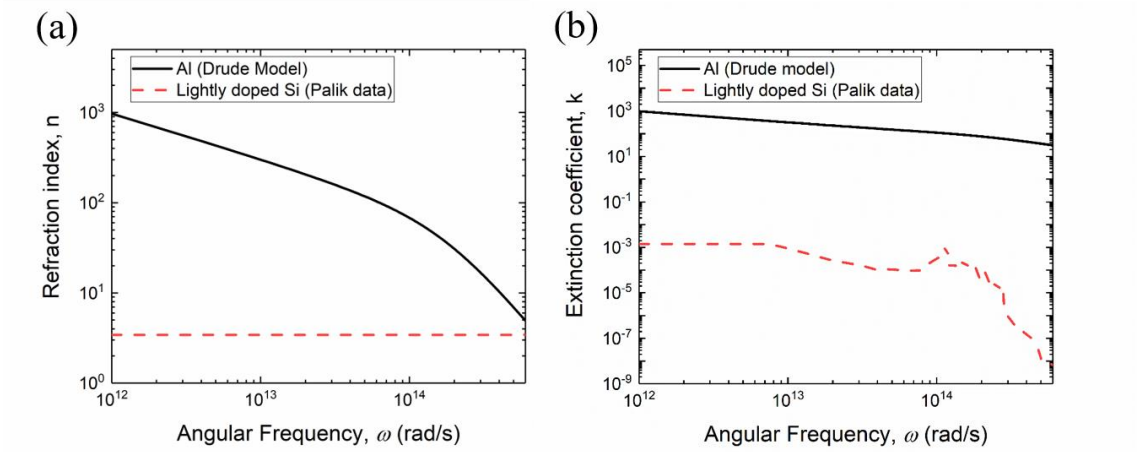

Figure 3.4 Optical constants of aluminum and lightly doped silicon: (a) refraction index n; (b) extinction coefficient k.

The obtained experimental results are later compared with theoretical near-field and far-field results. Hence, it is necessary to discuss the theoretical parts, first. The spectral near-field radiative heat transfer between two radiating media with temperatures of T_{e} and T_{r} can be expressed as[104,105]

$$q_{\mathrm{NFR}} = \frac{1}{\pi^2}\int_0^\infty d\omega\left[\Theta\left(\omega,T_{\mathrm{e}},T_{\mathrm{r}}\right)\right]\int_0^\infty s\left(\omega,\beta\right)d\beta = \frac{1}{4\pi^2}\int_0^\infty d\omega\left[\Theta\left(\omega,T_{\mathrm{e}},T_{\mathrm{r}}\right)\right]\int_0^\infty \beta\xi\left(\omega,\beta\right)d\beta \quad (3.1)$$

where $\Theta\left(\omega,T_{\mathrm{e}},T_{\mathrm{r}}\right) = \hbar\omega/\left(e^{\hbar\omega/k_B T_{\mathrm{e}}}-1\right) - \hbar\omega/\left(e^{\hbar\omega/k_B T_{\mathrm{r}}}-1\right)$ is the difference between the mean energy of Planck's oscillator at different temperatures, k_{B} is the Boltzmann constant, and β is the parallel-component wavevector. $\xi(\omega,\beta)$ represents the energy transmission coefficient depending on the frequency ω, and parallel-component wavevector β and the coefficient s can be defined as $s = \xi\beta/4$. Finally, the expression for $\xi(\omega,\beta)$ for propagating and evanescent waves is given by

$$\xi(\omega,\beta) = \begin{cases} \dfrac{\left(1-\left|R_1^s\right|^2\right)\left(1-\left|R_3^s\right|^2\right)}{\left|1-R_1^s R_3^s e^{i2\gamma_2 d}\right|^2} + \dfrac{\left(1-\left|R_1^p\right|^2\right)\left(1-\left|R_3^p\right|^2\right)}{\left|1-R_1^p R_3^p e^{i2\gamma_2 d}\right|^2}, & \beta < k_0 \\ \dfrac{4\,\mathrm{Im}(R_1^s)\,\mathrm{Im}\left(R_3^s\right)e^{-2\mathrm{Im}(\gamma_2)d}}{\left|1-R_1^s R_3^s e^{i2\gamma_2 d}\right|^2} + \dfrac{4\,\mathrm{Im}(R_1^p)\,\mathrm{Im}\left(R_3^p\right)e^{-2\mathrm{Im}(\gamma_2)d}}{\left|1-R_1^p R_3^p e^{i2\gamma_2 d}\right|^2}, & \beta > k_0 \end{cases} \quad (3.2)$$

Here, the subscripts 1, 2 and 3 denote the emitter, the vacuum layer and the receiver, respectively. Transverse electric and transverse magnetic polarizations are indicated as *s* and *p*, while γ is the wavevector component vertical to the interface. Vacuum gap distance is also shown as *d*. In addition, the thin-film reflection coefficient from vacuum gap to either the emitter (i,e., R_1) or to the receiver (i,e., R_3) is given by

$$R_i = \frac{r_{i-1,i} + r_{i,i+1}e^{i2\gamma_i t}}{1 + r_{i-1,i}r_{i,i+1}e^{i2\gamma_i t}} \quad (3.3)$$

Here, $r_{i,j}$ is the Fresnel reflection coefficient at the single interface from medium *i* to medium *j* and *t* is the thickness of Al thin-film. It should be noted that when the Al thin-film emitter (receiver) become semi-infinite, the thin-film reflection coefficient R_1 (R_3) will be replaced by the Fresnel reflection coefficient r_1 (r_3).

In addition, the net far-field (FF) radiative heat flux between two large parallel surfaces can be calculated by

$$q_{\mathrm{FF}} = \frac{\sigma_{\mathrm{SB}}(T_{\mathrm{e}}^4 - T_{\mathrm{r}}^4)}{\frac{1}{\varepsilon_{\mathrm{e}}} + \frac{1}{\varepsilon_{\mathrm{r}}} - 1} \tag{3. 4}$$

where σ_{SB} is Stefan-Boltzmann constant and ε denotes the emissivity of each layer. Here, the total-hemispherical emissivity of aluminum is considered as $\varepsilon_{\mathrm{Al}} = 0.03$ at 300 K.

Note that the total blackbody radiation is calculated by the well-known Planck's law as:

$$q_{\mathrm{BB}} = \sigma_{\mathrm{SB}}(T_{\mathrm{e}}^4 - T_{\mathrm{r}}^4) \tag{3. 5}$$

3.3 Plate-Plate Near-Field Radiation Measurement Setup

Fig. 3.5(a) illustrates the experimental platform fabricated to measure the near-field radiative heat flux (see Fig. 3.6 for the photos of the actual setup), where an Al thin-film emitter with the same thickness as the receiver is separated from the receiver sample by the polystyrene particles, under the total applied force of 30 mN which creates a vacuum gap around 200 nm. A thermoelectric heater is used to vary the emitter sample temperature, while a thermoelectric cooler maintains the receiver sample at a constant temperature of 23°C to create temperature differences, ΔT, from 25 K to 65 K by adjusting power inputs independently with different DC power supplies. Copper plates with 3.25 mm thickness and the conduction thermal resistance, $R_{\mathrm{copper}} = 0.325$ K/W, are used to spread the heat uniformly underneath (above) the receiver (emitter) samples. The temperatures of the emitter (T_1) and receiver (T_2) are measured by thermistors embedded inside the center of the Cu plates with an accuracy of ±0.1°C. Thermal grease (Arctic

Silver Ceramique 2) is used at every interface to minimize contact resistance R_{grease}, which varies from 0.129 K/W to 0.328 K/W between measurements. A 1.1-mm-thick glass microscope slide with a thermal conductivity of 1 W/mK and conduction thermal resistance, R_{glass} = 44 K/W, is placed below the receiver sample to find the amount of heat transfer by measuring the copper plate temperatures T_2 and T_3 across the slide.

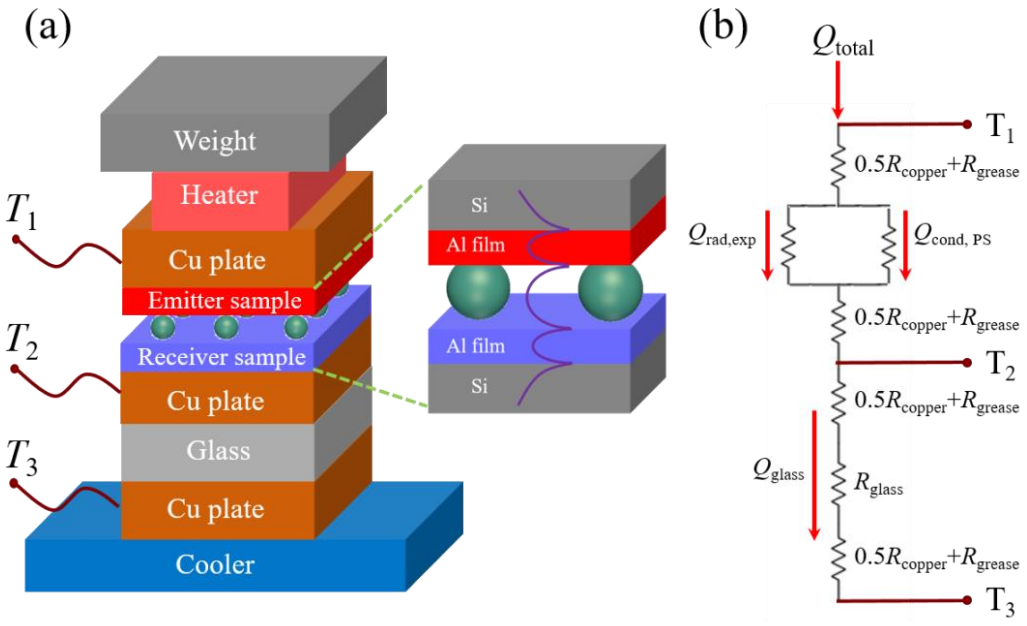

Figure 3.5 (a) Schematic of the experimental setup with the illustration of coupled SPP inside the vacuum gap and within the thin-film of Al. Thermistors were inserted inside the Cu plates. (b) Equivalent thermal circuit model. The emitting layer is maintained at temperature of T_1 and the receiver is at T_2 separated by a vacuum gap distance d.

Note that the copper plates, samples, and glass slide have the same area of A = 5×5 mm^2. According to the 1D thermal resistance network in Fig. 3.5(b), the rate of heat transfer Q_{glass} across the glass slide can be calculated as

$$Q_{glass} = \frac{T_2 - T_3}{2R_{grease} + R_{copper} + R_{glass}} \tag{3.6}$$

Under steady-state conditions and by neglecting side losses, the energy balance yields $Q_{total} = Q_{glass} = Q_{rad,exp} + Q_{cond,PS}$, where $Q_{cond,PS}$ is the heat conduction via the polystyrene (PS) particles calculated by Fourier's Law and the Hertz model (see Fig 3.7). Therefore, the rate of near-field radiative heat transfer $Q_{rad,exp}$ from the experiment can be determined by

$$Q_{rad,exp} = Q_{total} - Q_{cond,PS} \tag{3.7}$$

With the given nanoparticle concentration, $Q_{cond,PS}$ is less than 8% of the theoretical near-field radiative heat transfer between lightly doped Si at a vacuum gap distance of 200 nm . The experimental setup was placed inside a 12-inch diameter vacuum chamber where the measurement was conducted in a high vacuum environment, provided by a turbo pump which maintained a pressure less than 0.1 Pa. At this pressure, the conduction heat transfer with air molecules is less than 0.2% of the near-field radiative heat transfer between lightly doped Si at 200-nm vacuum gap from calculation (Fig. 3.8). The temperature difference between the emitter and receiver samples was varied from 25 K to 65 K with the TE heater and cooler, while the T_1, T_2, and T_3 readings were recorded for each measurement at steady state. The measurement is considered to be at steady-state when the variation of all temperatures was less than 0.1°C over 5 minutes. Three independent measurements were conducted for each Al thin-film of the same thickness, with a new pair of samples being used for each subsequent measurement. To ensure the consistency of the experimental procedures, the same suspension of PS nanoparticles was distributed over the Al thin-film samples with the same thickness that were fabricated from the same batch during the same particle distribution process along with one pair of bare Si chips.

Fig. 3.6 shows the actual experimental setup employed to measure the near-field radiative heat flux. The vacuum gap distance between two planar 5×5 mm^2 samples of the Al thin-films is maintained by 200 nm-polystyrene particles. The power input was supplied by a thermoelectric heater and the receiver temperature was kept constant at 23°C by a thermoelectric cooler. All temperatures were measured by thermistors placed inside the center of the Cu plates with an accuracy ±0.1°C.

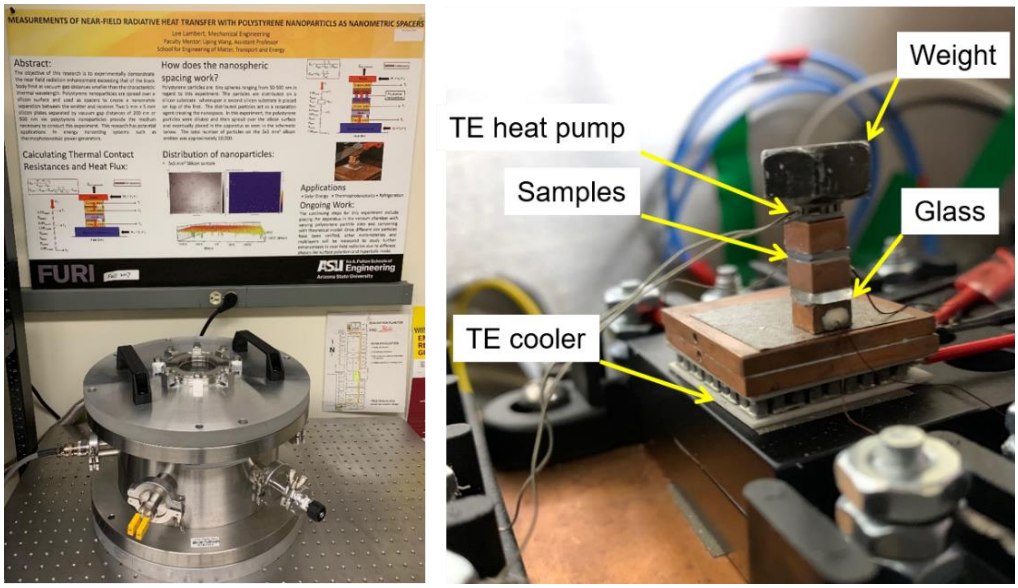

Figure 3.6 The photographs for the setup of the near-field radiative measurement with the plate-plate configuration and the vacuum chamber.

3.4 Evaluation of Conduction Heat Transfer

In this section, the conduction heat transfer through PS particles in addition to air conduction heat transfer are discussed in details. First, the conduction heat rate through the PS nanosized particles is estimated using Fourier's Law as[106]

$$q_{\text{cond,PS}} = \frac{Q_{\text{cond,PS}}}{A} = \frac{N\kappa A_{\text{c}}(T_{\text{e}} - T_{\text{r}})}{DA} \tag{3.8}$$

where N is the total number of particles distributed over the sample surface, κ and D are the thermal conductivity and diameter of PS nanoparticles, respectively, and A = 5×5 mm^2 represents the surface area of the samples. In addition, the contact area A_c between the PS nanoparticle and the lightly doped Si sample can be determined by using the Hertz model. This model calculates the resultant radius of circular contact area between two elastic spheres under applied vertical force as[106]

$$a = \{\frac{3FR_r}{4E^*}\}^{1/3} \tag{3.9}$$

where F is the applied vertical force. It should be noted that E^* (contact modulus) and R_r (reduced radius) can be defined as[106]

$$\frac{1}{E^*} = \frac{1-\nu_{Si}^2}{E_{Si}} + \frac{1-\nu_{PS}^2}{E_{PS}} \tag{3.10}$$

$$\frac{1}{R_r} = \frac{1}{R_{Si}} + \frac{1}{R_{PS}} \tag{3.11}$$

Here, R, ν, and E are radius, Poissons's ratio, and Young's modulus of the mediums. Note that Poissons's ratio and Young's modulus of PS nanoparticles are considered as 0.33 and 4.2 GPa[107] while those for Si sample are 0.22 and 165 GPa[108], respectively. Finally, the contact area between the 200 nm PS particle and silicon sample was estimated to be A_c = 657 nm^2 under the total applied force of F = 30 mN. As a comparison, the conduction heat flux rate and the near-field radiative heat flux between lightly doped silicon samples at 200 nm gap distance are compared in Fig. 3.7. It can be observed that total heat conduction through nanoparticles is less than 8% compared to the near-field heat flux at vacuum gap distance of 200 nm between lightly doped Si.

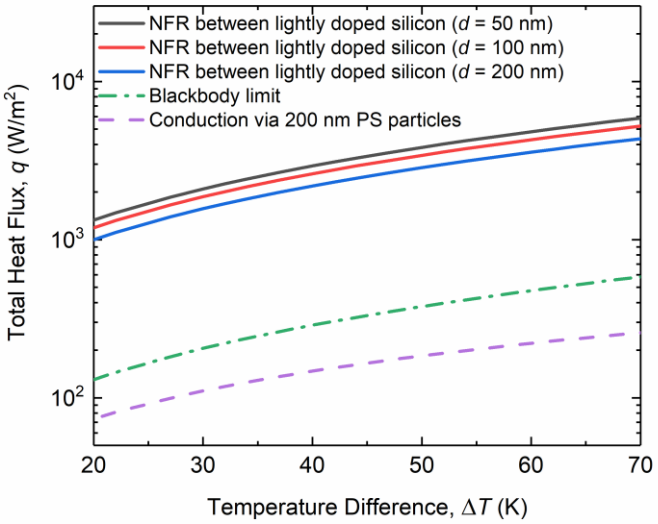

Figure 3.7 Comparison between the total near-field radiative heat flux and conduction heat flux through approximately 1.56×10^5 polystyrene nanoparticles (PS-NP) on 5×5 mm^2 lightly doped silicon surfaces at a 200 nm gap distance as a function of temperature difference between the emitter and receiver layers. Note that the receiver temperature is kept constant at 23°C.

In the energy balance equation (Eq. 3.7), the effect of air conduction is not included. Hence, it is necessary to make sure that the air conduction is negligible compared to the total near-field radiative heat transfer. The air conduction can be calculated as[12]

$$q_{\text{cond,air}} = \frac{k\left(T_{\text{e}} - T_{\text{r}}\right)}{d\left(1 + Kn\dfrac{(2-\alpha_T)(9\gamma-5)}{\alpha_T(\gamma+1)}\sqrt{\dfrac{T_{\text{m,FM}}}{T_{\text{m,DF}}}}\right)} \tag{3.12}$$

where k is the thermal conductivity of air at diffusion regime, Kn is the Knudsen number, d is the gap distance, α_T is the thermal accommodation coefficient, γ is the specific heat ratio and T_{e} and T_{r} are the temperature of emitter and receiver, respectively. In addition,

$T_{m,FM}$ and $T_{m,DF}$ also represent the effective mean temperatures for the free molecule and the diffusion regimes, respectively.

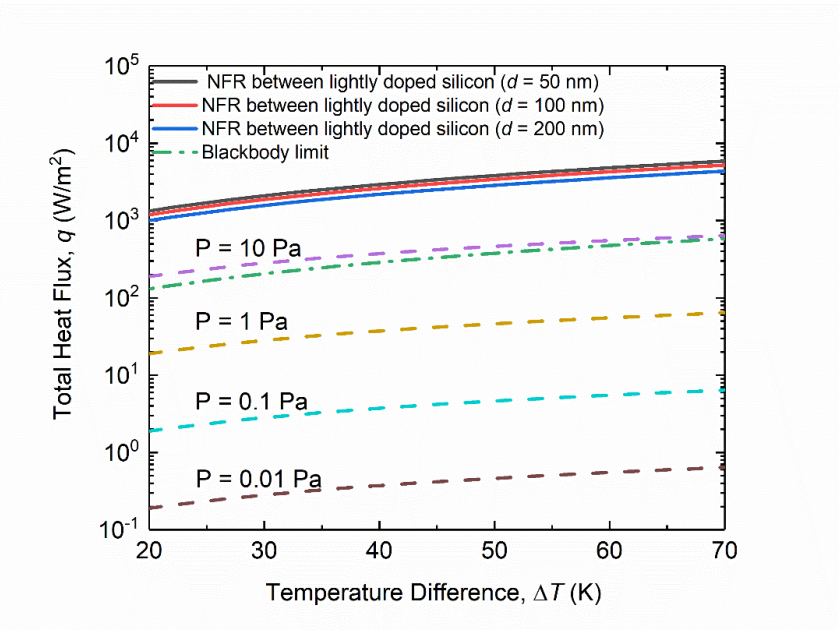

Figure 3.8 Near-field radiative heat flux between lightly doped silicon plates at 50, 100, and 200 nm vacuum gap distances in comparison with blackbody limit and air conduction heat flux at different vacuum pressures from 0.01 Pa to 10 Pa as a function of temperature difference between the emitter and receiver. Note that the receiver temperature is kept constant at 23°C.

As a comparison, the total near-field radiative heat fluxes between lightly doped silicon samples at 50, 100, and 200 nm gap distances and the air conduction at different pressures are plotted as a function of temperature difference between the emitter and receiver in Fig. 3.8. Note that the receiver temperature is kept constant at 23°C and the air pressure is changing from 0.01 Pa to 10 Pa. For instance, the air conduction heat flux at an air pressure of 0.1 Pa is less than 0.2% of that for near-field radiative heat flux between lightly doped silicon samples at a 200 nm gap distance. In the current

measurement, the air conduction is eliminated by maintaining the vacuum chamber pressure below 0.1 Pa.

3.5 Vacuum Gap Determination with Lightly-Doped Si Samples

One major challenge in the plate-plate near-field radiation measurements with mm-sized samples is how to experimentally determine the gap distance accurately. It should be noted that the nominal diameter of the nanoparticles cannot be discounted as a precise vacuum gap distance. The optical interferometry method, which requires double-side polished semitransparent samples, has been used to determine the gap distance by fitting the interference fringe measured between lightly doped Si before near-field measurement[63] and between quartz samples during the near-field measurement[15,59]. However, it cannot be applied to metallic thin-films due to opacity or very small transmission due to strong light attenuation. Here, we conducted additional near-field radiation measurements with 4 pairs of bare Si chips, each coated with the same PS particle suspension at the same time with Al thin-film sample of different thickness. The gap distance was obtained by fitting the measured near-field radiative heat flux between Si plates $q_{\mathrm{rad,exp}} = Q_{\mathrm{rad,exp}}/A$ with theoretical values $q_{\mathrm{rad,theo}}$ calculated by fluctuational electrodynamics as discussed in Eq. 3.1. Each pair of Si chips was coated with the same 200 nm- polystyrene particles at the same time as the PS particles were distributed over the various thicknesses of Al thin-film samples. A least-square method is used to fit the vacuum gap distance of the upper bound, average, and lower bound of the measured $q_{\mathrm{NFR,exp}}$ for Si samples at different ΔT by minimizing the total absolute error Z defined by

$$Z = \sqrt{\sum_{i=1}^{n} (Q_{\text{lower bound/mean/upper bound}} - Q_{\text{calculated at arbitrary } d})^2} \tag{3.13}$$

where n=9 indicates the number of total temperature differences between the emitter and receiver samples in each measurement. Note that the absolute error Z for the upper bound (270 nm), mean (215 nm), and lower bound (165 nm) of the total measured radiative heat flux between the lightly doped silicon samples are calculated as 112 W/m^2, 190 W/m^2 and 280 W/m^2, respectively.

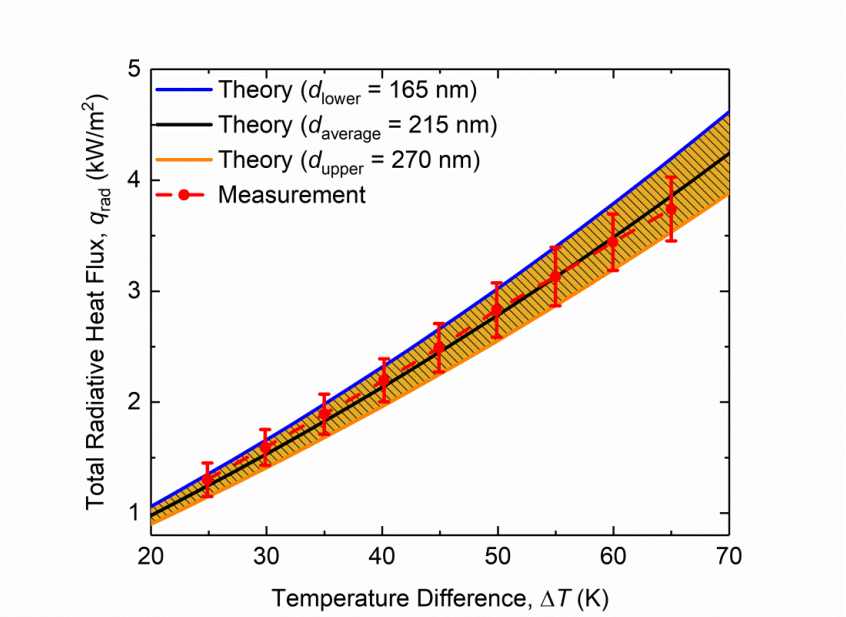

Figure 3.9 The near-field radiative heat flux between the lightly doped silicon samples separated by 200 nm-polystyrene particles. The temperature of the receiver is kept constant at 23°C. The fitted gap distance for mean value, upper bound, and lower bound are plotted as solid black, blue, and orange lines, respectively.

The near-field radiative heat transfer rate between the lightly doped Si samples is plotted as a function of temperature difference between the emitter and receiver, ΔT. The red circles show the experimental results, while the solid lines are fitted gap distances for

upper bound, mean, and lower bound of measured radiative heat flux rates at vacuum gap distances of 165, 215 and 270 nm, respectively. Error bars also show the standard uncertainty U_c associated with the measured radiative heat fluxes. To evaluate the precision of the measured near-field radiative heat flux, the total uncertainty is calculated as a combination of uncertainty type A and type B. The uncertainty type A (u_A), is due to the statistical variation of the observed measurements and is equal to the standard deviation of the measured near-field radiative heat fluxes at specific temperature differences between the emitter and receiver. On the other hand, the uncertainty type B evaluates the error propagation from the accuracy of measurement devices which can be calculated as

$$u_B = \sqrt{\left(\sum_{i=1}^{n}\left(\frac{\partial q_{NFR}}{\partial x_i} s_{x,i}\right)^2\right)} \tag{3.14}$$

Here, u_B is the type B uncertainty of the output (near-field radiative heat flux) while x_i indicates the measured input variables R_{Cu}, R_{grease}, R_{glass} and the temperature difference across the glass slide and $s_{x,i}$ is the corresponding uncertainty of each input measured variable. Finally, the uncertainty of the near-field radiative heat flux is defined as

$$U_c = k_c \sqrt{u_A^2 + u_B^2} \tag{3.15}$$

where the coverage factor k_c is considered as one to provide a confidence level of approximately 68%.

3.6 Near-Field Radiation Heat Flux of Al with Different Film Thicknesses

The comparison between the measured near-field radiative heat flux and the theoretical calculations at the fitted vacuum gap of d = 215 nm is shown in Figs. 3.10(a-

d) for Al thin-films with different thicknesses determined by AFM: (a) 13±2 nm, (b) 24±3 nm, (c) 40±3 nm, and (d) 79±3 nm. Note that the temperature of the receiver is kept constant at 23°C and temperature difference ΔT between the emitter and receiver is varied from 25 K to 65 K. The shaded area displays the calculated near-field radiative flux considering the uncertainty of the vacuum gap distance $d = 215^{+55}_{-50}$ nm obtained from four near-field radiation measurements between bare Si chips (as already discussed in Section 3.5), whereas solid black lines denote the near-field radiative heat fluxes at the average vacuum gap distance of d = 215 nm. The measured near-field radiative heat fluxes $q_{\mathrm{NFR,exp}}$, symbolized by the red markers with error bars as combined uncertainties U_c , show good agreement with theoretical predictions. It can be observed that the near-field radiative heat flux increases as the thickness of aluminum thin-film decreases. In the insets of Figs. 3.10(a-d), the total radiative heat flux of the Al thin-films at a vacuum gap distance of 215 nm is compared with the blackbody limit and far-field radiation of bulk aluminum surfaces. The theoretical results indicate that the total radiative heat flux between the 13-nm Al thin-film samples separated by a vacuum gap of 215 nm is approximately 5224 W/m^2 for the temperature difference ΔT = 65 K, indicating a theoretical improvement about 10 times over the blackbody limit and 650 times compared to the far-field radiation of bulk aluminum sample. The near-field radiative heat flux for thicker Al samples was calculated to be 3943 W/m^2, 2846 W/m^2 and 1901 W/m^2 for 24, 40 and 79-nm-thick Al films, respectively, under the same temperature difference of 65 K. As shown in Fig. 3.10, the near-field radiative heat flux decreases monotonically with increasing aluminum thickness.

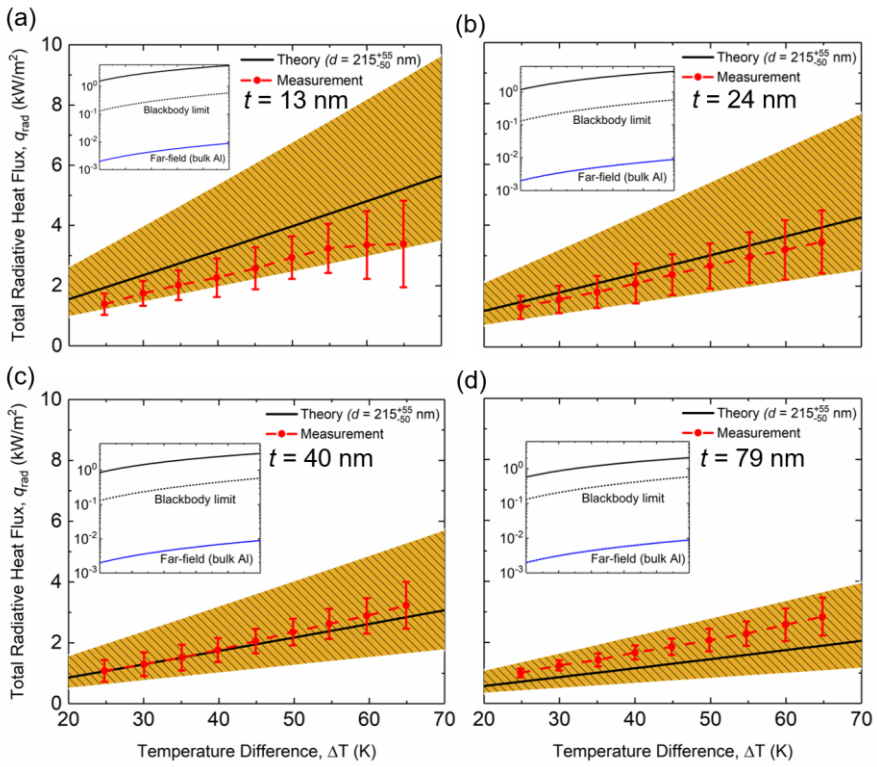

Figure 3.10 Measured near-field radiative heat flux (markers with error bars) between Al thin-films of several thicknesses at different ΔT values along with the theoretical prediction (shaded) at a vacuum gap distance $d = 215^{+55}_{-50}$ nm fitted from the near-field measurement with bare Si chips. The thicknesses of the aluminum are: (a) 13±2 nm, (b) 24±3 nm, (c) 40±3 nm, and (d) 79±3 nm. Note that the temperature of the receiver is kept constant at 23°C. The inset shows the total radiative heat flux at a vacuum gap of 215 nm compared with the blackbody limit and far-field radiative heat transfer of bulk aluminum plates.

Near-field radiative heat flux enhancement factors over the blackbody limit and over far-field radiation of bulk aluminum plates as a function of aluminum thickness are plotted in Figs. 3.11(a) and (b), respectively. The receiver temperature is kept constant at 23°C and the temperature difference between emitter and receiver is 65 K. At a vacuum gap distance of 215 nm, the near-field radiation heat flux was experimentally measured

with an average enhancement of 6.4 times over blackbody limit and ~420 times over far-field radiation with bulk Al, which is roughly consistent for all four Al thin-films of different thicknesses of 13 nm, 24 nm, 40 nm and 79 nm. On the other hand, calculations predict that the largest near-field radiative enhancement at d = 215 nm occurs with the 5-nm-thick Al thin-film attaining 11 times over the blackbody limit and 720 times over far-field radiation of bulk aluminum plates, respectively.

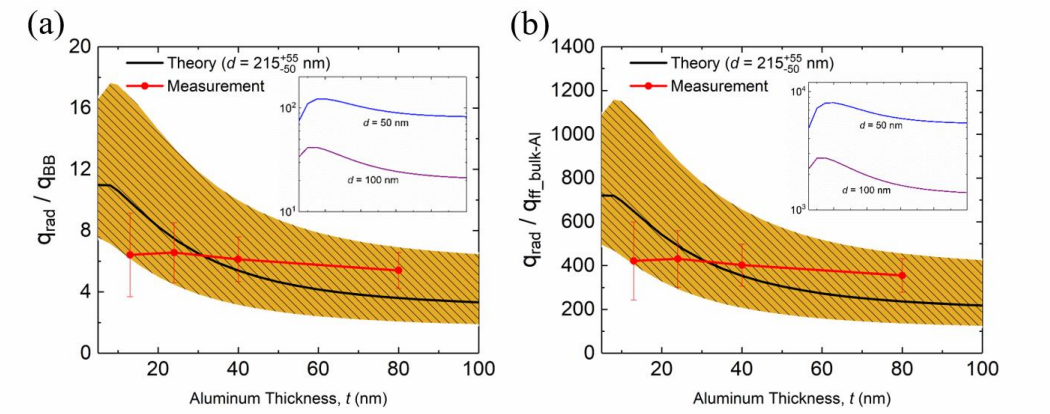

Figure 3.11 Measured near-field heat flux enhancement (markers with error bars) between Al thin-films at different thicknesses compared to (a) blackbody limit and (b) far-field radiative heat transfer between bulk aluminum plates. The shaded region indicates the vacuum gap uncertainty $d = 215^{+55}_{-50}$ nm while the average vacuum gap of 215 nm is shown by the solid black line. The insets inside (a) and (b) show the total radiative heat flux enhancement over blackbody and far-field limits at vacuum gap distances of 50 nm and 100 nm, respectively. Note that the temperature of the receiver is kept constant at 23°C and the temperature difference is 65 K.

Due to the uncertainty with the near-field heat flux measurement as well as with the theoretical prediction from the fitted vacuum gap $d = 215^{+55}_{-50}$ nm, the experimental data and calculation are considered to be within reasonable agreement as shown in Figs. 3.11. In addition, the insets of Figs. 3.11(a) and (b) display the near-field enhancement

factor over the blackbody limit and over far-field radiation of bulk aluminum calculated at smaller vacuum gap distances of 50 nm and 100 nm, respectively. The results suggest that the near-field enhancement over the blackbody limit could potentially reach 42 times with 15-nm-thick Al at a vacuum gap of 100 nm, or even 123 times with 20-nm-thick Al at a vacuum gap of 50 nm. When compared to the far-field radiation with bulk Al, the near-field and thin-film effects could enhance the radiation heat flux up to 2750 times with 15-nm-thick Al at d = 100 nm or 8060 times with 20-nm-thick Al at d = 50 nm.

3.7 Physical Mechanisms

To gain insight into the underlying mechanisms that enhance the radiative heat transfer between 10-nm Al thin-films in the near-field, the energy transmission coefficients for *s* and *p* polarizations at vacuum gap distance of 200 nm are presented in Figs. 3.12(a) and (b), respectively. The large transmission coefficients, shown by the bright contour, verify that the near-field radiative enhancement is attributed to the SPP coupling inside the Al thin-film layers for *p*-polarized waves. It can be noticed that the enhancement bands in the energy transmission coefficient for *s*-polarized waves are also significantly extended to high values of transverse wavevector β as shown in Fig. 3.12(b). This enhancement can be explained as the reduced reflectivity at the interface of Al thin-films and hence, contributing to the near-field photon tunneling. Additionally, the energy transmission coefficients between bulk aluminum surfaces at a 200 nm gap distance are plotted for *s* and *p* polarizations in Figs. 3.12(c) and (d), respectively. Compared to the 10-nm Al thin-film, the excitation of SPP in bulk Al is much weaker at *p* polarized

waves, and the contribution of the large transverse wavevector β at *s* polarization is also substantially suppressed.

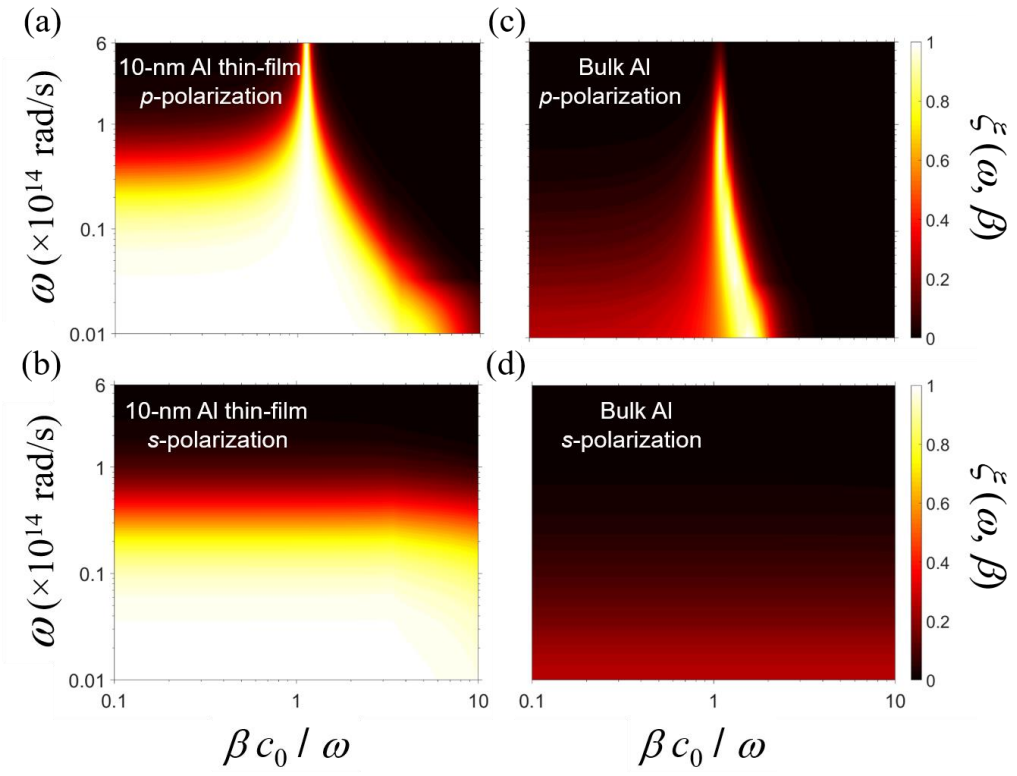

Figure 3.12 Contour plot of energy transmission coefficient (ξ) between lightly doped silicon samples coated by 10 nm aluminum for (a) *p* polarization and (b) *s* polarization, and between bulk aluminum samples for (c) *p* polarization and (d) *s* polarization at a vacuum gap distance of 200 nm. Note that the parallel wavevector component is normalized to the frequency.

The contour plot of $s(\omega,\beta)$ for the 10-nm Al thin-films and bulk Al samples at a vacuum gap distance of 200 nm are presented respectively in Figs. 3.13(a) and (b) as a function of angular frequency (ω) and parallel wavevector component normalized to the frequency. To fully understand the enhancement bands in the contour plots of $s(\omega,\beta)$ between the thin-film of Al samples, the dispersion for SPPs coupling is calculated via

$$\left|1-R_1^p R_3^p e^{i2\gamma_2 d}\right|=0 \tag{3.16}$$

where the expression for the reflection coefficient from the vacuum gap to either the emitter (i,e., R_1) or to the receiver (i,e., R_3) is previously discussed in Eq.3.3.

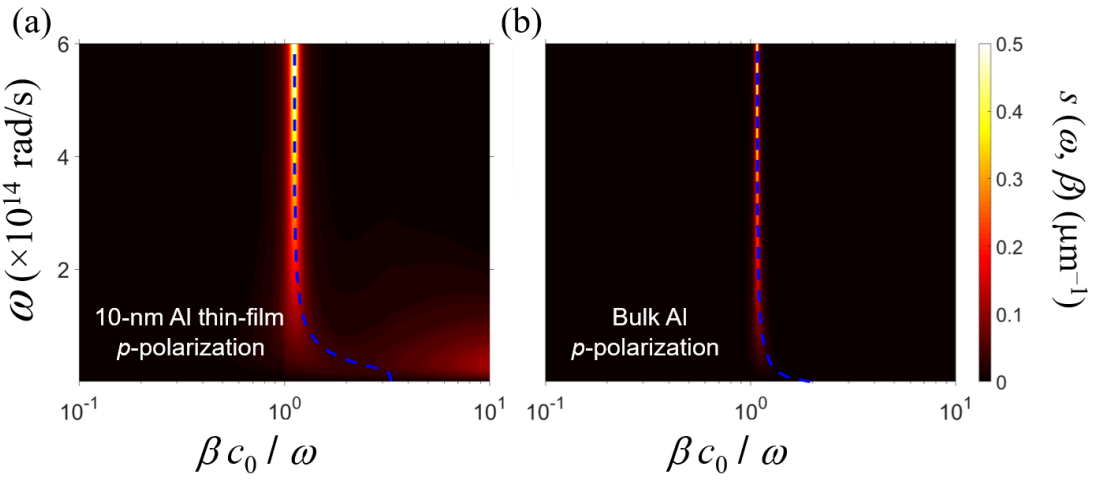

Figure 3.13 Contour plot of $s(\omega,\beta)$ for (a) 10-nm Al thin-film and (b) bulk Al at a vacuum gap distance of 200 nm. Note that the parallel wavevector component is normalized to the frequency. Surface-polariton dispersion is shown by the blue dashed line.

The dispersion curves, represented as the blue dashed lines in Figs. 3.13 (a-b), indicate that the enhancement bands in the contour plots of $s(\omega,\beta)$ are due to the excitation of surface plasmon polariton between the emitter and receiver samples. In addition, SPP coupling inside the Al thin-film layers cause further near-field heat flux enhancement in comparison to single SPP excitation inside the bulk Al samples as illustrated in Fig. 3.13.

To further illustrate the radiative heat transfer enhancement between ultra-thin aluminum films over bulk Al plates, the spectral radiative heat fluxes of *s* and *p* polarizations are compared, in addition to the effect of vacuum gap distance on the total

near-field radiative heat flux enhancement. To clarify the mechanism behind the heat flux enhancement for the 10-nm aluminum thin-film coated on silicon, the spectral radiative heat fluxes of *s* and *p* polarizations are shown in Fig. 3.14. As a comparison, the spectral heat fluxes between bare silicon samples and bulk metals are also shown in Fig. 3.14. The receiver temperature is 23°C and the temperature difference between emitter and receiver is 65 K. It illustrates that the spectral heat flux enhancement between the Al thin-films and bulk metals at lower frequency ranges are mainly due to the contribution of *s*-polarized waves, whereas the 10-nm-thick Al yields higher spectral heat flux because of reduced reflectivity at the interface of the thin-film layer over the bulk.

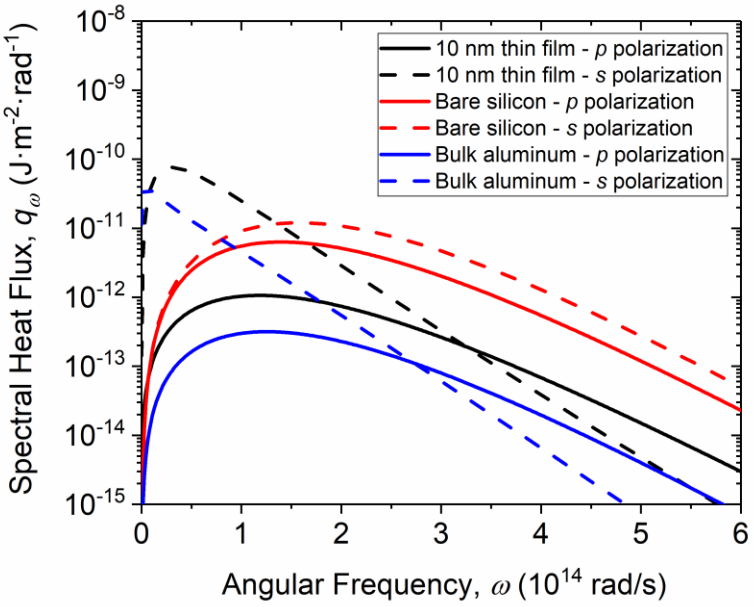

Figure 3.14 The spectral radiative heat flux for lightly doped silicon, bulk aluminum, and lightly doped silicon samples coated by 10-nm aluminum separated by a vacuum gap distance of 200 nm. The temperature of the receiver is 23°C and the temperature difference between the emitter and receiver is 65 K.

The total radiative heat flux enhancement between the aluminum thin-films, bulk bare silicon samples, and bulk aluminum plates are compared to blackbody limit as a function of vacuum gap distance in Fig. 3.15. The receiver temperature is constant at 23°C and the temperature difference between the emitter and receiver samples is 65 K. For all cases, total radiative heat flux increases as the vacuum gap distance decreases due to the contribution of the evanescent mode. For instance, the theoretical results demonstrate that the radiative heat flux between 10 nm aluminum thin-films exceeds the blackbody limit by 110.4 and 12.2 times at vacuum gaps of 50 nm and 200 nm, respectively.

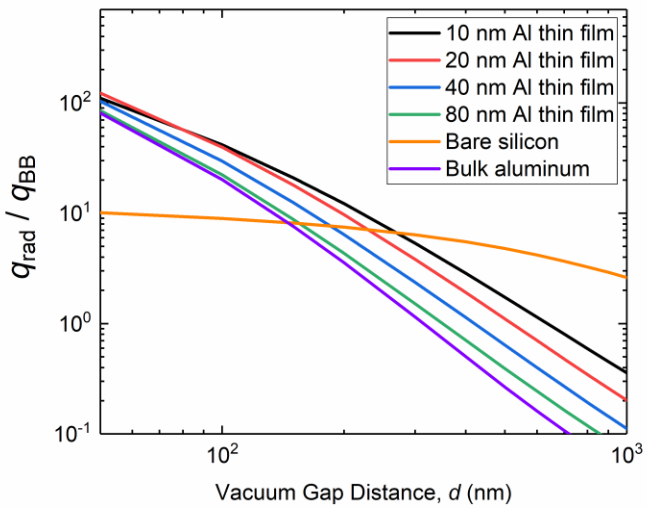

Figure 3.15 The near-field radiative heat transfer enhancement between aluminum thin-films, bulk bare silicon samples, and bulk aluminum plates compared to the blackbody limit at different vacuum gap distances. The temperature of receiver is 23°C and the temperature difference between the emitter and receiver is 65 K.

Lastly, the effect of native oxidation of Al on the total near-field radiative heat flux is presented in this section. Fig. 3.16 illustrates the theoretical near-field radiative

heat flux between 13 nm Al thin-film compared with 3-nm-thick Al_2O_3 layers grown on 10 nm Al thin-film both deposited on Si chips as a function of temperature difference ΔT between the emitter and receiver. The temperature of the receiver is also considered constant at 23^0C and the vacuum gap distance is 215 nm. The theoretical results obtained from fluctuational electrodynamics indicate that 3-nm thick aluminum oxide layer affected the total near-field radiative heat flux by less than 4%. For instance, at a temperature difference of ΔT = 70 K, the total radiative heat flux with and without the Al oxide layer is calculated as 5.8 kW/m^2 and 5.6 kW/m^2, respectively. Thus, the effect of native oxidation of Al with 3-nm Al_2O_3 on the total near-field radiative heat flux is negligible.

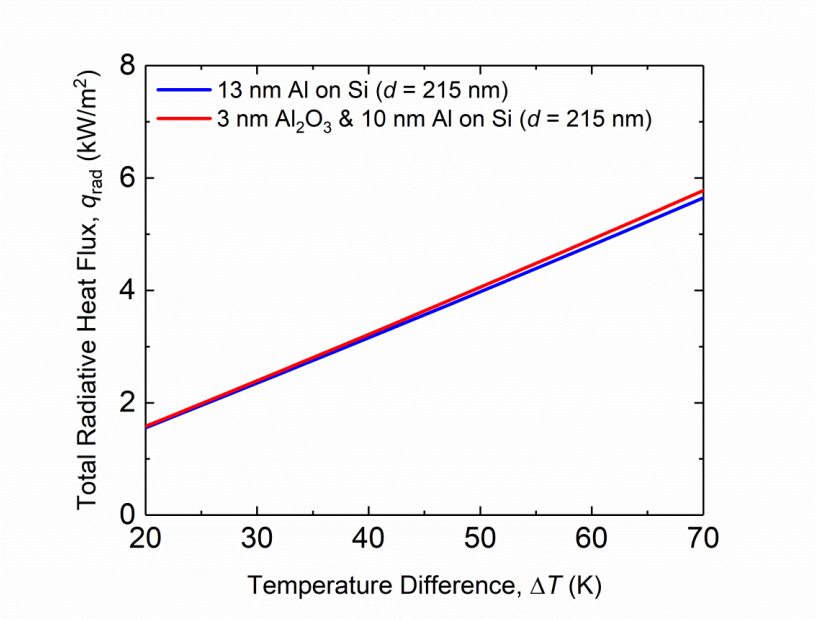

Figure 3.16 The near-field radiative heat flux between 13 nm Al thin-films compared with 3 nm-thick Al_2O_3 layers grown on 10 nm Al thin-films both deposited on lightly doped silicon samples maintained by a vacuum gap distance of 215 nm. Note that the temperature of the receiver is kept constant at 23°C.

CHAPTER 4

THEORETICAL STUDY OF NEAR-FIELD THERMOPHOTOVOLTAIC SYSTEMS WITH MULTILAYER METAMATERIAL EMITER AND TANDEM CELLS

The main purpose of this Chapter is to spectrally tune the absorption of the receiver and enhance the conversion efficiency in a TPV system. Section 4.1 gives the theory of the near-field radiation between isotropic homogenous multilayers. The standard and direct methods for the calculation of charge transport in a PV cell are provided in Section 4.2. Section 4.3 numerically studies the electrical power output of a TPV system consisting of multilayer metamaterials with alternate tungsten and alumina layers, as an efficient selective emitter. Finally, a TPV system with a plain planar emitter separated from a PV tandem cell is numerically analyzed in Section 4.4.

4.1 Theory of Near-Field Radiative Transfer between Isotropic Homogenous Multilayers

In this section, the near-field thermal radiation between isotropic homogeneous multilayers will be theoretically studied by using the fluctuational electrodynamics theory along with the dyadic Green's function. This study paves the way to design and optimize the nanostructured multilayer emitters to tune the spectral heat transfer and improve the efficiency of the near-field TPV systems. The electric field **E** and magnetic field **H** can be expressed as[5,109]

$$\mathbf{E}(\mathbf{x},\omega) = i\omega\mu_0 \int_{\mathrm{V}} \overline{\overline{\mathbf{G}}}_{\mathrm{E}}(\mathbf{x},\mathbf{x}',\omega)\mathbf{j}(\mathbf{x}',\omega)\mathrm{d}\mathbf{x}' \tag{4.1a}$$

$$\mathbf{H}(\mathbf{x},\omega) = \int_{V} \overline{\overline{\mathbf{G}}}_{H}(\mathbf{x},\mathbf{x}',\omega)\mathbf{j}(\mathbf{x}',\omega)d\mathbf{x}' \tag{4.1b}$$

where μ_0 is the magnetic permeability in vacuum, and i is unit of purely imaginary number. The terms $\overline{\overline{\mathbf{G}}}_{E}(\mathbf{x},\mathbf{x}',\omega)$ and $\overline{\overline{\mathbf{G}}}_{H}(\mathbf{x},\mathbf{x}',\omega)$ are the electric and magnetic dyadic Green's functions respectively. The electric and magnetic dyadic Green's functions demonstrate the relationship between the electric field $\mathbf{E}(\mathbf{x},\omega)$ and magnetic field $\mathbf{H}(\mathbf{x},\omega)$, with frequency ω at location **x,** and a vector source at location **x'** within a body of volume V, respectively**.** By considering a cylindrical coordinate system, the space variable can be defined as $\mathbf{x} = r\vec{\mathbf{r}} + z\vec{\mathbf{z}}$, with r-direction being parallel to the interface and z-direction perpendicular to the interface.

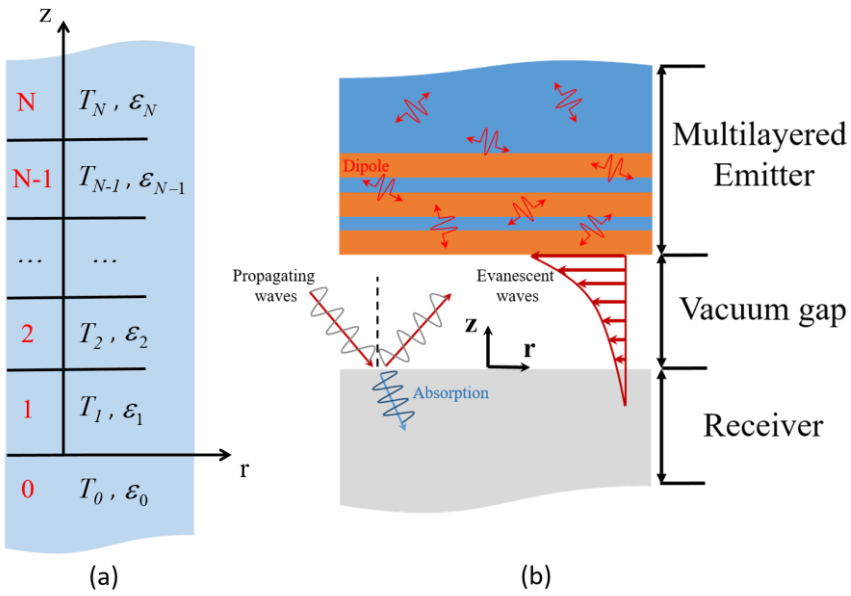

Figure 4.1 (a) Schematic of a one dimensional multilayered structure sandwiched between two semi-infinite mediums. Corresponding temperature and dielectric function of each layer is denoted as T and ε, respectively. (b) Schematic for near-field radiation from both the propagating and evanescent electromagnetic weaves due to thermally induced dipoles. Two parallel plates are separated by a vacuum gap distance d.

The dyadic Green's function between any two layers of the multilayered structure shown in Fig 4.1 is given by[5,41,110]

$$\overline{\overline{\mathbf{G}}}_{\mathrm{E}}(\mathbf{x},\mathbf{x}',\omega)=\frac{i}{4\pi}\int\frac{\beta \mathrm{d}\beta}{k_{\mathrm{z},s}}F(\beta)e^{i\beta(r-r')} \tag{4.2}$$

where

$$F(\beta)=Ae^{i(k_{z,l}z-k_{z,s}z')}\vec{\mathbf{e}}_l^{+}\vec{\mathbf{e}}_s^{+}+Be^{i(-k_{z,l}z-k_{z,s}z')}\vec{\mathbf{e}}_l^{-}\vec{\mathbf{e}}_s^{+}+Ce^{i(k_{z,l}z+k_{z,s}z')}\vec{\mathbf{e}}_l^{+}\vec{\mathbf{e}}_s^{-}+De^{i(-k_{z,l}z+k_{z,s}z')}\vec{\mathbf{e}}_l^{-}\vec{\mathbf{e}}_s^{-} \tag{4.3}$$

Here, $\mathbf{k}_{\mathrm{i}}=\beta\vec{\mathbf{r}}+k_{\mathrm{z,i}}\vec{\mathbf{z}}$ and $k_i=\sqrt{\varepsilon_i}\,\omega/c$. The subscript *s* denotes the emitting layer and *l* represents the receiving layer. Unit vectors $\vec{\mathbf{e}}^{-}$ and $\vec{\mathbf{e}}^{+}$ are also defined for s and p polarizations as $\vec{\mathbf{e}}^{-}=\vec{\mathbf{e}}^{+}=\vec{\mathbf{r}}\times\vec{\mathbf{z}}$ and $\vec{\mathbf{e}}_i^{\pm}=(\beta\vec{\mathbf{z}}\mp k_{z,i}\vec{\mathbf{r}})/k_i$, respectively[5,41,110]. The coefficients A, B, C and D can be obtained by using the transfer matrix formulation[5,110]. Based on the ergodic hypothesis, the spectral heat flux at location **x** is given by the ensemble average of the spectral Poynting vector as[110]

$$\langle\mathbf{S}(\mathbf{x},\omega)\rangle=\int_0^{\infty}\frac{1}{2}\langle\mathrm{Re}[\mathbf{E}(\mathbf{x},\omega)\times\mathbf{H}^{*}(\mathbf{x},\omega)]\rangle\mathrm{d}\omega \tag{4.4}$$

where the superscript * denotes the conjugate of complex number. Thus, the energy absorbed by a layer is calculated as the difference between the total heat fluxes at upper and lower interfaces. To solve equation (4.4), the ensemble average of the fluctuating current densities should be calculated by the fluctuation-dissipation theory as[110,111]

$$\left\langle j_m(\mathbf{x}',\omega)\,j_n^{*}(\mathbf{x}'',\omega')\right\rangle=(4/\pi)\omega\varepsilon_0\,\mathrm{Im}(\varepsilon(\omega))\delta_{mn}\delta(\mathbf{x}'-\mathbf{x}'')\Theta(\omega,T)\delta(\omega-\omega') \tag{4.5}$$

where $\Theta(\omega,T)=\hbar\omega/\left[\exp(\hbar\omega/k_{\mathrm{B}}T)-1\right]$ is the mean energy of a Planck oscillator in thermal equilibrium at frequency ω and temperature *T*, $\hbar$ is the Planck constant divided

by 2π and k_B is the Boltzmann constant. Permittivity of the free space is denoted by ε_0. Subscripts m and n (m, n = 1, 2, or 3) refer to orthogonal components of fluctuating current densities**,** δ_{mn} is the Kronecker delta and $\delta(\omega-\omega')$ is the Dirac delta function. Substitution of Eqs. (4.1(a)), (4.1(b)) and (4.5) into Eq. (4.4) gives the analytical expression of the radiative heat flux at a location z_c along the z-direction of the multilayered structure shown in Figs. 4.1 as[112]

$$q_\omega(z_c)=\frac{k_0^{\,2}\Theta(\omega,T)}{\pi^2}\times \mathrm{Re}[i\varepsilon_s''(\omega)\int_0^\infty \beta \mathrm{d}\beta \int_V \sum_{i=r,\theta,z}(G_{ri}^E G_{\theta i}^{H*}-G_{\theta i}^E G_{ri}^{H*})]\,dz' \qquad (4.6)$$

where k_0 is the wave vector in vacuum and T, V and ε_s'' represent the temperature, volume and imaginary part of the dielectric function of the emitting layer, respectively. The total radiative heat flux represents the contribution from both the propagating and evanescent electromagnetic waves due to thermally induced dipoles as shown in Fig. 4.1(b). The amplitude of the evanescent field decays exponentially with increasing distance from the emitter interface and it would be dominant when the vacuum gap distance becomes smaller than the characteristic wavelength of thermal radiation.

4.2 Model of Charge Transport in the PV Cells

4.2.1 Standard method

In this section, the photocurrent generation would be calculated in a PV cell separated into N layers by solving the charge transport equations. The electron-hole pairs generation rate is described as[85]

$$g_l(\lambda)=\frac{Q_{\lambda,l}}{d_l\left(hc_0/\lambda\right)} \text{ with } \frac{hc_0}{\lambda}\geq E_g \qquad (4.7)$$

where $Q_{\lambda,l}$, is the spectral heat flux absorbed in lth layer of the PV cell with the thickness of d_l, h is the Planck constant, c_0 is the light velocity in vacuum and hc_0/λ is the photon energy at wavelength λ. This equation indicates that only the photons with energy higher than the energy bandgap (E_g) of PV cell can generate electron-hole pairs. In depletion region of the PV cell, the generated electron-hole pairs can be completely collected due to the built-in voltage, and the drift current is expressed as

$$J_{dp}(\lambda) = eg_{dp}(\lambda)L_{dp} \tag{4.8}$$

where $e = 1.602\times10^{-19}$ C is the electron charge, and L_{dp} is the depletion region thickness. On the other hand, minority carrier concentration at p- and n-regions should be calculated to obtain the photocurrent. The electron concentration in p-region can be expressed with the following 1-D, steady state continuity equation[85]:

$$D_e \frac{d^2 n_e}{dz^2} - \frac{n_e - n_e^0}{\tau_e} + g(z,\lambda) = 0 \tag{4.9}$$

The boundary conditions can be set as

$$D_e \frac{dn_e}{dz}\Big|_{z=0} = u_p \left[n_e(0) - n_e^0 \right], \text{ and } n_e|_{z=a} = n_e^0 \tag{4.10}$$

where D_e is the electron diffusion constant, n_e is the local electron concentration, n_e^0 is the equilibrium electron concentration, τ_e is the electron relaxation time, and u_p is the surface recombination velocity in the p-region. The photocurrent generated in the p-region can be then given as

$$J_e(\lambda) = eD_e \frac{dn_e}{dz}|_{z=a} \tag{4.11}$$

Note that the photocurrent in the n-region, $J_h(\lambda)$, can be obtained in the same way by just replacing the electron in the p-region with hole in the n-region. Finally, the total

generated drift current, $J_\lambda(\lambda)$, is the summation of the three drift currents $J_\lambda(\lambda) = J_{dp}(\lambda)+ J_e(\lambda)+ J_h(\lambda)$. The quantum efficiency $\eta_q(\lambda)$, which is the ratio of the number of generated electron-hole pairs and the number of absorbed photons, can be obtained through the total generated drift current and absorbed spectral heat flux[85].

$$\eta_q(\lambda) = \frac{J_\lambda / e}{S_\lambda / (hc/\lambda)} \tag{4.12}$$

where S_λ is the spectral heat flux absorbed by the whole PV cell. The electrical power output can be expressed as[85]

$$P_E = J_{ph} V_{oc} (1 - 1/y)[1 - \ln(y)/y] \tag{4.13}$$

where $y = \ln(J_{ph}/J_0)$. Here, J_{ph} and J_0 are photocurrent and dark current respectively. The dark current (J_0) can be calculated by[113]

$$J_0 = e\left(\frac{n_i^2}{N_D}\sqrt{\frac{D_h}{\tau_h}} + \frac{n_i^2}{N_A}\sqrt{\frac{D_e}{\tau_e}}\right) \tag{4.14}$$

where n_i is the intrinsic carrier concentration, N_A is the acceptor concentration and N_D is the donor concentration. Note that D_h and D_e are diffusion coefficients of p and n region of the PV cell, respectively. The total photocurrent can be also expressed as[85]

$$J_{ph} = \frac{e}{hc}\int_0^{\lambda_g} \eta_q S_\lambda \lambda d\lambda \tag{4.15}$$

where λ_g is the bandgap wavelength of receiver. The open-circuit voltage is expressed by[85]

$$V_{oc} = \left(\frac{k_B T}{e}\right)\ln\left(\frac{J_{ph}}{J_0} + 1\right) \tag{4.16}$$

Finally, the conversion efficiency η, which characterizes the performance of TPV systems, is expressed as the ratio of electrical power output and the radiative power input as:

$$\eta = P_{\mathrm{E}} / P_{\mathrm{R}} \tag{4.17}$$

where $P_{\mathrm{R}} = \int_0^{\lambda} S_{\lambda} d\lambda$ is the total absorbed radiative power by the cell and electrical contacts. In Section 4.3, the performance of a TPV system comprised of a multilayered emitter and a PV cell ($In_{0.18}Ga_{0.82}Sb$) is analyzed by the standard method. The parameters of $In_{0.18}Ga_{0.82}Sb$ cell would be the same as those used in Ref.[85]. The thicknesses of p-region, depletion region, and n-region are set as 0.4 μm, 0.1 μm, and 10 μm, respectively. The p-region has a doping concentration of 10^{19} cm^{-3}, and that for n-region is 10^{17} cm^{-3}. The diffusion coefficient and relaxation time for electron in p-region are set as 125 cm^2/s and 9.75 ns, respectively, while those for hole in n-region are set as 31.3 cm^2/s and 30.8 ns, respectively. The surface recombination velocities on the top surface of p-region and the bottom surface of n-region are set as 7.4×10^4 m/s and 0 m/s, respectively. Recombination on the bottom surface of n-region is not considered because the thickness of n-region is much larger than the hole diffusion length. More details about the parameters used in the calculation of photocurrent generation can be found from Ref.[85].

4.2.2 Direct method

Here, TPV performance is calculated based on the energy balance analysis and the effect of applied voltage V on the mean energy of a Planck oscillator ($\Theta(\omega,T)$) is considered by a modified description as

$$\Theta(\omega,T)=\hbar\omega/\left[\exp(\frac{\hbar\omega-qV}{k_{\mathrm{B}}T})-1\right] \tag{4.18}$$

where q is the elementary charge, and V is the applied voltage. As previously mentioned, $\hbar$ is the Planck constant divided by 2π and k_{B} is the Boltzmann constant. The analytical expression of the radiative heat flux exchange from the emitter (medium 1) to receiver layers (medium 2) shown in Figs. 4.1 can be obtained as[112]

$$q_{\omega,1\to2}(\omega)=\frac{2{k_0}^2\Theta(\omega,z,T_1)}{\pi}\times\int_0^{\infty}\mathrm{Re}[i\sum_{i=x,y,z}\varepsilon_{\mathrm{ii}}''(\omega,z)(G_{xi}^{E}G_{yi}^{H^*}-G_{yi}^{E}G_{xi}^{H^*})]\,dz \tag{4.19}$$

where k_0 is the wave vector in vacuum and T, and ε_{ii}'' represent the temperature, and imaginary part of the dielectric function of the emitter layer, respectively and the net heat flux exchange between the emitter and receiver is $q_{12}=q_{1\to2}-q_{2\to1}$. It should be noted that the applied voltage for the emitter would be zero while it is nonzero for the receiver of TPV system. To evaluate the electrical power output, the total applied current density provided inside the PV cell should be calculated as[114]

$$I=q[F_{12}-F_{21}-R(V)] \tag{4.20}$$

where F_{ij} denotes the total number of electron-hole pair generation due the photons with energy greater than the PV cell bandgap emitted from medium i to j as

$$F_{12}=\frac{2}{\pi}\int_{\omega_g}^{\infty}\frac{k_0^2\Theta(\omega,z,T_1)}{\hbar\omega}\{\int_d^{\infty}\mathrm{Re}[i\sum_{i=x,y,z}\varepsilon_{\mathrm{ii}}''(\omega,z)(G_{xi}^{E}G_{yi}^{H^*}-G_{yi}^{E}G_{xi}^{H^*})]\,dz\}\mathrm{d}\omega \tag{4.21a}$$

$$F_{21}=\frac{2}{\pi}\int_{\omega_g}^{\infty}\frac{k_0^2\Theta(\omega,z,T_2,V)}{\hbar\omega}\{\int_{-\infty}^{0}\mathrm{Re}[i\sum_{i=x,y,z}\varepsilon_{\mathrm{ii}}''(\omega,z)(G_{xi}^{E}G_{yi}^{H^*}-G_{yi}^{E}G_{xi}^{H^*})]\,dz\}\mathrm{d}\omega \tag{4.21b}$$

In equation (4.20), $R(V)$ denotes the total radiative and nonradiative recombination rates inside the PV cell. For instance, the nonradiative Auger and Shockley-Read-Hall (SHR) recombinations for a PV cell with a thickness of t are expressed as follows[114]

$$R(V) = (C_n n + C_p p)(np - n_i^2)t + \frac{1}{\tau}\frac{np - n_i^2}{n + p + 2n_i}t \tag{4.22}$$

where n and p are the electron and hole concentrations, respectively and n_i denotes the intrinsic carrier concentration. C_p and C_n represent the Auger recombination coefficients and τ is the bulk Shockley-Read_Hall lifetime. Thus, the efficiency of a TPV system can be described as

$$\eta = \frac{I \times V}{q_{12}} \tag{4.23}$$

In Section 4.4, the performance of a TPV system comprised of a plain planar and a tandem PV cell is calculated by the direct method. Here, GaSb with a bandgap of ω_g = 11.03×10^{14} rad/s and InAs with a bandgap of ω_g = 5.4×10^{14} rad/s are selected as the first and second sub-cell, respectively and Table 1 indicates the corresponding intrinsic carrier concentration and Auger recombination coefficients.

	GaSb	InAs
n_i (cm^{-3})	1.5×10^{12}	6.06×10^{14}
$C_n = C_p$ [cm^6s^{-1}]	2.5×10^{-30}	2.26×10^{-27}

Table 4.1 Intrinsic carrier concentration and Auger recombination coefficients for GaSb and InAs sub-cells.

4.3 TPV Performance Analysis with Multilayer Emitter and Single-Junction Cell

The spectral heat fluxes between the multilayer emitter and the PV cell with different tungsten and alumina layer thickness, are presented in Fig 4.2(a) at vacuum gap distance of d = 100 nm. Moreover, in order to be considered as semi-infinite, a minimum 20 layers with alternating tungsten and alumina needs to be considered for the multilayer emitter, which leads to a relative difference in the total heat flux smaller than 1% compared to that with 40 layers. In order to solely investigate the effect of alumina layer thickness on the spectral near-field radiative transfer, the tungsten layer thickness is fixed at t_W = 10 nm while alumina layer thickness varies from 100 nm to 400 nm. As a comparison, the spectral heat flux between plain tungsten emitter and the PV cell is also presented by the black dash line. It can be clearly seen that the spectral heat flux is much enhanced above the bandgap of PV cell when the plain tungsten emitter is replaced by the multilayer emitter.

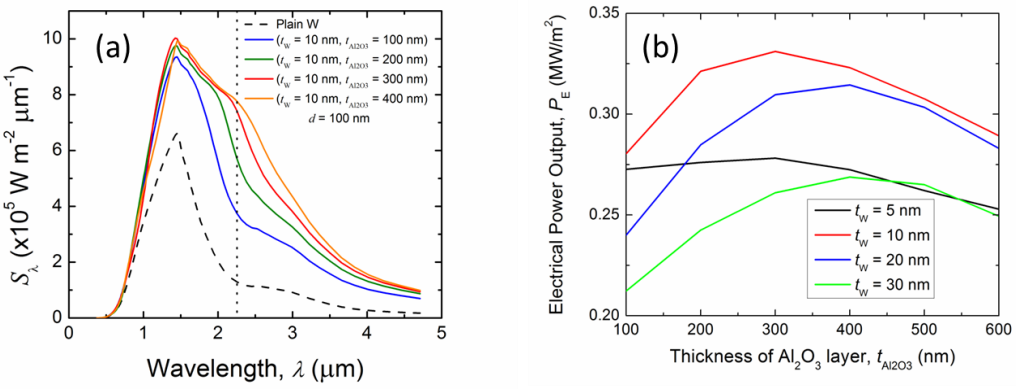

Figure 4.2 (a) Spectral heat fluxes between the multilayer emitter and the receiver when the tungsten layer thickness is set as 10 nm, while the alumina layer thickness is varied. The dash vertical line indicates the bandgap of PV cell. (b) The electrical power output as a function of alumina layer thickness with different values of tungsten layer thickness. The vacuum gap distance d is 100 nm.

However, the spectral heat flux below the energy bandgap of PV cell is also increased due to the type II hyperbolic behavior. In fact, the most portion of energy should be emitted only above the bandgap E_g (i.e., wavelengths smaller than λ_g = 2.22 μm), to minimize the thermalization losses and hence improve the conversion efficiency. In order to optimize both the tungsten and alumina layer thicknesses, the electrical power output calculated by Eq. (4.13) was plotted in Fig 4.2 (b) with different tungsten and alumina layer thickness combinations. Since the spectral heat flux below the bandgap will be significantly reduced due to adding a gold reflector layer, electrical power output is selected as the optimal function instead of conversion efficiency at this time. Based on the result of Fig 4.2(b), it can be concluded that the optimized value of t_W = 10 nm and t_{Al2O3} = 300 nm can maximize the electrical power output and thus, all the results shown in the following paragraphs are based on these geometric dimensions.

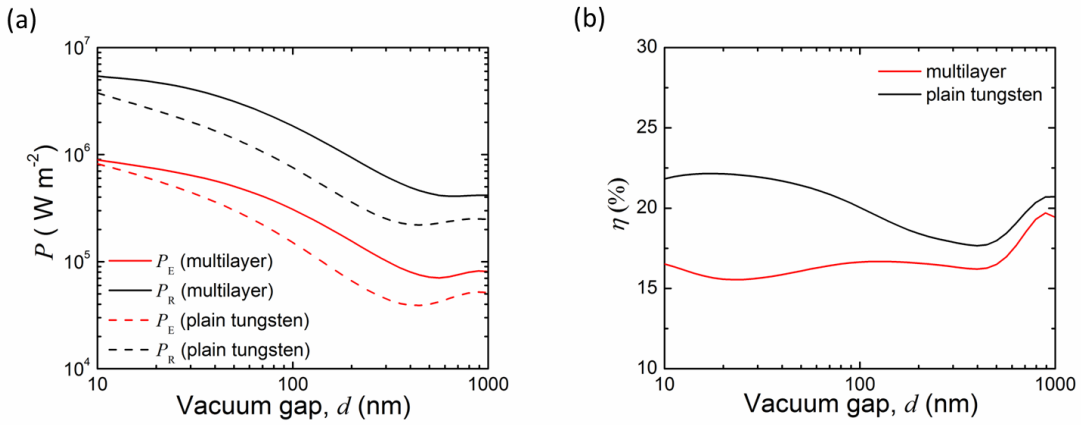

Figure 4.3 (a) The electrical power output and radiative power input, and (b) the conversion efficiency of the TPV system for both multilayer emitter and plain tungsten emitter vs vacuum gap distance.

The electrical power output and radiative power input of the TPV system for both multilayer emitter and plain tungsten emitter are plotted as a function of vacuum gap distance in Fig 4.3(a). Due to enhanced spectral heat flux using the multilayer emitter indicated in Fig 4.2, the radiative power input is enhanced compared to the plain tungsten emitter while the electrical power output is also improved due to the enhanced spectral heat flux above the bandgap of PV cell. However, the increase rate of radiative power input is greater than that of electrical power output and as shown in Fig 4.3(b), the conversion efficiency of the TPV system with the multilayer emitter is actually lower than that with a plain tungsten emitter. A higher electrical power output of about P_E = 0.34 MW/m^2 and a lower conversion efficiency of η = 16.6% of the TPV system with the multilayer emitter are achieved at 100 nm vacuum gap. In fact, due to high heat losses compared with plain tungsten emitter, the conversion efficiency of TPV system using multilayer emitter is decreased.

4.4 TPV Performance Analysis with Planar Emitter and Tandem Cell

Figure 4.4 illustrates a near-field TPV device with an emitter of GZO, separated by a vacuum gap distance of *d* from a tandem cell consisting of p-doped GaSb as the first layer and n-doped InAs as the second layer. The whole setup is also supported by a gold backside reflector to recycle the photons back to the emitter. The thickness of GaSb and InAs sub-cells are set as h = 1.5 μm, and t = 0.5 μm, respectively. The emitter temperature and both PV cells are at T_e = 1800 and T_r = 300 K respectively. These values are assumed as the default ones.

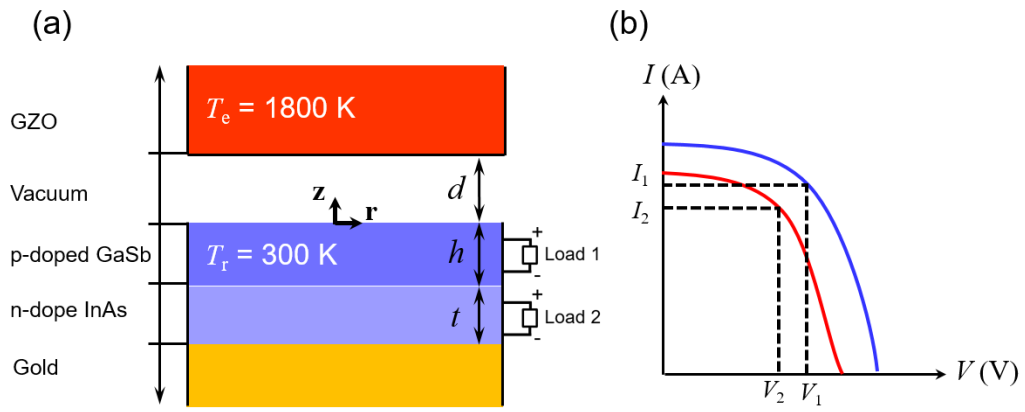

Figure 4.4 The schematic of a TPV system consisting of an emitter made of GZO and a tandem cell with p-doped GaSb and n-doped InAs as the first and second sub-cells, respectively. The thickness of GaSb and InAs sub-cells are set as h = 1.5 μm, and t = 0.5 μm, respectively, and the vacuum gap distance is d = 100 nm.

In this study, the dielectric function of the emitter (GZO) is determined by the Drude-Lorentz model as $\varepsilon(\omega)=\varepsilon_\infty-\frac{\omega_{p1}^2}{\omega(\omega+i\Gamma_p)}+\frac{f_1\omega_1^2}{\omega_1^2-\omega^2-i\omega\Gamma_1}$ in which ε_∞ = 2.475, ω_{p1} = 1.927 eV, Γ_P = 0.117 eV, f_1 = 0.866 eV, ω_1 = 4.850 eV and Γ_1 = 0.029 eV[94,115]. For the first layer of receiver, a p-doped GaSb cell assuming a bandgap of ω_{g1} = 11.03×10^{14} rad/s at a doping level of 1.3×10^{17} cm^{-3} is selected[39]. For the second layer of the receiver, an n-doped InAs cell with a doping level of 2×10^{16} cm^{-3} and a bandgap of ω_{g2} = 5.4×10^{14} rad/s is considered[114]. The material properties of both cells are obtained from Palik's data[102]. However, because of the contributions of free electrons induced by doping, the dielectric function of p-doped GaSb cell is modified by adding an extra Drude term, $-15.1\frac{\omega_{p2}^2}{\omega^2+i\Gamma_D\omega}$ in which plasma frequency and scattering rate are ω_{p2} = 2.6×10^{13} rad/s

and Γ_D = 2.15×10^{13} rad/s, respectively[39]. The optical properties of the gold back reflector at a given angular frequency ω is also described by a Drude model as $\varepsilon_{\text{Drude}}(\omega) = 1 - \frac{\omega_{p3}^2}{\omega^2 + i\Gamma\omega}$ when the plasma frequency is ω_{P3} = 1.37×10^{16} rad/s and the scattering rate is Γ = 7.31×10^{13} rad/s[51]. It should be mentioned that PV tandem cells can be connected in series or can be functioning separately. In a series connection, the current would be the same for each cell while with a separate connection between the top and the bottom cells does not impose any limitation on the current production. As shown in Fig. 4.4(b), a separate connection is considered in this work and the total efficiency would be the summation of the best efficiency of each individual cell (i.e., $\eta_{\text{tandem cell}} = \frac{(I_1 \times V_1) + (I_2 \times V_2)}{q_{12}}$). Here, q_{12} indicates the total heat exchange between the emitter and receiver layers. It should be noted that as the number of PV cells increases or a separate connection between PV cells is chosen, the efficiency of the stack potentially increases while this efficiency improvement is achieved at the cost of increased complexity and manufacturing price. The obtained numerical results indicating the total heat flux exchange between emitter and receiver layers, electric current, and conversion efficiency are shown in table 4.2 for a TPV system with a tandem cell structure comparing to a TPV system composed of an only one cell made of either p-doped GaSb or n-doped InAs cell with a thickness of 2 μm. In this study, Auger recombination is also considered in the evaluation of the current density.

TPV cell (s)	Cell thickness (μm)	Total heat flux exchange (kW/m^2)	Electric current (kW/m^2)	Efficiency%
n-doped InAs	2	692.7	196.6	28.3
p-doped GaSb	2	422.9	146.3	34.5
p-doped GaSb n-doped InAs	1.5 0.5	616.1	133.3 111.1	39.1

Table 4.2 Numerical results of the total heat flux exchange between emitter and receiver layers, electric current, and conversion efficiency for a TPV device with either a tandem cell or an individual cell. Auger recombination is considered in the evaluation of the current density and the total thickness of tandem cell structure or the thickness of an individual cell in a single stack structure is 2 μm.

Considering a conversion system with an n-doped InAs as the only PV cell with a thickness of 2 μm, the total heat flux exchange from emitter to the receiver (including both cell and gold back reflector) and the electric current would be 692.7 kW/m^2 and 196.6 kW/m^2, respectively resulting in an efficiency of 28.3%. Similarly, a conversion system with a single PV cell made of p-doped GaSb with a thickness of 2 μm, has a total heat flux exchange and electric current of 422.9 kW/m^2 and 146.3 kW/m^2, respectively. The efficiency of this system consequently calculated as 34.5%. In fact, a TPV system with a single PV junction cannot make an excellent use of the emitted spectrum since the photons with energies less than the bandgap of PV cell cannot contribute to the power output. Tandem cell on the other hand, is advantageous since low-energy photons can pass through the first PV cell and contribute to the electron-hole pair generation in the second PV cell. Several numerical simulation have been performed to finally identify the optimum thicknesses for GaSb and InAs sub-cells as $h = 1.5$ μm, and $t = 0.5$ μm,

respectively in a tandem structure. As demonstrated in table 4.2, using a tandem cell in a near-field thermophotovoltaic system results in an enhanced conversion efficiency and electrical power output of 39.1% and 244.4 kW/m^2, respectively. Hence, in a TPV system with a tandem structure, a conversion efficiency improvement of 4.6% and 10.8% can be achieved comparing to a 2 μm-single GaSb cell and a 2 μm-single InAs cell, respectively. This enhancement is due to the enhanced absorption in each layer of PV cells where photons with higher energy would be absorbed by the first layer (GaSb) while the ones with lower energy are absorbed in the second cell (InAs).

CHAPTER 5

IMPACT OF MAGNETIC POLARITONS ON NEAR-FIELD THERMOPHOTOVOLTAIC SYSTEMS

In this chapter, we study the effect of magnetic polariton (MP) on the conversion performance of a near-field thermophotovoltaic (TPV) system made of a nanostructured Drude grating emitter and a nanometer-thick photovoltaic (PV) cell with a lossless metal as the backside reflector. Section 5.1 gives the near-field radiative heat flux calculated through scattering matrix theory coupled with rigorous coupled-wave analysis based on fluctuational electrodynamics. The enhanced spectral radiative heat flux between Drude emitter and thin PV cell and for the base geometry values are discussed in Section 5.2. Contour plots of energy transmission coefficient and an inductor-capacitor circuit model along with magnetic field distribution are presented in Section 5.3 to verify and understand the MP excitation in the near-field. Finally, effects of PV cell thickness and vacuum gap distances are systematically investigated on the near-field radiative heat flux, electrical power output, and energy conversion efficiency in Section 5.4 and 5.5, respectively.

5.1 Theory of Scattering Matrix Method Incorporated with Rigorous Coupled Wave Analysis

Near-field radiative heat flux q between the grating structures can be obtained using the scattering matrix theory[116-118]

$$q = \int_0^\infty q_\omega d\omega = \frac{1}{2\pi^3}\int_0^\infty \left[\Theta(\omega, T_1) - \Theta(\omega, T_3)\right]\left[\int_0^{\pi/\Lambda}\int_0^\infty \xi\left(\omega, k_{x0}, k_y\right) dk_y dk_{x0}\right] d\omega \quad (5.1)$$

Note that q_ω is the net spectral heat flux absorbed by the receiver. As previously discussed, the function $\Theta(\omega,T)=\hbar\omega/\left(e^{\hbar\omega/k_BT}-1\right)$ is the average energy of a Planck's oscillator at a given angular frequency ω and temperature *T*, k_{x0} and k_y are the wavevector components in *x* and *y* directions, and $\xi(\omega, k_{x0}, k_y)$ is the energy transmission coefficient defined by[118]

$$\xi\left(\omega,k_{\mathrm{x0}},k_{\mathrm{y}}\right)=\mathrm{tr}\left(\mathbf{D}\mathbf{W}_1\mathbf{D}^{\dagger}\mathbf{W}_2\right) \tag{5.2}$$

where

$$\mathbf{D}=\left(\mathbf{I}-\mathbf{S}_1\mathbf{S}_2\right)^{-1} \tag{5.3a}$$

$$\mathbf{W}_1=\Sigma_{-1}^{pw}-\mathbf{S}_1\Sigma_{-1}^{pw}\mathbf{S}_1^{\dagger}+\mathbf{S}_1\Sigma_{-1}^{ew}-\Sigma_{-1}^{ew}\mathbf{S}_1^{\dagger} \tag{5.3b}$$

$$\mathbf{W}_2=\Sigma_{1}^{pw}-\mathbf{S}_2^{\dagger}\Sigma_{1}^{pw}\mathbf{S}_2+\mathbf{S}_2^{\dagger}\Sigma_{1}^{ew}-\Sigma_{1}^{ew}\mathbf{S}_2 \tag{5.3c}$$

Here, $\mathbf{S}_1$ and $\mathbf{S}_2$ are calculated by the reflection matrixes $\mathbf{R}_1$ and $\mathbf{R}_2$ obtained by rigorous coupled-wave analysis (RCWA) method[118-120], while operators $\Sigma_n^{pw/ew}$ were clearly presented in Ref. [118]. The main idea of this method is based on the Floquet's theorem that the solutions of periodic differential equations can be expanded with Bloch waves. After multiple scattering in the periodic grating structure, the reflected electromagnetic wave is expanded to a series of diffracted ones with different orders. Assuming a 1D grating periodically arranged in *x* direction, the *x* component of the wavevector for *j*th order $k_{x,j}$ is determined from the Bloch-Floquet condition

$$k_{x,j}=\frac{2\pi}{\lambda}\sin\theta+\frac{2\pi}{\Lambda}\,j \tag{5.4}$$

where λ is the wavelength, θ is the incident angle, and Λ is the grating period. After applying the boundary conditions at each interface, the reflectance for each diffraction order can be calculated, and the total reflectance would be the summation of them. Note that the convergence of RCWA strongly depends on the total diffraction orders, so that they should be carefully checked to be sufficient for the following calculations. However, RCWA is efficient to obtain radiative properties for 1D gratings, it is very computationally expensive for 2D gratings and even more complex nanostructures. More details can be found in Refs. [119-121].

5.2 Spectral Near-Field Radiative Flux between a Drude Grating Emitter and an Ultrathin TPV Cell with Perfect Back Reflector

Figure 5.1(a) illustrates a near-field TPV device comprised of a one-dimensional metallic grating emitter, a thin PV cell, and a lossless metal as the backside reflector. The grating emitter geometry is set as period $\Lambda = 0.6$ μm, depth $h = 0.5$ μm, and ridge width $w = 0.3$ μm. The filling fraction is then defined as $f = w/\Lambda$. $In_{0.18}Ga_{0.82}Sb$ is chosen as the material for the PV cell at $T_3 = 300$ K with thickness t, and is separated from the grating emitter at $T_1 = 1000$ K by a vacuum gap distance d. These values are assumed as the default ones unless specified otherwise. The optical properties of $In_{0.18}Ga_{0.82}Sb$ with a bandgap of 0.56 eV are obtained from Palik's data[102]. It should be noted that the fabrication of a thin-layer of semiconductor materials on silicon[122] and metallic substrate[123] has been experimentally demonstrated. In order to recycle the photons back to the emitter and minimize the thermalization losses, a lossless metal is used as the backside reflector for the PV cell. Optical properties of the metallic grating emitter and

the back reflector at a given angular frequency ω are described by a Drude model as $\varepsilon_{\text{Drude}}(\omega) = 1 - \frac{\omega_p^2}{\omega^2 + i\Gamma\omega}$. For the grating emitter, the plasma frequency is ω_{P1} = 1.37×10^{16} rad/s and the scattering rate is Γ_1 = 7.31×10^{13} rad/s, both of which are taken from the material properties of gold at room temperature[51]. On the other hand, the backside reflector is assumed to have the same plasma frequency as the emitter (i.e., ω_{P4} = ω_{P1}) with zero scattering rate (i.e., Γ_4 = 0) to exclude the possible absorption by the reflector, which cannot be calculated by current theoretical model.

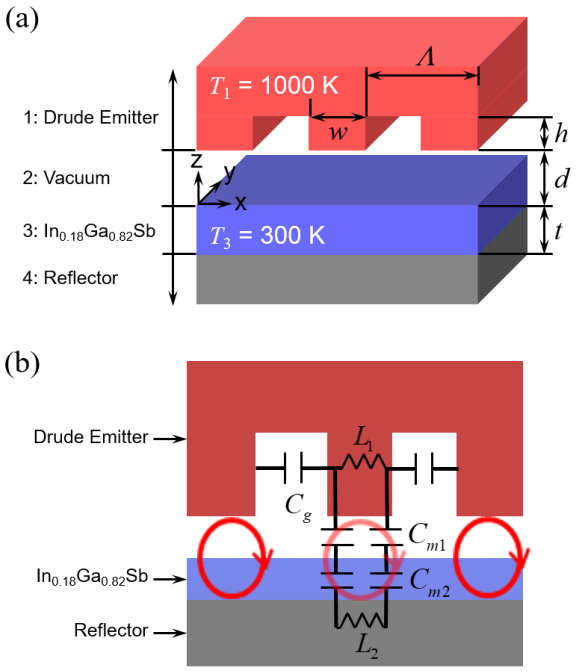

Figure 5.1 (a) Schematic of a near-field TPV with the grating parameters of period (Λ), depth (*h*), and ridge width (*w*). The emitter and receiver temperatures are respectively set as T_1 = 1000 K, and T_3 = 300 K in this study. The cell thickness is denoted as *t* and the vacuum gap distance is *d* = 50 nm. (b) LC circuit model of the corresponding TPV system is constructed to predict the MP resonance frequency.

Note that an internal quantum efficiency (η_q) of 100% is assumed in this work and the surface and bulk recombination losses are not considered in the electrical model. This assumption might lead to over-predict the conversion efficiency of the near-field TPV system. While bulk recombination losses for minority carriers can be greatly reduced since the entire sub-100-nm cell layer can be treated as the depletion region,[30] bulk recombination due to the lateral diffusion and surface recombination could be severe. Surface passivation can be used to possibly reduce surface recombination, while electron-hole recombination due to lateral diffusion might be alleviated by placing the top electrode nearby the grating ridges where MP is excited.

The spectral heat flux between the Drude grating emitter and thin-film $In_{0.18}Ga_{0.82}Sb$ cell with a lossless metal on the back is shown in Fig. 5.2. For simulation 1 shown in Figure 5.2, a total of 81 diffraction orders was used to obtain $\mathbf{R}_1$ and $\mathbf{R}_2$ while a total of 45 and 170 data points was respectively used for k_{x0} and k_y wavevectors. The upper limit of k_y was set to $40\omega/c$ and a total of 180 angular frequency values were evenly spanned over a frequency range from 3×10^{14} rad/s to 2.5×10^{15} rad/s, which ensures the relative error of q less than 1% compared to the case of doubling all the numbers (i.e., simulation 2 in Figure 5.2). As a comparison, the results for a planar emitter with either a semi-infinite or a thin-film $In_{0.18}Ga_{0.82}Sb$ cell supported by a backside reflector are also plotted in Fig. 5.2. Vacuum gap distance d is kept as 50 nm for all cases. When both the planar emitter and PV cell are semi-infinite, the main part of spectral heat flux is below the bandgap of the $In_{0.18}Ga_{0.82}Sb$, i.e. 8.5×10^{14} rad/s, which means that most of the radiative transfer could not generate electricity, resulting in a low conversion efficiency of 1.5%.

In order to reduce the unusable portion of spectral radiative energy transport in the frequency range below the bandgap, a thin-film of $In_{0.18}Ga_{0.82}Sb$ cell is employed when a lossless reflector is added to be on the back of the PV cell[30,87]. Compared with the semi-infinite cell case, when a thin-film cell is placed on a metal reflector, one can clearly see a significant drop for the energy transfer below the bandgap. This is due to that most of the energy below the bandgap has a large penetration depth in the cell and is reflected on the surface of the backside reflector to the emitter[30,87]. While the unusable energy transfer below the bandgap is decreased, the part above the bandgap has also been suppressed as shown in Fig. 5.2 because part of the energy above the bandgap is also reflected back due to the ultra-thin thickness of the cell. The combination of these effects results in an improved conversion efficiency of 15.3%.

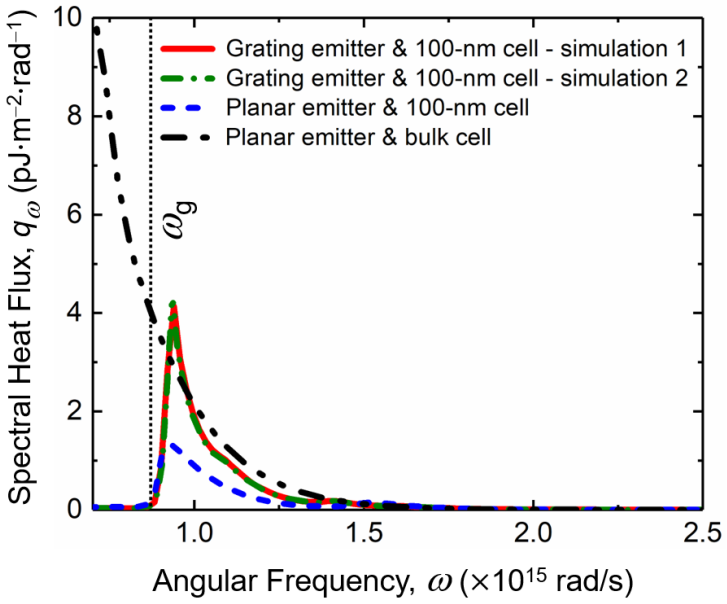

Figure 5.2 Spectral heat fluxes for grating and planar emitters with thin-film PV cell of t = 100 nm, and planar emitter with semi-infinite PV cell at vacuum gap of 50 nm. The PV cell bandgap of 8.5×10^{14} rad/s is shown with a vertical dotted line. Numerical simulations 1 and 2 are defined in Section 5.1.

A Drude grating emitter with aforementioned base geometry values is employed to possibly further enhance the spectral heat flux above the PV cell bandgap by exciting magnetic polariton within nanometric vacuum gaps as previously reported by Ref. [51]. It is observed that there exists a narrow band enhancement on the spectral heat flux at ω = 9.1×10^{14} rad/s with a peak value about 3.1 times higher than that of planar emitter. As a result, the conversion efficiency of the near-field TPV system is further improved from 15.3% to 19.2% when the planar emitter is replaced by the grating one.

5.3 Verification of Magnetic Polariton Excitation

In order to clarify the mechanism behind the spectral heat flux enhancement at ω = 9.1×10^{14} rad/s when applying the grating emitter with thin-film cell and backside reflector, the contour plots of energy transmission coefficient (ξ) are analyzed in Fig. 5.3.

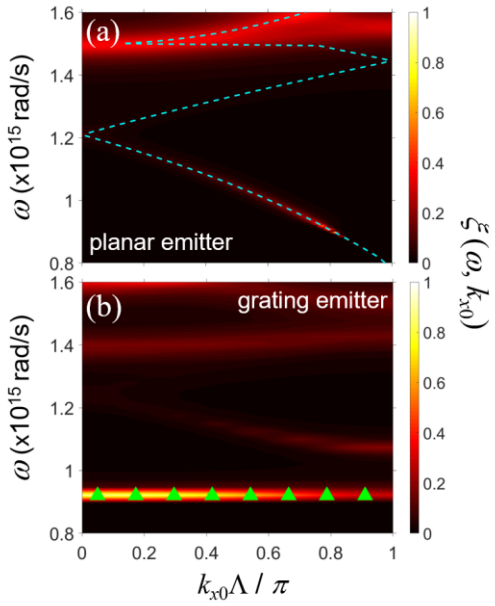

Figure 5.3 Contour plot of energy transmission coefficient (ξ) between (a) the planar emitter, (b) the grating emitter and the $In_{0.18}Ga_{0.82}Sb$ cell with t = 100 nm at a vacuum

gap of 50 nm. The dispersion for SPPs coupling is shown with a blue dash line in (a) and MP resonance frequency predicted by the LC circuit model is presented with green triangles in (b).

Note that the energy transmission coefficients for TPV structures with planar emitter and grating emitter are presented respectively in Fig. 5.3(a) and Fig. 5.3(b) as a function of angular frequency (ω) and normalized x component of wavevector ($k_{x0}\Lambda/\pi$) under $k_y = 0$. The cell thickness is set as t = 100 nm and the vacuum gap d is 50 nm. In order to fully understand the enhancement bands shown in Fig. 5.3, the coupled SPPs mode between the planar Drude emitter and the lossless metal backside reflector is calculated via

$$\left|1 - r_1^p R_3^p e^{i2\gamma_2 d}\right| = 0 \tag{5.5}$$

where

$$R_3^p = \frac{r_{2,3}^p + r_{3,4}^p e^{i2\gamma_3 t_3}}{1 + r_{2,3}^p r_{3,4}^p e^{i2\gamma_3 t_3}} \tag{5.6}$$

Here, the subscripts 1, 2, 3 and 4 denote the emitter layer, vacuum gap, TPV receiver and metal backside reflector, respectively. γ is the wavevector component vertical to the interface and r^p is Fresnel reflection coefficient for p polarization. Based on the good agreement between the transmission coefficient enhancement bands and the dispersion curve represented as the blue dash line in Fig. 5.3(a), it can be verified that the enhancement bands at higher frequency ranges are due to the SPP coupling between the Drude planar emitter and the metal backside reflector.

SPP coupling is also responsible for most enhancement bands shown in Fig. 5.3(b) for the Drude grating emitter case, while there is a bright horizontal band at the

frequency around $\omega = 9.1\times10^{14}$ rad/s which is not identified yet. It should be noticed that this enhancement band is independent of k_{x0}. This behavior is similar to the characteristic of magnetic polariton mode which has been studied previously in near-field[51,52] and far field regime[54-56], suggesting that MP excitation may be responsible for this enhancement. Since MP is a result of local electromagnetic energy confinement, an equivalent LC circuit model as depicted in Fig. 5.1(b) could be employed to predict MP resonance frequency by zeroing the total impedance[53]

$$Z_{\text{tot}} = i\omega[\frac{L_{\text{m1}} + L_{\text{k1}}}{1-\omega^2 C_{\text{g}}(L_{\text{m1}} + L_{\text{k1}})} - \frac{2}{\omega^2 C_{\text{m}}} + L_{\text{m2}} + L_{\text{k2}}] \tag{5.7}$$

Here, $L_{\text{m}} = 0.5\mu_0 w(d+t)$ denotes the contribution of mutual parallel-plate inductance between the emitter ridge with width *w* and perfect metal reflector separated by a vacuum gap *d* and a cell thickness *t*. The kinetic inductance is expressed as $L_{\text{k}} = -w/(\varepsilon_0 \varepsilon'_{\text{m}} \omega^2 \delta)$, where $\delta = \lambda/(4\pi\kappa)$ is the penetration depth with κ being the extinction coefficient of the metal and ε'_{m} represents the real part of the dielectric function of the metal. Note that μ_0 and ε_0 are the absolute magnetic permeability and electric permittivity of vacuum. Total parallel-plate capacitance between the upper and lower metal layers is defined as $C_{\text{m}} = \frac{C_{\text{m1}} C_{\text{m2}}}{C_{\text{m1}} + C_{\text{m2}}}$ where $C_{\text{m1}} = c_1 \varepsilon_0 w/d$ and $C_{\text{m2}} = c_1 \varepsilon_0 \varepsilon_{\text{InGaSb}} w/t$ respectively account for the capacitance of vacuum and PV cell with the non-uniform charge distribution factor considered as c_1 = 0.3. The gap capacitance inside the grating emitter grooves is calculated by $C_{\text{g}} = \varepsilon_0 h/(\Lambda - w)$.

The MP resonance frequency predicted by the LC circuit model is shown as the green triangles in Fig. 5.3(b) for vacuum gap of 50 nm, which is in good agreement with the energy transmission enhancement band observed at frequency of $\omega = 9.1\times10^{14}$ rad/s. This excellent match confirms that the excitation of MP inside the vacuum gap of the near-field TPV along with coupled SPPs resonance are the main mechanisms responsible for the spectral heat flux peak, leading to spectral selectivity of radiative transport and thereby the improved conversion efficiency.

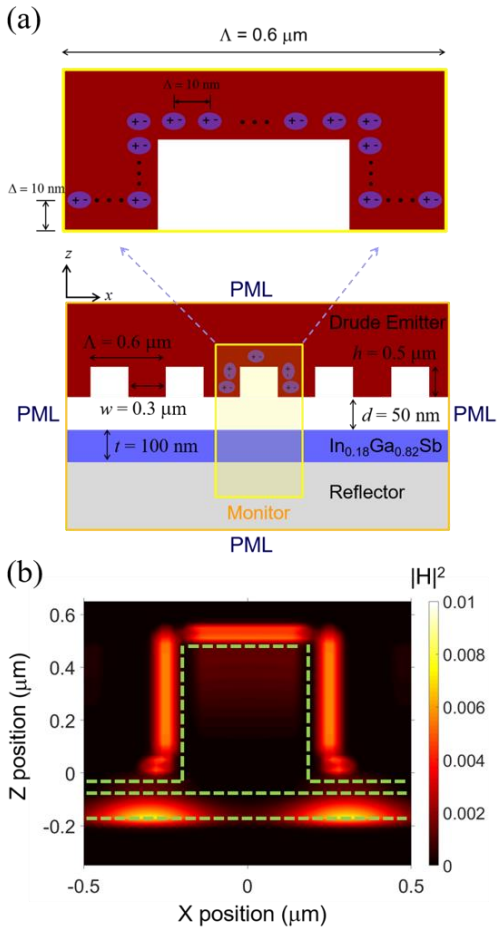

Figure 5.4 (a) Schematic of the applied electric dipoles to simulate magnetic field of *p*-polarized waves inside the PV cell at $\omega = 9.1\times10^{14}$ rad/s (MP resonance frequency) in

FDTD software. (b) Contour plot of magnetic field in TPV system at d = 50 nm when geometric parameters are set at default values.

To further verify that MP resonance frequency occurs at $\omega = 9.1\times10^{14}$ rad/s, corresponding magnetic field distribution is calculated by finite-difference time-domain method. As shown in Fig. 5.4(a), boundary conditions are set as perfectly matched layers, while electric dipole sources oscillate in x and z direction, whose magnetic fields are summed up incoherently to present the effect of p-polarized waves. The distance of electric dipole sources with their neighbors and their depth away from the surface of Drude grating emitter are set as 10 nm. Fig. 5.4(b) presents the resulting magnetic field at $\omega = 9.1\times10^{14}$ rad/s and clearly there is a strong field confinement inside the ultra-thin $In_{0.18}Ga_{0.82}Sb$ layer between the Drude grating emitter and the backside reflector. This demonstrates the exact behavior of MP excitation, which causes the spectral radiative heat flux enhancement at this frequency as shown in Fig. 5.2.

5.4 Effects of Cell Thickness on Electric Power and Conversion Efficiency

To gain more insights on the physical behavior of MP mode in near-field radiative transfer, the effect of PV cell thickness on MP excitation is investigated in terms of energy transmission coefficient as observed from Figs. 5.5(a-d). The LC circuit model prediction is also plotted as the green triangles. It should be noted that the accuracy of LC circuit model is subject to the non-uniform charge distribution factor. For simplicity, the value of c_1 is considered 0.3 which can still reasonably predict MP resonance frequency for different cases. Based on the LC model, the capacitance of the PV cell (i.e., C_{m2}) is inversely proportional to the cell thickness, while a thicker PV cell will increase the

mutual inductor (i.e., L_m). From the calculation, the LC model predicts that MP resonance frequency shifts from 1.21×10^{15} rad/s to 9.1×10^{14} rad/s as $In_{0.18}Ga_{0.82}Sb$ cell thickness t varies from 10 nm to 100 nm. It is found that when $In_{0.18}Ga_{0.82}Sb$ thickness is set as t = 100 nm, MP frequency matches well with the cell bandgap and it would lead to a high TPV performance.

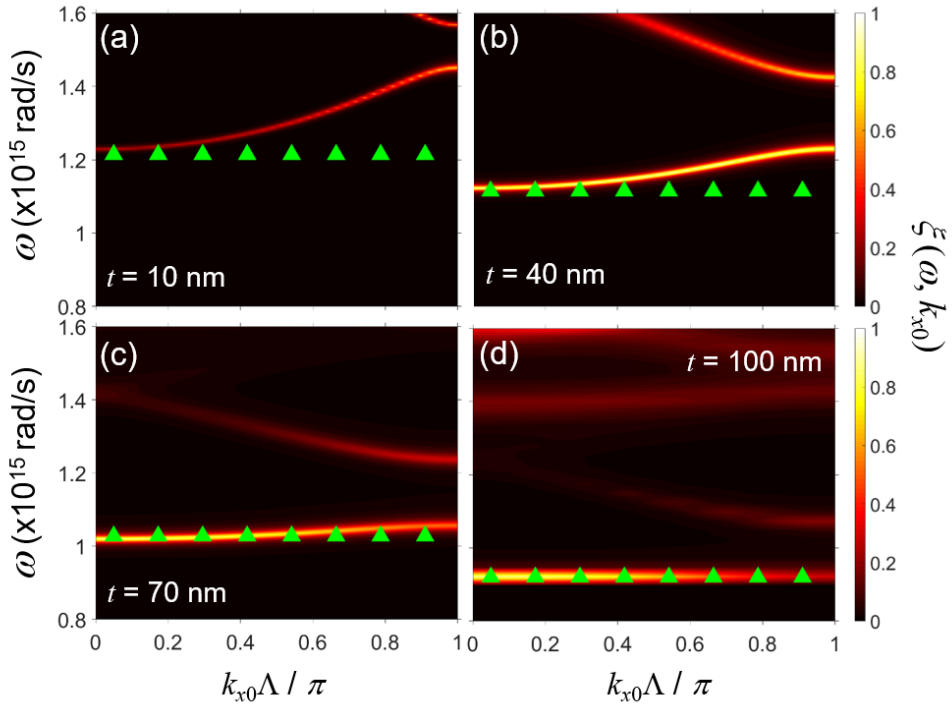

Figure 5.5 Contour plot of energy transmission coefficient (ξ) between the grating emitter and PV cell for different cell thickness. (a) t = 10 nm, (b) t = 40 nm, (c) t = 70 nm and (d) t = 100 nm. Note that vacuum gap width is assumed as 50 nm.

In order to further investigate the effect of TPV cell thickness on MP, the performance of the near-field TPV system with the grating emitter is compared with the one with the planar emitter. The total radiative heat flux, electrical power generation, and conversion efficiency of the near-field TPV systems as a function of PV cell thickness are

plotted in Figs. 5.6(a), (b) and (c), respectively. It can be observed that total radiative heat flux and electrical power output of near-field TPV systems with either planar or grating emitter increase as TPV cell thickness increases.

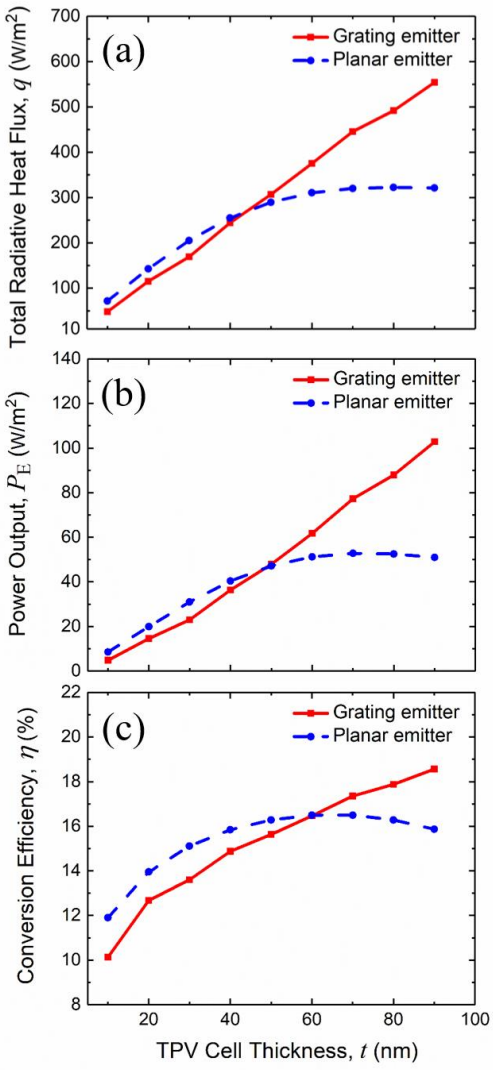

Figure 5.6 The effect of PV cell thickness on (a) total radiative heat flux and (b) electrical power generation, and (c) conversion efficiency for a near-field TPV with both planar and grating emitter at vacuum gap distance of 50 nm.

As it has been already explained, the MP resonance frequency matches better with the cell bandgap as cell thickness increases. Hence, the contribution from MP at larger

cell thicknesses enhances the near-field TPV performance when the planar emitter is replaced by a grating one. In addition, TPV system with the planar emitter has a higher radiative power and electrical power output when cell thickness is smaller than about 50 nm. The same trend can be seen for TPV conversion efficiency. However, radiative power, electrical power output and conversion efficiency of the TPV device with the grating emitter become higher than the planar case at larger cell thickness.

5.5 Effects of Vacuum Gap on Electric Power and Conversion Efficiency

The total radiative heat flux, electrical power generation, and conversion efficiency of the near-field TPV system with both grating emitter and planar emitter as a function of the vacuum gap distance are plotted in Fig. 5.7(a), (b) and (c), respectively**.** For all cases, the thickness of the thin-film cell is set as t = 100 nm. As it mentioned previously, the PV cell quantum efficiency is assumed as 100% since the PV cell is an ultra-thin receiver and the whole cell is considered in depletion region[30]. As shown in Fig. 5.7(a), for both the planar and grating emitter cases, as the vacuum gap distance decreases, the transition from the far field to near-field regime around 1 μm would increase the radiative flux significantly due to the contribution of evanescent waves coupling. When the vacuum gap distance is beyond 1 μm, the total radiative heat flux almost saturates because the propagating waves start to dominate the radiative heat transfer and it is independent on the vacuum gap distance. Fig. 5.7(b) demonstrates that the contribution of evanescent waves increase the electrical power output in smaller vacuum gap distances, accordingly. On the other hand, compared with the case of a planar emitter, the one with the grating emitter has a higher total heat flux and electrical

power output. It can be explained as the excitation of MP above the PV cell bandgap at smaller vacuum gap distances. However, when the vacuum gap increases, the MP resonance becomes weaker and the surface plasmon polariton (SPP) coupling is the main reason to cause the enhancement as studied previously in Ref. 92.

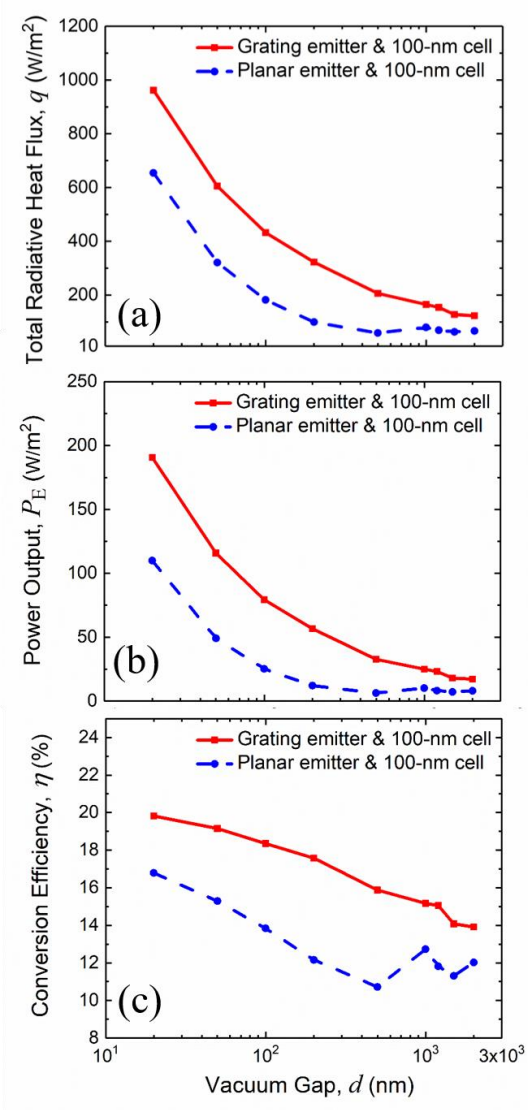

Figure 5.7 The effect of vacuum gap distance on (a) total radiative heat flux and (b) electrical power generation, and (c) conversion efficiency for a near-field TPV with both planar and grating emitter.

Similar phenomena can be observed for the conversion efficiency as shown in Fig. 5.7(c). The near-field TPV with a grating emitter always possesses a higher conversion efficiency due to the MP excitation at small vacuum gap and SPPs coupling at large vacuum gap. The highest conversion efficiency for grating emitter case can be achieved as 19.8% at d = 20 nm compared with 16.8% for the planar case. In addition, the maximum conversion efficiency improvement of 5.4% is observed at d = 200 nm that can be explained by excitation of MP and SPPs coupling. It should be also noticed that a near-field TPV system containing a grating emitter reaches to conversion efficiency of 19.2% and electrical power output of 115.9 W/m^2 at vacuum gap distance of d = 50 nm showing an improvement over the planar case by 3.9% and 136% for efficiency and power, respectively. This enhancement is mostly due to MP excitation inside the PV cell as it is illustrated here in near-field TPV application for the first time.

CHAPTER 6

THEORETICAL STUDY OF NEAR-FIELD THERMAL RADIATION BETWEEN POLAR GRATING METAMATERIALS

The excitation of phonon mediated MP in the SiC grating grooves and its effect on the near-field radiative heat transfer is the main focus of this chapter. In Section 6.1, the spectral radiative heat transfer and the total heat flux for both planar and grating structures are compared. In Section 6.2, the excitation of magnetic polaritons as the main mechanism is discussed. An Inductor-capacitor model and contour plots of energy transmission and magnetic distribution of SiC grating structures will be studied to further explore the main mechanisms. Next, the effect of geometrical parameters on the resonance frequency of MP are investigated in Section 6.3. Finally, the near-field thermal radiation in a sphere-plate configuration is numerically presented in Section 6.4.

6.1 Near-field Radiative Transfer between SiC Deep Grating Metamaterials

As depicted in Fig. 6.1(a), the grating period, depth, and ridge width for the reference geometry are denoted as Λ = 5 μm, h =1 μm, and w = 4.5 μm, respectively. The grating filling ratio is then $f = w/\Lambda = 0.9$. The temperatures of emitter and receiver are T_1 = 400 K and T_2 = 300 K, respectively. The scattering formalism[116,118] that is incorporated into fluctuation electrodynamics with rigorous coupled-wave analysis (RCWA)[119,120] is employed to exactly calculate the near-field radiative heat flux. The dielectric function of SiC is described by a Lorentz model[12] as $\varepsilon_{\mathrm{SiC}}(\nu) = \varepsilon_\infty(1+\frac{\nu_{\mathrm{LO}}^2-\nu_{\mathrm{TO}}^2}{\nu_{\mathrm{TO}}^2-i\gamma\nu-\nu^2})$, where ν is the frequency in wavenumber, the high-frequency constant ε_∞ is 6.7, the longitudinal optical-

phonon frequency ν_{LO} is 969 cm^{-1}, the transverse optical-phonon frequency ν_{TO} is 793 cm^{-1}, and scattering rate γ equals 4.76 cm^{-1} at room temperature.

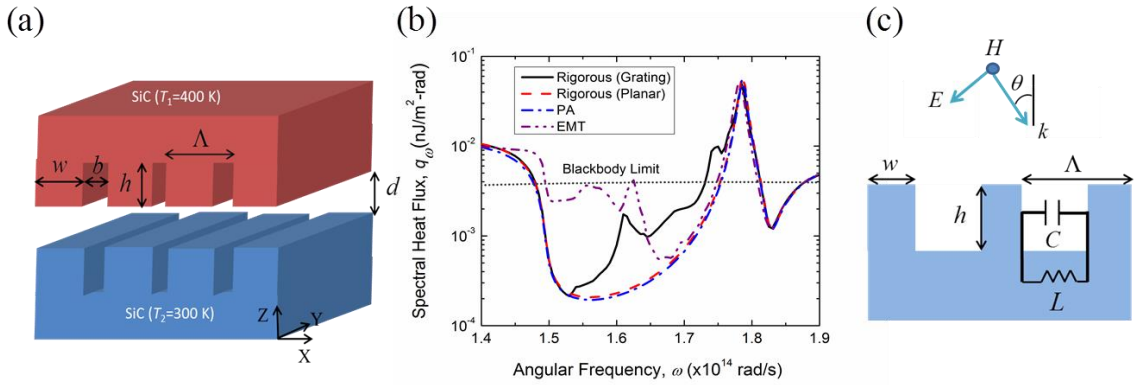

Figure 6.1 (a) Schematic of radiative heat transfer between two symmetric SiC deep gratings. The emitter and receiver temperatures are respectively set as T_1 = 400 K, and T_2 = 300 K in this study. (b) Spectral heat fluxes between two aligned SiC gratings at d = 1 μm calculated from rigorous scattering theory, EMT and PA method. The spectral heat fluxes between two SiC plates at d = 1 μm, and far-field blackbody limit are presented. The grating geometry is set as the default. (c) Corresponding LC circuit model of a 1D grating structure.

In Fig. 6.1(b), the spectral radiative heat fluxes between two SiC gratings predicted by rigorous scattering matrix method (denoted as Grating case), EMT and PA method are compared with planar surfaces and far-field blackbody limitation. Note that the default grating parameters are used and the vacuum gap distance is d = 1 μm. For the planar case, a significantly enhanced spectral heat flux around 1.79×10^{14} rad/s has been observed, which is well known as the strong SPhP coupling between SiC plates in near-field. Unlike the planar case, besides the enhanced spectral heat flux around 1.79×10^{14} rad/s due to strong SPhP coupling, there are two additional peaks at frequencies around ω = 1.61×10^{14} rad/s and ω = 1.75×10^{14} rad/s for the grating case. In order to explore the

underlying mechanism for these additional peaks, the spectral heat fluxes between SiC gratings calculated by EMT and PA method are investigated.

The Derjaguin's proximity approximation (PA) method considers a weighted heat transfer between plates. Therefore, the PA method can only consider the SPP/SPhP coupling between two planar surfaces. For one dimensional grating with filling ratio $f = w/\Lambda$ and no lateral shift, the radiative heat flux can be predicted by PA as[124]

$$q_\omega^{\mathrm{PA}} = f \times q_\omega^{\mathrm{plate}}(d) + (1-f) \times q_\omega^{\mathrm{plate}}(d+2h) \tag{6.1}$$

where $q_\omega^{\mathrm{plate}}(d)$ and $q_\omega^{\mathrm{plate}}(d+2h)$ are the spectral heat fluxes between two plates at a gap distance of d and $d+2h$, respectively. Note that h denotes the depth of gratings. The PA method predicts almost the same spectral heat flux with planar case, which is because it is an approximate method to consider the weighted sum of planar contributions and the filling ratio is as large as 0.9. The spectral heat flux between two SiC gratings calculated by EMT method can be obtained by setting up the diffraction order in the rigorous scattering matrix theory as 0, i.e.

$$q_\omega^{\mathrm{EMT}} = q_\omega(N=0) \tag{6.2}$$

where q_ω is the spectral heat flux, and N is the diffraction order used to calculate the reflection coefficient through RCWA. Note that by setting up $N = 0$, the k_{x0} range cannot be limited by π/Λ anymore and a sufficiently large one should be provided. As predicted by the EMT method, besides the spectral heat flux peak due to SPhP coupling similar to planar case, another broadband enhancement from 1.5 to 1.64×10^{14} rad/s has been observed. In order to explain this enhancement predicted by EMT method, the Maxwell-Garnett theory, is applied to express the effective dielectric functions as [125]

$$\varepsilon_{\mathrm{O}} = 1 - f + \varepsilon_{\mathrm{SiC}} f \tag{6.3}$$

$$\varepsilon_{\mathrm{E}} = \frac{\varepsilon_{\mathrm{SiC}}}{(1-f)\varepsilon_{\mathrm{SiC}} + f} \tag{6.4}$$

where the subscript "O" and "E" denote the ordinary and extraordinary component of dielectric function, respectively.

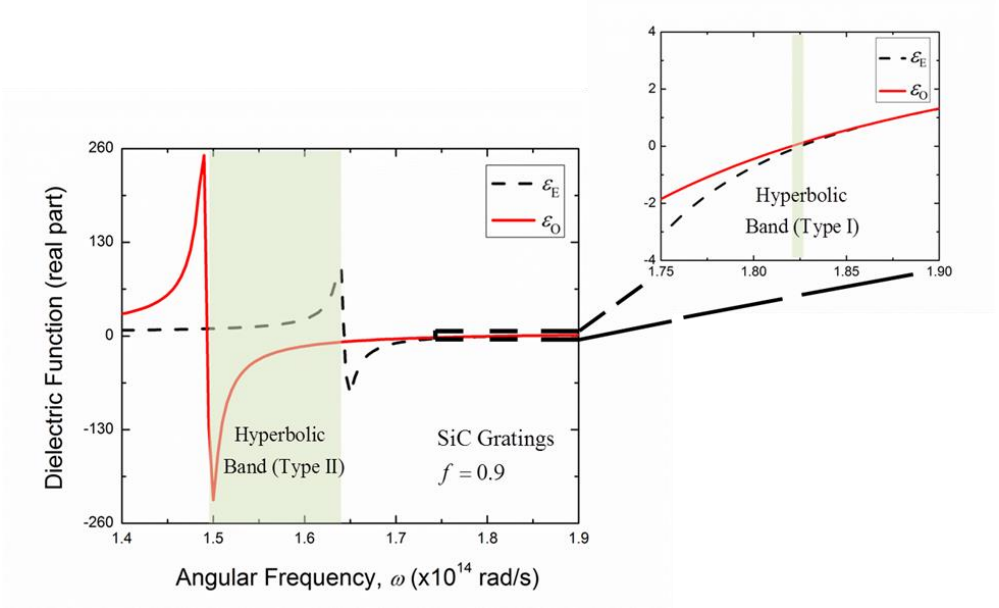

Figure 6.2 Effective dielectric functions (real part only) for SiC gratings with f = 0.9. The hyperbolic dispersions are supported in two narrow bands between 1.5×10^{14} and 1.64×10^{14} rad/s, and between 1.82×10^{14} and 1.83×10^{14} rad/s as shown by shaded regions.

As the optical axis of considered grating structure is along x axis shown in Fig. 6.1(a), it gives $\varepsilon_{\mathrm{xx}} = \varepsilon_{\mathrm{E}}$, and $\varepsilon_{\mathrm{yy}} = \varepsilon_{\mathrm{zz}} = \varepsilon_{\mathrm{O}}$. The real parts of the dielectric function in orthogonal directions ε_{O} and ε_{E} of SiC gratings calculated by Eqs. (6.3) and (6.4) are shown in Fig. 6.2. As presented in a shaded region of Fig. 6.2 from $\omega = 1.5\times10^{14}$ to 1.64×10^{14} rad/s, the real part of ε_{E} is positive, while that of ε_{O} is negative, which indicates a region with type II hyperbolic behavior. Apart from that, there is a second hyperbolic

band of type I shown in the shaded area of the inset figure from 1.82×10^{14} to 1.83×10^{14} rad/s. Note that there is a singularity point when frequency is around 1.5×10^{14} and 1.64×10^{14} rad/s, for real part of ε_O and ε_E, respectively. These behaviors are called epsilon near pole (ENP), which may cause enhanced absorption. Compared with the effective medium dielectric functions shown in Fig. 6.2, it is easy to identify that the broadband enhancement predicted by this model shown in Fig. 6.1(b) is due to the first type II hyperbolic behavior. However, for the second type I hyperbolic band from 1.82×10^{14} to 1.83×10^{14} rad/s, which is very narrow, it is hard to observe the enhancement effect from Fig. 6.1(b). Moreover, the additional two peaks around 1.5 and 1.64×10^{14} rad/s respectively shown in Fig 6.1(b) come from ENP modes of ε_O and ε_E as shown in Fig. 6.2. Although additional spectral heat flux peaks are predicted by the EMT method, the frequencies are not consistent with the ones calculated by rigorous scattering matrix theory. Therefore, the PA method under predicts the spectral heat flux between two SiC gratings, while the EMT method over predicts it. Since the two additional peaks of the spectral heat flux between two SiC gratings are consistent with the MP resonance frequencies corresponding to the far-field spectral emittance peaks of the same SiC grating geometry studied in Ref. [56], this suggests that these two spectral heat flux peaks may be due to MP excitation. For simplicity, the following discussions in this section are based on this assumption that MP is the main mechanism for these two spectral heat flux peaks. In the next section, the significant role of MP and its effect on two spectral heat flux peaks is verified.

Figure 6.3 shows the spectral radiative heat fluxes between SiC gratings at several different vacuum gap distances in near-field regime. For d = 1 μm, different from the

case of two SiC plates, the broadband peak around ω_{MP1} = 1.61×10^{14} rad/s and a small peak around ω_{MP2} = 1.75×10^{14} rad/s only occur between two SiC gratings, which could enhance the radiative heat transfer. As already discussed, these two additional peaks might be occurred due to the excitation of MP inside the groove of grating structures.

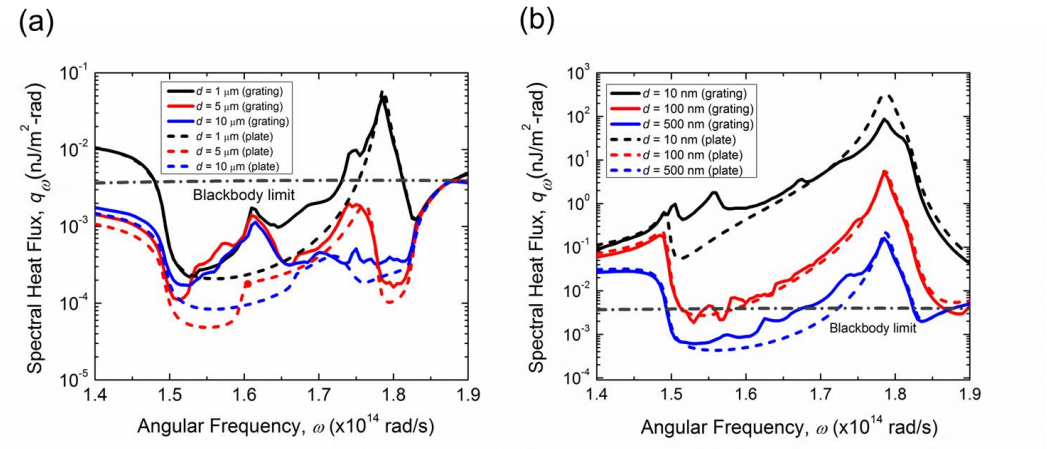

Figure 6.3 Spectral heat fluxes between two SiC gratings at (a) vacuum gap below 1 μm and (b) vacuum gap above 1 μm. The spectral heat fluxes between two SiC plates and blackbody limit are also presented. The emitter and receiver temperatures are set as 400 K and 300 K, respectively. The grating parameters are set as the default values.

When the vacuum gap increases to 5 μm, an enhanced spectral heat flux due to MP can still be observed, and the amplitude doesn't change much. However, the spectral heat flux peak due to coupled-SPhP will drop significantly because of a much weaker coupling with a larger vacuum gap. Different from the case of d = 1 μm, where coupled-SPhP dominates the total heat transfer, MP and coupled-SPhP have the equivalent effect at d = 5 μm. As the vacuum gap further increases to 10 μm, the enhanced spectral heat flux due to coupled-SPhP further decreases and that due to MP still doesn't change much, which results in that MP will dominate the total heat transfer.

On the other hand, when the vacuum gap distance becomes below 1 μm, the spectral heat fluxes between two SiC gratings and two SiC plates are shown in Fig. 6.3(b). For the case of d = 500 nm, similar to that at d = 1 μm, the enhanced spectral heat flux due to MP can still be observed, and the coupled-SPhP mode between the gratings is the same with the plates. However, when the vacuum gap further decreases to 100 nm, the effect of MP on enhancing spectral heat flux can hardly be seen, which is due to that at smaller vacuum gap the evanescent waves tunneling may dominate the heat transfer other than MP around the frequency of 1.62×10^{14} rad/s. At an extremely small vacuum gap of d = 10 nm, the low-frequency branch of coupled-SPhP will shift to a lower frequency and may have strong interaction with MP. The consequent result is that compared to the case of two SiC plates, the spectral heat flux due to coupled-SPhP will drop and MP will shift to a lower frequency to cause an enhanced spectral heat flux around 1.55×10^{14} rad/s as shown in Fig. 6.3(b). As a result, it can be understood that the MP excited inside the groove of SiC grating structures might enhance the total radiative transport at larger vacuum gap and its effect at smaller vacuum gap results in reduced heat flux.

The total radiative heat fluxes between two SiC gratings calculated by rigorous scattering theory, EMT and PA method along with the results of SiC plates are shown in Fig. 6.4. It can be noted that when the vacuum gap distance is larger than 1 μm, there is an enhancement in total heat flux of grating structures in comparison to the planar case, which is due to the excitation of MP. Although EMT method can follow the same trend with rigorous scattering theory, this is a coincidence because the total heat transfer enhancement for EMT method is mainly from hyperbolic and ENP behavior explained in

Fig. 6.2. When the vacuum gap distance is smaller than 1 μm, because of the dominating effect of coupled-SPhP and evanescent waves tunneling, the total heat flux between SiC gratings is similar to that between SiC plates.

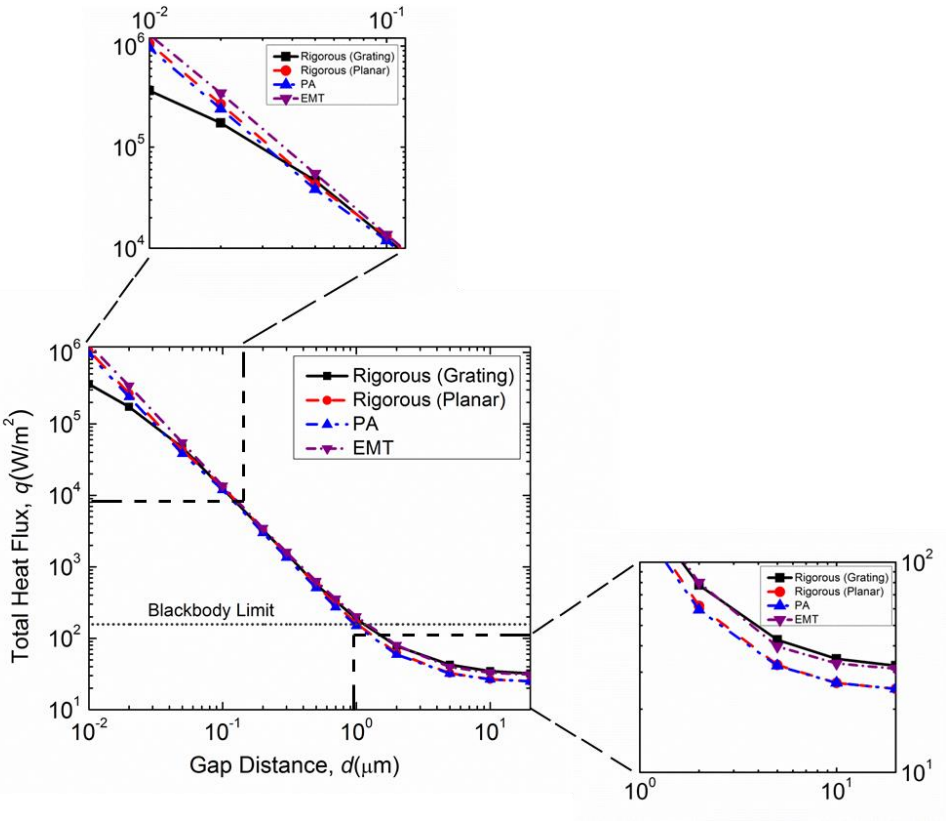

Figure 6.4 Total heat fluxes between two SiC gratings at different vacuum gaps calculated by rigorous scattering theory, EMT and PA method. The total heat fluxes between two SiC plates at different vacuum gaps are also presented. The emitter and receiver temperatures are set as 400 K and 300 K, respectively. The grating parameters are set as the default values.

However, when the vacuum gap goes below 20 nm, the total heat flux for grating is becoming less than planar SiC plates due to the interaction of MP and coupled-SPhP, which causes a significant decrease of spectral heat flux at coupled-SPhP frequency as shown in Fig. 6.3(b). Neither EMT nor PA method can predict the total heat flux decrease

below 20-nm vacuum gap. PA method is valid if the SPP/SPhP is the only mechanism to cause heat transfer enhancement, and the under-prediction of radiative heat transfer is due to that it cannot account for the contribution from MP. However, EMT provides additional hyperbolic modes, which over predicts the radiative heat transfer compared with rigorous calculation. For vacuum gap below 1 μm, the function between the total heat flux and the vacuum gap distance is fitted, and it shows that the total heat flux is proportional to d^{-2} and $d^{-1.7}$ for SiC plates and SiC gratings accordingly. Again, in this section, we assumed that additional two peaks are due to the excitation of MP. In order to verify this, the LC circuit model result of far-field SiC grating and contour plot of energy transmission coefficient along with magnetic field distribution at spectral peak frequencies will be presented as follows.

6.2 Physical Mechanisms

In order to confirm that MP resonance exists in near-field and the spectral heat flux peaks at $\omega = 1.61\times10^{14}$ rad/s and $\omega = 1.75\times10^{14}$ rad/s are due to MP resonance, the contour plots of energy transmission coefficient at $d = 1$ μm for two SiC gratings and planar surfaces are shown in Fig. 6.5(a) and (b), respectively. Note that $0 < k_{x0} < \pi/\Lambda$ and $k_y = 0$ is specified, and k_{x0} is normalized to the light line with $\omega_0 = 1.5\times10^{14}$ rad/s. The brightness in the figure indicates the strength of energy transmission across the vacuum gap in the near-field. Both the symmetric and antisymmetric branches of the dispersion curves for SPhP coupling between SiC plates are also presented as white dash lines by respectively solving the following equations[8]

$$\frac{k_{1z}}{\varepsilon_1}+\frac{k_{0z}}{\varepsilon_0}\coth\left(\frac{k_{0z}d}{2i}\right)=0 \tag{6.5a}$$

$$\frac{k_{1z}}{\varepsilon_1}+\frac{k_{0z}}{\varepsilon_0}\tanh\left(\frac{k_{0z}d}{2i}\right)=0 \tag{6.5b}$$

where the subscript "1" and "0" refers to SiC and vacuum, respectively. k_z is the wavevector component vertical to the interface. The good agreement of the coupled-SPhP dispersion curves calculated by equation (6.5) and transmission coefficient enhancement band confirms that strong horizontal enhancement band at ω_{SPhP} = 1.79×10^{14} rad/s is due to SPhP coupling between SiC plates.

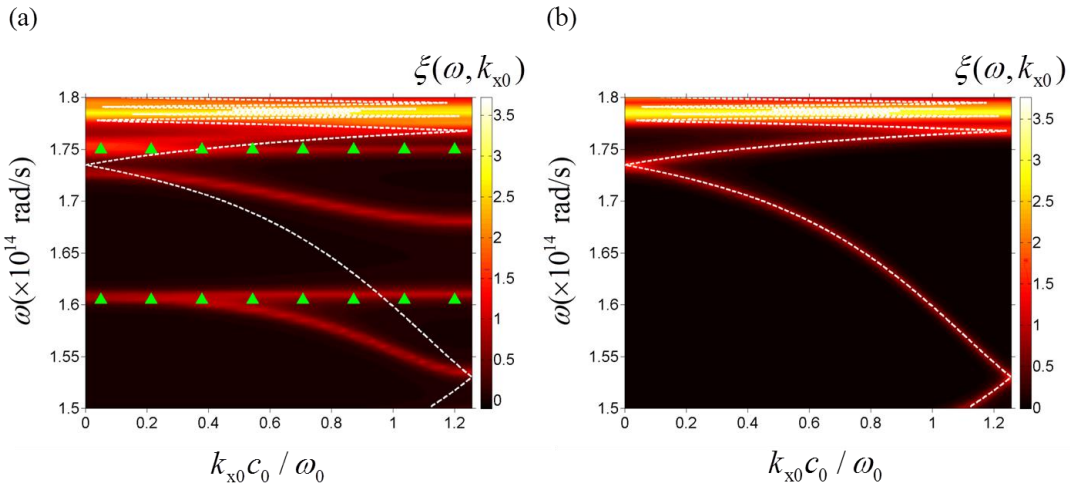

Figure 6.5 Contour plot of energy transmission coefficient (ξ) between (a) two symmetric SiC gratings at vacuum gap of 1 μm with default values and (b) two SiC plates at vacuum gap of 1 μm. Note that k_y = 0 is assumed in this plot and k_{x0} is normalized (ω_0 = 1.5×10^{14} rad/s). The dispersion relations for coupled SPhP between two SiC plates at d = 1 μm are plotted as the white dash lines and MP resonance frequencies predicted by LC circuit model are also shown with green triangles.

As shown in Fig. 6.5(a), there are two more strong horizontal enhancement bands for grating structure at ω_{MP1} = 1.61×10^{14} rad/s and ω_{MP2} = 1.75×10^{14} rad/s, which are

independent of wavevector k_{x0}. The interactions between them and coupled-SPhP have changed the behavior of coupled-SPhP modes. The independency of these two enhancement bands on wavevector k_{x0} is consistent with the characteristic of MP resonance investigated in far field regime[55,56,68].

Magnetic polaritons (MP), which indicate a strong coupling of external electromagnetic waves inside a micro/nanostructure with the magnetic resonance, have been recently employed to achieve spectral near-field heat flux enhancement. This mode can be excited when metallic slit arrays or metallic gratings are separated by a vacuum gap or a dielectric spacer. Lenz's law indicates that an oscillating current would be generated due to a time-varying magnetic field perpendicular to the plane of the structure. Coupling of magnetic resonance induced by the oscillating current flowing inside the metallic structures leads to the excitation of MP. It should be also noticed that excitation of this mode depends on the material properties and also the geometry of structure. The resonance condition of the magnetic response can be predicted by an analogy to an inductor-capacitor (LC) circuit.

For instance, the schematci of a 1D grating structure with the grating parameters of period (Λ), depth (h), and ridge width (w) is shown in Fig. 6.1(c). Based on the corresponding LC circuit model, the magnetic inductance based on the coil inductance is given by[56]

$$L_{\mathrm{m}} = \mu_0 h(\Lambda - w) \tag{6.6}$$

where μ_0 is the permeability of the vacuum. The contribution of the drifting electrons towards the inductance is also given by

$$L_{\mathrm{k}} = -(2h + (\Lambda - w)) / (\varepsilon_0 \varepsilon'_{\mathrm{m}} \omega^2 \delta) \tag{6.7}$$

where

$$\delta = \lambda / (4\pi\kappa) \tag{6.8}$$

Note that ε_0 and $\varepsilon'_{\mathrm{m}}$ are the permittivity of vacuum and the real part of the dielectric function of the grating, respectively and κ is the extinction coefficient of the grating. The gap capacitance can be also defined as

$$C = c_2 \varepsilon_0 h / (\Lambda - w) \tag{6.9}$$

here, the correction factor c_2 is a numerical factor accounting for the nonuniform charge distribution between the ridges of the grating. The far-field MP resonance frequency can be predicted using LC circuit model by zeroing the total impedance[56]

$$Z_{tot} = i\omega(L_m + L_k - \frac{1}{\omega^2 C}) = 0 \tag{6.10}$$

where L_{m}, L_{k}, C are respectively mutual inductor, kinetic inductor, and capacitor. Using Eq. (6.10), the resonance angular frequency is predicted to be $\omega_{\mathrm{LC}} = 1.61\times10^{14}$ rad/s by the LC circuit model (shown as green triangles), which matches very well with the horizontal enhancement band of transmission coefficient around ω_{MP1} from the rigorous solution. This clearly confirms the excitation of MP and its enhancement on heat transfer in near-field. By comparison between the spectral heat fluxes at d = 1 μm, it can be observed that $\omega_{\mathrm{MP2}} = 1.75\times10^{14}$ rad/s also occur at the same resonance frequency in both far and near-fields, suggesting that the spectral enhancement in near-field radiative transfer at d = 1 μm is associated with the excitation of MP.

6.3 Geometrical Effect

To further confirm and understand the behaviors of MP resonance in near-field radiative transport across vacuum gaps, the grating geometric effect on near-field radiative transfer between SiC gratings is investigated in terms of transmission coefficient at the gap distance d = 1 μm. Figures 6.6(b), (c), and (d) respectively present the effect of groove width (b), grating depth (h) and grating period (Λ) on the resonance frequency respectively in comparison to the default case shown in Fig. 6.6(a). The MP resonance frequencies predicted by the LC circuit model are also presented as green triangles in the figures, and they match very well with the horizontal enhancement bands for each case.

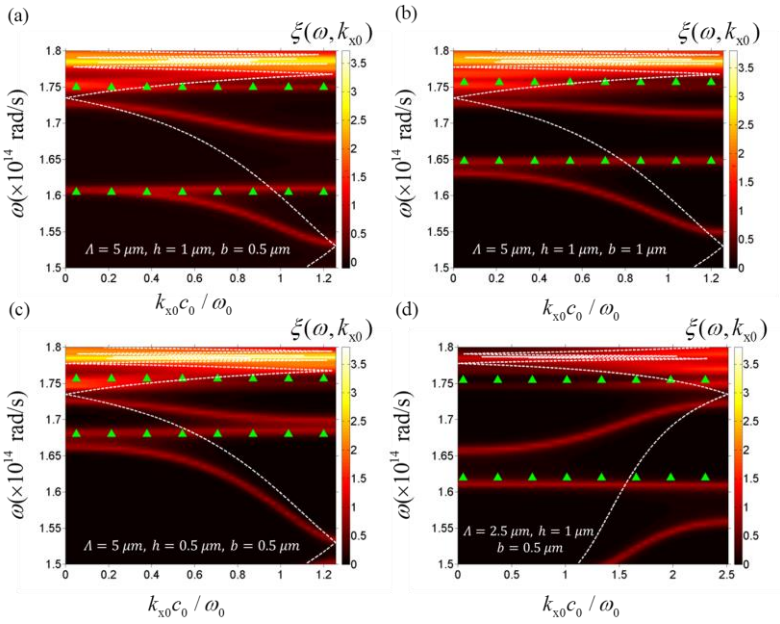

Figure 6.6 Contour plot of transmission coefficient (ξ) between two symmetric SiC gratings with different geometries of (a) Λ = 5 μm, h = 1 μm, b = 0.5 μm; (b) Λ = 5 μm, h = 1 μm, b = 1 μm; (c) Λ = 5 μm, h = 0.5 μm, b = 0.5 μm; (d) Λ = 2.5 μm, h = 1 μm, b = 0.5 μm. It should be note that vacuum gap distance are assumed as 1 μm for all cases.

When increasing the groove width from 0.5 μm to 1 μm, the MP1 resonance shifts to a higher frequency by comparing Fig. 6.6(a) and (b), which is due to the effect of the change of both inductors and capacitors. Similarly, through the comparison between Fig. 6.6(a) and (c), when grating depth decreases from 1 μm to 0.5 μm, the MP resonance will increase to a higher frequency. However, the change of grating period can hardly change the MP resonance as illustrated in Fig. 6.6(a) and (d). This is due to that the energy penetration depth in SiC is much smaller than the grating width and the grating period has little effect on any inductor or capacitor.

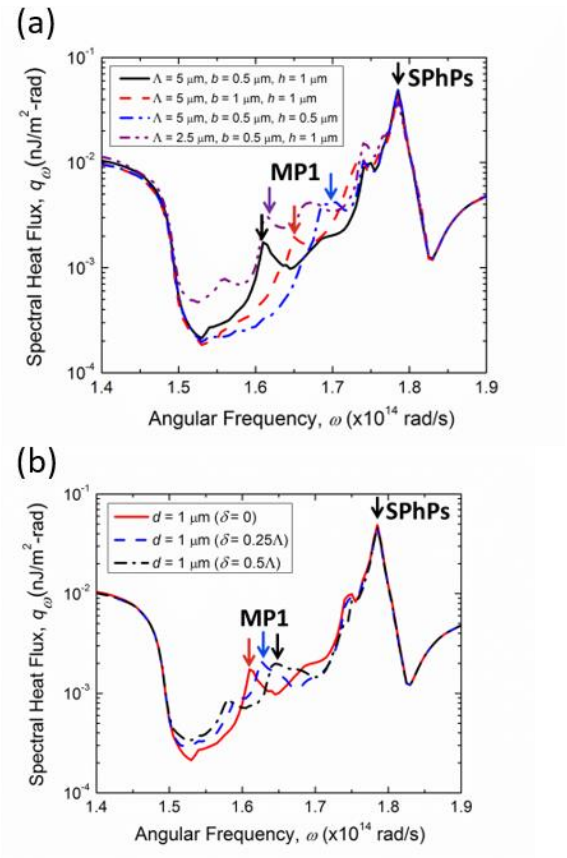

Figure 6.7(a) Spectral heat fluxes between two aligned SiC gratings at d = 1 μm for different geometries. (b) Spectral heat fluxes between two SiC gratings at d = 1 μm calculated for three different lateral displacements.

The spectral heat fluxes between two SiC gratings with different geometries are also investigated in Fig. 6.7(a). Consistent with the behavior explained in Fig. 6.6, as groove width increases or grating depth decreases, the spectral heat flux peak associated with MP1 will shift to a higher frequency, while the grating period change cannot shift the position. The MP2 resonance frequency stays to be unchanged, which is consistent with the previous observations in far field. The lateral displacement effect on spectral heat flux between two SiC gratings is also investigated. For the reference geometry with default parameters, the spectral heat fluxes for three different lateral displacements are shown in Fig. 6.7(b) with d = 1 μm.

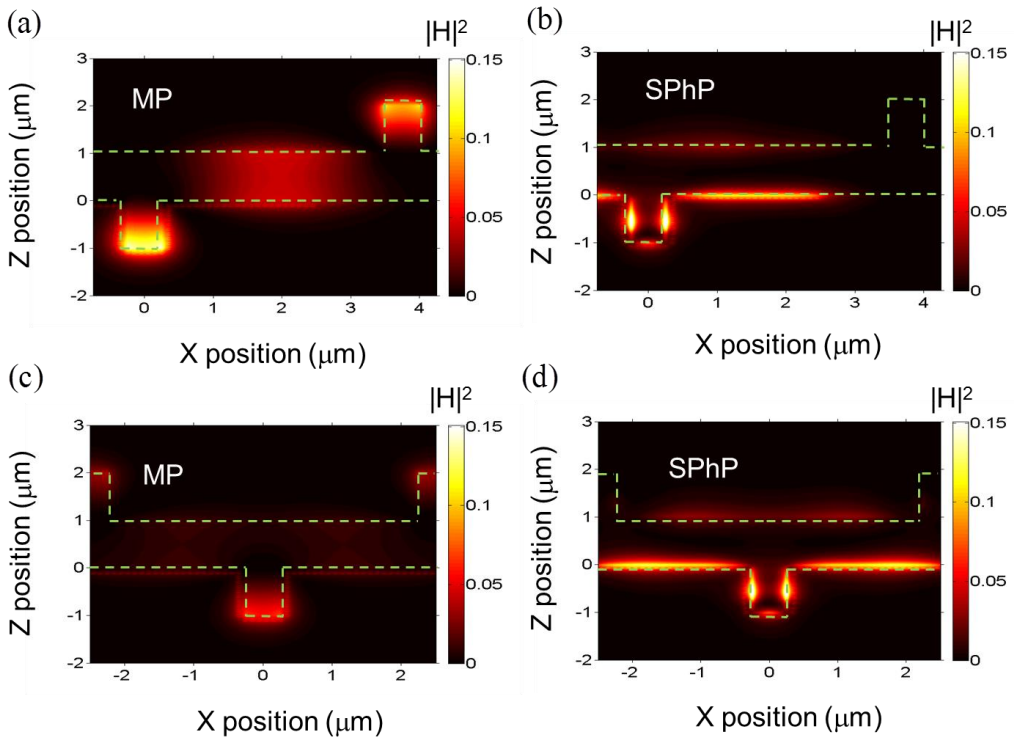

Figure 6.8 Contour plot of magnetic field between two symmetric SiC gratings at (a) magnetic polariton resonance frequency and (b) SPhP resonance frequency for $\delta = 0.25\Lambda$ and (c) magnetic polariton resonance frequency and (d) SPhP resonance frequency for $\delta = 0.5\Lambda$ when d = 1 μm and other geometric parameters are set at default values.

As lateral displacement increases from perfect alignment to half period, MP1 resonance frequency shifts to higher values while that for MP2 and coupled-SPhP frequency is not changing. The corresponding magnetic fields at MP and SPhP resonance frequencies for $\delta = 0.25\Lambda$ and $\delta = 0.5\Lambda$ are also shown in Fig. 6.8. Similar to the perfect alignment case, magnetic fields are confined within the grating groove to cause enhanced spectral heat flux at MP resonance. At coupled-SPhP resonance frequency, the surface waves just propagate along the interface between the vacuum gap and SiC grating as expected.

6.4 Near-field Thermal Radiation in Sphere-Plate Configuration

As previously stated, the total radiative heat flux can be greatly enhanced by several order of magnitudes due to the contribution of evanescent waves at nano-size vacuum gap distances. However, maintaining such a small gap distance between parallel plates and experimentally measure the thermal heat transfer emitting from a hot object to the receiver sample is a big challenge. Hence, researchers tried to develop and measure near-field radiative heat transfer between a microsphere and a planar substrate to validate the theoretical predictions. Here, a brief explanation for the numerical methodology is given while the experimental demonstration of near-field radiation between a microsphere and a metamaterial substrate can be defined as a future project as it is discussed in Chapter 7. For a sphere-plate configuration, the near-field radiative heat flux can be estimated by proximity force theorem as[10]

$$G(d) \approx 2\pi R \int_{s=d}^{\infty} h_{\text{near-field}}^{\text{Plate-Plate}}(s)ds \tag{6.11}$$

where G is the near-field conductance, $h(s)$ represents the near-field radiative heat transfer coefficient between two planar surfaces separated by a vacuum gap distance of s, R is the radius of the sphere, and d is the vacuum gap distance between the sphere and substrate. The radius of microsphere in the following obtained numerical results is assumed as 50 μm and hence, the upper limit for the integration in equation 6.11 is also set as 50 μm. It should be noted that there is no rigorous theoretical calculation for the near-field radiation in a sphere-plate configuration due to the large computational effort[10].

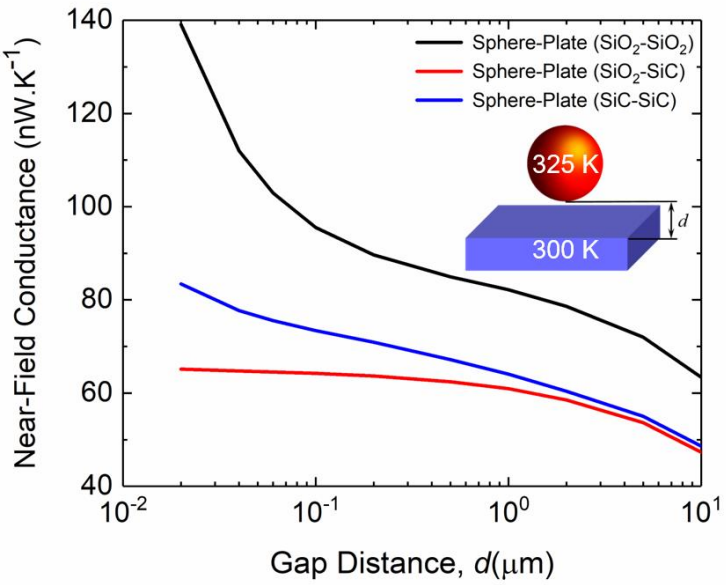

Figure 6.9 Theoretical near-field conductance obtained by the proximity force theorem for different material combinations (SiO_2-SiO_2, SiO_2-SiC, and SiC-SiC). The emitter and receiver temperatures are 325 K and 300 K, respectively.

Fig. 6.9 represents the near-field conductance (G) between a microsphere with diameter of 100 μm and a planar surface as a function of vacuum gap distance for different material combinations. The emitter and receiver temperature are considered as

325 K and 300 K, respectively. As previously stated, the contribution of evanescent modes can greatly enhance the near-field radiative heat transfer. As depicted in Fig 6.9, near-field conductance for all combinations (SiO_2-SiO_2, SiO_2-SiC, and SiC-SiC) is significantly enhanced at smaller vacuum gap distances due to the contribution of evanescent modes. However, in a sphere-plate geometry both made of SiO_2, the near-field conductance shown by solid black line is much increased at smaller vacuum gap distances comparing to the cases of SiO_2-SiC, and SiC-SiC. It should be noticed that resonance surface waves can even contribute more to near-field radiation comparing to non-resonant evanescent waves. It is well-known that polar dielectric materials such as SiO_2 can support surface phonon polaritons at or near to room temperature. Thus, the dominant contribution from the excitation of surface phonon polaritons plays a significant role in smaller vacuum gap distances for the case of SiO_2-SiO_2. On the other hand, mismatch of material properties between SiC and SiO_2 cannot support coupling resonance modes and results in a smaller enhancement as indicated by red solid line in Fig 6.9.

CHAPTER 7

CONCLUSION AND FUTURE RECOMMENDATIONS

This chapter provides an overall conclusion of each research task performed for this dissertation in Section 7.1. The future experimental research on plate-plate near-field TPV systems and near-field radiation in a sphere-plate configuration are recommended in Sections 7.2 and 7.3, respectively.

7.1 Conclusion

This dissertation experimentally demonstrated the near-field and thin-film effects along with the excitation of resonance modes on enhanced radiative heat transfer. Ultra-thin aluminum layers coated on 5×5 mm^2 silicon parallel plates are separated by nanosized polystyrene particles. The near-field radiative heat flux between 13-nm-thick Al films is measured at a vacuum gap distance of 215 nm, showing an improvement of 6.4 times over the blackbody limit and 420 times over that of the far-field radiative heat transfer between bulk Al plates with a temperature difference of 65 K. The reasonable agreement between the experimental results and theoretical prediction from fluctuational electrodynamics suggests the contribution of increased scattering and SPP coupling inside the Al thin-film layers to the near-field energy transfer.

In addition, we theoretically investigated the effects of different physical mechanisms such as SPhP/SPP, MPs, and HM on near-field radiative transfer and employed them to spectrally enhance and tune the spectral radiative heat flux in near-field TPV systems. First, a multilayered emitter separated from $In_{0.18}Ga_{0.82}Sb$ cell is considered in which the tungsten and alumina layer thicknesses are optimized to obtain

maximum electrical power output. It is shown that the spectral heat flux is much enhanced when plain tungsten emitter is replaced with the multilayer emitter due to effective medium intrinsic lossy property and additional surface plasmon polariton coupling in the tungsten thin film. The invalidity of effective medium theory to predict photon transport in the near-field with multilayer emitters is also discussed. Second, the performance of a near-field thermophotovoltaic (TPV) system including an emitter (GZO) at temperature of 1800 K and a tandem cell composed of p-doped GaSb and n-doped InAs PV cells at 300 K supported by a gold back reflector is numerically investigated. Fluctuational electrodynamics along with the dyadic Green's function is applied to evaluate the net radiative heat transfer and electrical power output. The thicknesses of PV cells are optimized to obtain the maximum efficiency while Auger recombination is considered in the evaluation of the current density. Here, we demonstrated that using a tandem cell in a near-field thermophotovoltaic system can achieve an increased conversion efficiency and electrical power output of 39.1% and 244.4 kW/m^2, respectively at a vacuum gap distance of 100 nm. The thickness of p-doped GaSb and n-doped InAs sub-cells are considered as 1.5 μm, and 0.5 μm, respectively. It shows an improvement of 4.6% compared to a 2 μm-single GaSb cell and an improvement of 10.8% compared to a 2 μm-single InAs cell. This enhancement is due to the enhanced spectral selectivity in each layer of PV cells where photons with higher energy would be absorbed by the first layer (GaSb) while the ones with lower energy are absorbed in the second cell (InAs). Third, the performance of a near-field TPV system containing a Drude grating emitter, an ultra-thin $In_{0.18}Ga_{0.82}Sb$ cell with a metal back reflector beneath the PV cell is investigated. The radiative heat transfer is modeled by

using scattering matrix theory, and the electrical power output is obtained by assuming an internal quantum efficiency of 100%. The thickness of the PV cell is optimized to be t = 100 nm in terms of conversion efficiency. It is found that, power output and conversion efficiency are enhanced to 115.9 W/m^2 and 19.2% respectively with grating emitter at the vacuum gap of d = 50 nm, while those for the planar emitter are 49.1 W/m^2 and 15.3%. Excitation of magnetic polaritons (MP) across the vacuum gap and inside the $In_{0.18}Ga_{0.82}Sb$ cell right above the bandgap energy of the cell is demonstrated as the main mechanism for the efficiency enhancement of the near-field TPV system with grating emitter compared with planar emitter.

Finally, we have theoretically investigated the effect of magnetic polaritons excited inside the deep grooves of SiC grating microstructures on near-field radiative transfer. It shows that at larger vacuum gap distance, compared to the case of SiC plates, SiC gratings have a higher total heat flux due to MP excitation. However, when it comes to smaller vacuum gap distance, MP can hardly improve the total heat flux due to the dominating coupled-SPhP effect and even suppress it after interaction with coupled-SPhP at extremely small vacuum gap. The EMT and PA methods are also analyzed and neither of them can predict the heat transfer correctly. The contour plots of transmission coefficient and magnetic field distribution have been employed to identify the MP effect as well. This study demonstrated that the excitation of magnetic polaritons can be an effective way to spectrally control the near-field thermal radiation which is particularly beneficial for energy-harvesting applications.

7.2 Recommendation on Plate-Plate NF-TPV Experiment with Multilayers

This dissertation mainly focused on designing an efficient near-field thermophotovoltaic system by help of MP and SPPs/SPhPs excited in metamaterial nanostructures. Using tandem cell in near-field TPV devices is also found as an effective approach providing an optimized utilization of the energy of photons and enhancing the electric current and consequently the conversion efficiency. However, all the works proposed in this dissertation are based on theoretical calculations. Hence, the future recommendation is to prepare an experimental setup for the study of near-field radiative heat transfer role and the impact of resonance modes such as MP and SPPs/SPhPs in energy conversion systems. The experimental project will mainly include designing an optimized multilayered emitter, sample fabrication, and material property characterization. The effect of near-field and resonance modes on photogeneration current, and the spectrum of the radiative transfer should be also analyzed. In addition, the effect of a back reflector on output power density can be experimentally demonstrated.

7.3 Recommendation on Sphere-Plate SiC Metasurface Experiment to Verify MP

The main challenge of near-field radiation measurement is to maintain a small vacuum gap distance (usually below 200 nm) between two plates. By proposing a sphere-plate configuration, the obstacle of maintaining parallel surfaces can be removed. In addition, a smaller vacuum gap distance typically below 100 nm can be achieved. It should be noted that the near-field radiative heat transfer measurement between a sphere and a plate requires Scanning Electrochemical Microscopy (SECM) or Atomic Force

Microscope (AFM) probe fabrication. In the next step, a sphere with a diameter of 50 μm or 100 μm made of SiC attaching to a probe should be placed with a distance greater than 2 μm above a planar SiC grating structure. Then, the sphere should be approaching to the substrate step by step to finally reach the surface. It should be noted that as soon as the contact is made, the temperature of the tip reduces rapidly. Finally, probe should leave the surface to create a nano-vacuum gap distance between the sphere and the substrate. However, the resolution of the system and the surface roughness are two challenges in determining a precise vacuum gap distance. A correct estimation for the tip temperature using thermal conductivity model and the deflection of the cantilever would be other difficulties. The obtained experimental results of this work can verify the significant role of MP in enhanced near-field thermal radiation between SiC nanostructures in the near-field regime that can follow up the theoretical results presented in Chapter 6 of this dissertation.

REFERENCES

1 Chen, Y. B. & Zhang, Z. M. Design of tungsten complex gratings for thermophotovoltaic radiators. *Optics Communications* **269**, 411-417 (2007).

2 Zhao, B., Wang, L. P., Shuai, Y. & Zhang, Z. M. M. Thermophotovoltaic emitters based on a two-dimensional grating/thin-film nanostructure. *International Journal of Heat and Mass Transfer* **67**, 637-645 (2013).

3 Wang, L. P. & Zhang, Z. M. Wavelength-selective and diffuse emitter enhanced by magnetic polaritons for thermophotovoltaics. *Applied Physics Letters* **100**, 063902 (2012).

4 Sai, H., Kanamori, Y. & Yugami, H. High-temperature resistive surface grating for spectral control of thermal radiation. *Applied Physics Letters* **82**, 1685-1687 (2003).

5 Narayanaswamy, A. & Chen, G. Thermal emission control with one-dimensional metallodielectric photonic crystals. *Physical Review B* **70**, 125101 (2004).

6 Karalis, A. & Joannopoulos, J. D. 'Squeezing' near-field thermal emission for ultra-efficient high-power thermophotovoltaic conversion. *Scientific Reports* **6**, 28472 (2016).

7 Basu, S. & Wang, L. P. Near-field radiative heat transfer between doped silicon nanowire arrays. *Applied Physics Letters* **102**, 053101 (2013).

8 Basu, S., Zhang, Z. M. & Fu, C. J. Review of near-field thermal radiation and its application to energy conversion. *International Journal of Energy Research* **33**, 1203-1232 (2009).

9 Shen, S., Mavrokefalos, A., Sambegoro, P. & Chen, G. Nanoscale thermal radiation between two gold surfaces. *Applied Physics Letters* **100**, 233114 (2012).

10 Shen, S., Narayanaswamy, A. & Chen, G. Surface Phonon Polaritons Mediated Energy Transfer between Nanoscale Gaps. *Nano Letters* **9**, 2909-2913 (2009).

11 Narayanaswamy, A., Shen, S. & Chen, G. Near-field radiative heat transfer between a sphere and a substrate. *Physical Review B* **78**, 115303 (2008).

12 Zhang, Z. M. *Nano/microscale heat transfer*. (McGraw-Hill, 2007).

13 Hu, L., Narayanaswamy, A., Chen, X. Y. & Chen, G. Near-field thermal radiation between two closely spaced glass plates exceeding Planck's blackbody radiation law. *Applied Physics Letters* **92**, 133106 (2008).

14 Lim, M., Song, J., Lee, S. S. & Lee, B. J. Tailoring near-field thermal radiation between metallo-dielectric multilayers using coupled surface plasmon polaritons. *Nature Communications* **9**, 4302 (2018).

15 Ghashami, M. *et al.* Precision Measurement of Phonon-Polaritonic Near-Field Energy Transfer between Macroscale Planar Structures Under Large Thermal Gradients. *Physical Review Letters* **120**, 175901 (2018).

16 Silveirinha, M. & Engheta, N. Tunneling of electromagnetic energy through subwavelength channels and bends using ε-near-zero materials. *Physical Review Letters* **97**, 157403 (2006).

17 Alù, A., Silveirinha, M. G., Salandrino, A. & Engheta, N. Epsilon-near-zero metamaterials and electromagnetic sources: Tailoring the radiation phase pattern. *Physical Review B* **75**, 155410 (2007).

18 Molesky, S., Dewalt, C. J. & Jacob, Z. High temperature epsilon-near-zero and epsilon-near-pole metamaterial emitters for thermophotovoltaics. *Optics Express* **21 Suppl 1**, A96-110 (2013).

19 Chang, J. Y., Yang, Y. & Wang, L. P. Tungsten nanowire based hyperbolic metamaterial emitters for near-field thermophotovoltaic applications. *International Journal of Heat and Mass Transfer* **87**, 237-247 (2015).

20 Biehs, S. A., Tschikin, M. & Ben-Abdallah, P. Hyperbolic Metamaterials as an Analog of a Blackbody in the Near Field. *Physical Review Letters* **109**, 104301 (2012).

21 Cortes, C. L., Newman, W., Molesky, S. & Jacob, Z. Quantum nanophotonics using hyperbolic metamaterials. *Journal of Optics* **14**, 063001 (2012).

22 Guo, Y., Newman, W., Cortes, C. L. & Jacob, Z. Applications of hyperbolic metamaterial substrates. *Advances in OptoElectronics* **2012** (2012).

23 Guo, Y., Cortes, C. L., Molesky, S. & Jacob, Z. Broadband super-Planckian thermal emission from hyperbolic metamaterials. *Applied Physics Letters* **101**, 131106 (2012).

24 Liu, B. A., Shi, J. W., Liew, K. & Shen, S. Near-field radiative heat transfer for Si based metamaterials. *Optics Communications* **314**, 57-65 (2014).

25 Liu, X. L., Zhang, R. Z. & Zhang, Z. M. Near-field thermal radiation between hyperbolic metamaterials: Graphite and carbon nanotubes. *Applied Physics Letters* **103**, 213102 (2013).

26 Liu, B. A. & Shen, S. Broadband near-field radiative thermal emitter/absorber based on hyperbolic metamaterials: Direct numerical simulation by the Wiener chaos expansion method. *Physical Review B* **87**, 115403 (2013).

27 Biehs, S. A., Ben-Abdallah, P., Rosa, F. S. S., Joulain, K. & Greffet, J. J. Nanoscale heat flux between nanoporous materials. *Optics Express* **19**, A1088-A1103 (2011).

28 Basu, S., Chen, Y. B. & Zhang, Z. M. Microscale radiation in thermophotovoltaic devices - A review. *International Journal of Energy Research* **31**, 689-716 (2007).

29 Yang, Y., Chang, J. Y., Sabbaghi, P. & Wang, L. P. Performance Analysis of a Near-Field Thermophotovoltaic Device With a Metallodielectric Selective Emitter and Electrical Contacts for the Photovoltaic Cell. *Journal of Heat Transfer-Transactions of the Asme* **139**, 052701 (2017).

30 Tong, J. K., Hsu, W. C., Huang, Y., Boriskina, S. V. & Chen, G. Thin-film 'Thermal Well' Emitters and Absorbers for High-Efficiency Thermophotovoltaics. *Scientific Reports* **5** (2015).

31 Park, K., Basu, S., King, W. P. & Zhang, Z. M. Performance analysis of near-field thermophotovoltaic devices considering absorption distribution, *Journal of Quantitative Spectroscopy & Radiative Transfer* **109**, 305 (2008).

32 Yu, H. T., Liu, D., Duan, Y. Y. & Yang, Z. Four-layer metallodielectric emitter for spectrally selective near-field radiative transfer in nano-gap thermophotovoltaics. *Journal of Quantitative Spectroscopy & Radiative Transfer* **217**, 235-242 (2018).

33 Daneshvar, H., Prinja, R. & Kherani, N. P. Thermophotovoltaics: Fundamentals, challenges and prospects. *Applied Energy* **159**, 560-575 (2015).

34 Ilic, O., Jablan, M., Joannopoulos, J. D., Celanovic, I. & Soljacic, M. Overcoming the black body limit in plasmonic and graphene near-field thermophotovoltaic systems. *Optics Express* **20**, A366-384 (2012).

35 DeSutter, J., Bernardi, M. P. & Francoeur, M. Determination of thermal emission spectra maximizing thermophotovoltaic performance using a genetic algorithm. *Energy Conversion and Management* **108**, 429-438 (2016).

36 Otey, C. R., Lau, W. T. & Fan, S. H. Thermal Rectification through Vacuum. *Physical Review Letters* **104**, 154301 (2010).

37 Iizuka, H. & Fan, S. H. Rectification of evanescent heat transfer between dielectric-coated and uncoated silicon carbide plates. *Journal of Applied Physics* **112**, 024304 (2012).

38 Yang, Y., Basu, S. & Wang, L. P. Radiation-based near-field thermal rectification with phase transition materials. *Applied Physics Letters* **103**, 163101 (2013).

39 Liu, X. L. & Zhang, Z. M. M. High-performance electroluminescent refrigeration enabled by photon tunneling. *Nano Energy* **26**, 353-359 (2016).

40 Chen, K. F., Santhanam, P., Sandhu, S., Zhu, L. X. & Fan, S. H. Heat-flux control and solid-state cooling by regulating chemical potential of photons in near-field electromagnetic heat transfer. *Physical Review B* **91**, 134301 (2015).

41 Park, K. & Zhang, Z. Fundamentals and applications of near-field radiative energy transfer. *Frontiers in Heat and Mass Transfer (FHMT)* **4** (2013).

42 Rousseau, E. *et al.* Radiative heat transfer at the nanoscale. *Nature Photonics* **3**, 514-517 (2009).

43 Thompson, D. *et al.* Hundred-fold enhancement in far-field radiative heat transfer over the blackbody limit. *Nature* **561**, 216-221 (2018).

44 Fiorino, A. *et al.* Giant Enhancement in Radiative Heat Transfer in Sub-30 nm Gaps of Plane Parallel Surfaces. *Nano Letters* **18**, 3711-3715 (2018).

45 Liu, X. L., Wang, L. P. & Zhang, Z. M. M. Near-Field Thermal Radiation: Recent Progress and Outlook. *Nanoscale and Microscale Thermophysical Engineering* **19**, 98-126 (2015).

46 Joulain, K., Mulet, J. P., Marquier, F., Carminati, R. & Greffet, J. J. Surface electromagnetic waves thermally excited: Radiative heat transfer, coherence properties and Casimir forces revisited in the near field. *Surface Science Reports* **57**, 59-112 (2005).

47 Jones, A. C., O'Callahan, B. T., Yang, H. U. & Raschke, M. B. The thermal near-field: Coherence, spectroscopy, heat-transfer, and optical forces. *Progress in Surface Science* **88**, 349-392 (2013).

48 Doherty, M. D., Murphy, A., Pollard, R. J. & Dawson, P. Surface-Enhanced Raman Scattering from Metallic Nanostructures: Bridging the Gap between the Near-Field and Far-Field Responses. *Physical Review X* **3**, 011001 (2013).

49 Dai, J., Ding, F., Bozhevolnyi, S. I. & Yan, M. Ultrabroadband super-Planckian radiative heat transfer with artificial continuum cavity states in patterned hyperbolic metamaterials. *Physical Review B* **95**, 245405 (2017).

50 Wang, B. N., Lin, C. W., Teo, K. H. & Zhang, Z. M. Thermoradiative device enhanced by near-field coupled structures. *Journal of Quantitative Spectroscopy & Radiative Transfer* **196**, 10-16 (2017).

51 Yang, Y. & Wang, L. P. Spectrally Enhancing Near-Field Radiative Transfer between Metallic Gratings by Exciting Magnetic Polaritons in Nanometric Vacuum Gaps. *Physical Review Letters* **117**, 044301 (2016).

52 Yang, Y., Sabbaghi, P. & Wang, L. P. Effect of magnetic polaritons in SiC deep gratings on near-field radiative transfer. *International Journal of Heat and Mass Transfer* **108**, 851-859 (2017).

53 Lee, B. J., Wang, L. P. & Zhang, Z. M. Coherent thermal emission by excitation of magnetic polaritons between periodic strips and a metallic film. *Optics Express* **16**, 11328-11336 (2008).

54 Wang, L. P. & Zhang, Z. M. Effect of magnetic polaritons on the radiative properties of double-layer nanoslit arrays. *Journal of the Optical Society of America B-Optical Physics* **27**, 2595-2604 (2010).

55 Wang, L. & Zhang, Z. Resonance transmission or absorption in deep gratings explained by magnetic polaritons. *Applied Physics Letters* **95**, 111904 (2009).

56 Wang, L. P. & Zhang, Z. M. Phonon-mediated magnetic polaritons in the infrared region. *Optics Express* **19**, A126-A135 (2011).

57 Song, B. *et al.* Radiative heat conductances between dielectric and metallic parallel plates with nanoscale gaps. *Nature Nanotechnology* **11**, 509 (2016).

58 Kim, K. *et al.* Radiative heat transfer in the extreme near field. *Nature* **528**, 387-391 (2015).

59 Ito, K., Miura, A., Iizuka, H. & Toshiyoshi, H. Parallel-plate submicron gap formed by micromachined low-density pillars for near-field radiative heat transfer. *Applied Physics Letters* **106**, 083504 (2015).

60 St-Gelais, R., Zhu, L. X., Fan, S. H. & Lipson, M. Near-field radiative heat transfer between parallel structures in the deep subwavelength regime. *Nature Nanotechnology* **11**, 515 (2016).

61 Shi, J. W., Li, P. F., Liu, B. A. & Shen, S. Tuning near field radiation by doped silicon. *Applied Physics Letters* **102**, 183114 (2013).

62 Lim, M., Lee, S. S. & Lee, B. J. Near-field thermal radiation between doped silicon plates at nanoscale gaps. *Physical Review B* **91**, 195136 (2015).

63 Watjen, J. I., Zhao, B. & Zhang, Z. M. M. Near-field radiative heat transfer between doped-Si parallel plates separated by a spacing down to 200 nm. *Applied Physics Letters* **109**, 203112 (2016).

64 Bernardi, M. P., Milovich, D. & Francoeur, M. Radiative heat transfer exceeding the blackbody limit between macroscale planar surfaces separated by a nanosize vacuum gap. *Nature Communications* **7**, 12900 (2016).

65 Kralik, T. *et al.* Strong Near-Field Enhancement of Radiative Heat Transfer between Metallic Surfaces. *Physical Review Letters* **109**, 224302 (2012).

66 Boriskina, S. *et al.* Enhancement and tunability of near-field radiative heat transfer mediated by surface plasmon polaritons in thin plasmonic films. *Photonics* **2**, 659-683 (2015).

67 Zhao, B. & Zhang, Z. M. Study of magnetic polaritons in deep gratings for thermal emission control. *Journal of Quantitative Spectroscopy and Radiative Transfer* **135**, 81-89 (2014).

68 Wang, H. & Wang, L. Perfect selective metamaterial solar absorbers. *Optics Express* **21 Suppl 6**, A1078-1093 (2013).

69 Wang, H., Yang, Y. & Wang, L. Switchable wavelength-selective and diffuse metamaterial absorber/emitter with a phase transition spacer layer. *Applied Physics Letters* **105**, 071907 (2014).

70 Wang, H., Yang, Y. & Wang, L. Infrared frequency-tunable coherent thermal sources. *Journal of Optics* **17**, 045104 (2015).

71 Dai, J., Dyakov, S. & Yan, M. Radiative heat transfer between two dielectric-filled metal gratings. *Physical Review B* **93**, 155403 (2016).

72 Dai, J., Dyakov, S. A. & Yan, M. Enhanced near-field radiative heat transfer between corrugated metal plates: Role of spoof surface plasmon polaritons. *Physical Review B* **92**, 035419 (2015).

73 Sabbaghi, P., Yang, Y., Chang, J.-Y. & Wang, L. Near-Field Thermophotovoltaic Energy Conversion by Excitation of Magnetic Polariton inside Nanometric Vacuum Gaps with Nanostructured Drude Emitter and Backside Reflector. *Journal of Quantitative Spectroscopy and Radiative Transfer* **234**, 108-114 (2019).

74 Chubb, D. L. & Lowe, R. A. Thin-film selective emitter. *Journal of Applied Physics* **74**, 5687-5698 (1993).

75 Chubb, D. L. & Wolford, D. S. Dual layer selective emitter. *Applied Physics Letters* **87**, 141907 (2005).

76 Lin, S.-Y., Moreno, J. & Fleming, J. Three-dimensional photonic-crystal emitter for thermal photovoltaic power generation. *Applied Physics Letters* **83**, 380-382 (2003).

77 Sai, H., Kanamori, Y. & Yugami, H. Tuning of the thermal radiation spectrum in the near-infrared region by metallic surface microstructures. *Journal of Micromechanics and Microengineering* **15**, S243 (2005).

78 Fiorino, A. *et al.* Nanogap near-field thermophotovoltaics. *Nature Nanotechnology* **13**, 806-811 (2018).

79 Yeng, Y. X. *et al.* Performance analysis of experimentally viable photonic crystal enhanced thermophotovoltaic systems. *Optics Express* **21 Suppl 6**, A1035-1051 (2013).

80 Yeng, Y. X. *et al.* Photonic crystal enhanced silicon cell based thermophotovoltaic systems. *Optics Express* **23**, A157-168 (2015).

81 Zhou, Z. G., Chen, Q. S. & Bermel, P. Prospects for high-performance thermophotovoltaic conversion efficiencies exceeding the Shockley-Queisser limit. *Energy Conversion and Management* **97**, 63-69 (2015).

82 Whale, M. D. & Cravalho, E. G. Modeling and performance of microscale thermophotovoltaic energy conversion devices. *Ieee Transactions on Energy Conversion* **17**, 130-142 (2002).

83 Whale, M. D. *A fluctuational electrodynamic analysis of microscale radiative transfer and the design of microscale thermophotovoltaic devices*, Massachusetts Institute of Technology (1997).

84 Laroche, M., Carminati, R. & Greffet, J.-J. Near-field thermophotovoltaic energy conversion. *Journal of Applied Physics* **100**, 063704 (2006).

85 Park, K., Basu, S., King, W. P. & Zhang, Z. M. Performance analysis of near-field thermophotovoltaic devices considering absorption distribution. *Journal of Quantitative Spectroscopy & Radiative Transfer* **109**, 305-316 (2008).

86 Francoeur, M., Vaillon, R. & Mengüç, M. P. Thermal impacts on the performance of nanoscale-gap thermophotovoltaic power generators. *IEEE Transactions on Energy Conversion* **26**, 686-698 (2011).

87 Bright, T. J., Wang, L. P. & Zhang, Z. M. Performance of Near-Field Thermophotovoltaic Cells Enhanced With a Backside Reflector. *Journal of Heat Transfer-Transactions of the Asme* **136**, 062701 (2014).

88 Jin, S., Lim, M., Lee, S. S. & Lee, B. J. Hyperbolic metamaterial-based near-field thermophotovoltaic system for hundreds of nanometer vacuum gap. *Optics Express* **24**, A635-649 (2016).

89 Messina, R. & Ben-Abdallah, P. Graphene-based photovoltaic cells for near-field thermal energy conversion. *Scientific Reports* **3**, 1383 (2013).

90 Bernardi, M. P. *et al.* Impacts of propagating, frustrated and surface modes on radiative, electrical and thermal losses in nanoscale-gap thermophotovoltaic power generators. *Scientific Reports* **5**, 11626 (2015).

91 Narayanaswamy, A. & Chen, G. Surface modes for near field thermophotovoltaics. *Applied Physics Letters* **82**, 3544-3546 (2003).

92 Watjen, J., Liu, X., Zhao, B. & Zhang, Z. in *ASME 2016 5th International Conference on Micro/Nanoscale Heat and Mass Transfer*. V001T005A011-V001T005A011 (American Society of Mechanical Engineers).

93 Yu, H. T., Duan, Y. Y. & Yang, Z. Selectively enhanced near-field radiative transfer between plasmonic emitter and GaSb with nanohole and nanowire periodic arrays for thermophotovoltaics. *International Journal of Heat and Mass Transfer* **123**, 67-74 (2018).

94 Yu, H. T., Liu, D., Yang, Z. & Duan, Y. Y. Simple Rectangular Gratings as a Near-Field "Anti-Reflection" Pattern for GaSb TPV Cells. *Scientific Reports* **7**, 1026 (2017).

95 Anaya, M., Lozano, G., Calvo, M. E. & Míguez, H. ABX3 perovskites for tandem solar cells. *Joule* **1**, 769-793 (2017).

96 Eperon, G. E., Hörantner, M. T. & Snaith, H. J. Metal halide perovskite tandem and multiple-junction photovoltaics. *Nature Reviews Chemistry* **1**, 0095 (2017).

97 McMeekin, D. P. *et al.* Solution-Processed All-Perovskite Multi-Junction Solar Cells. *Joule* **3**, 387-401 (2019).

98 Zhao, D. *et al.* Efficient two-terminal all-perovskite tandem solar cells enabled by high-quality low-bandgap absorber layers. *Nature Energy* **3**, 1093 (2018).

99 Wilt, D., Wehrer, R., Palmisiano, M., Wanlass, M. & Murray, C. Monolithic interconnected modules (MIMs) for thermophotovoltaic energy conversion. *Semiconductor Science and Technology* **18**, S209 (2003).

100 Sahoo, G. & Mishra, G. Efficient use of low-Bandgap GaAs/GaSb to convert more than 50% of solar radiation into electrical energy: a numerical approach. *Journal of Electronic Materials* **48**, 560-570 (2019).

101 Goodson III, T. *Solar Fuels: Materials, Physics, and Applications*. (CRC Press, 2017).

102 Palik, E. D. *Handbook of optical constants of solids*. Vol. 3 (Academic press, 1998).

103 Modest, M. F. *Radiative heat transfer*. (Academic press, 2013).

104 Basu, S. & Zhang, Z. M. Maximum energy transfer in near-field thermal radiation at nanometer distances. *Journal of Applied Physics* **105**, 093535 (2009).

105 Fu, C. J. & Zhang, Z. M. Nanoscale radiation heat transfer for silicon at different doping levels. *International Journal of Heat and Mass Transfer* **49**, 1703-1718 (2006).

106 Hertz, H. On the contact of elastic solids. *Z. Reine Angew. Mathematik* **92**, 156-171 (1881).

107 Guo, D., Li, J., Xie, G., Wang, Y. & Luo, J. Elastic properties of polystyrene nanospheres evaluated with atomic force microscopy: size effect and error analysis. *Langmuir* **30**, 7206-7212 (2014).

108 Dolbow, J. & Gosz, M. Effect of out-of-plane properties of a polyimide film on the stress fields in microelectronic structures. *Mechanics of Materials* **23**, 311-321 (1996).

109 Rytov, S. M. *Principles of Statistical Radiophysics*. (Springer-Verlag, 1987).

110 Francoeur, M., Menguc, M. P. & Vaillon, R. Solution of near-field thermal radiation in one-dimensional layered media using dyadic Green's functions and the scattering matrix method. *Journal of Quantitative Spectroscopy & Radiative Transfer* **110**, 2002-2018 (2009).

111 Henry, C. H. & Kazarinov, R. F. Quantum noise in photonics. *Reviews of Modern Physics* **68**, 801 (1996).

112 Blandre, E. *Thermal radiation at the nanoscale: near-field and interference effects in few-layer structures and on the electrical performances of thermophotovoltaic devices*, Tohoku University (2016).

113 Ashcroft, N. W. & Mermin, N. D. *Solid state physics*. (saunders college, philadelphia, 1976).

114 Zhao, B. *et al.* High-performance near-field thermophotovoltaics for waste heat recovery. *Nano Energy* **41**, 344-350 (2017).

115 Kim, J., Naik, G. V., Emani, N. K., Guler, U. & Boltasseva, A. Plasmonic resonances in nanostructured transparent conducting oxide films. *IEEE Journal of Selected Topics in Quantum Electronics* **19**, 4601907-4601907 (2013).

116 Lambrecht, A. & Marachevsky, V. N. Casimir interaction of dielectric gratings. *Physical Review Letters* **101**, 160403 (2008).

117 Liu, X. L. & Zhang, Z. M. Graphene-assisted near-field radiative heat transfer between corrugated polar materials. *Applied Physics Letters* **104**, 251911 (2014).

118 Lussange, J. *et al.* Radiative heat transfer between two dielectric nanogratings in the scattering approach. *Physical Review B* **86**, 085432 (2012).

119 Li, L. F. Use of Fourier series in the analysis of discontinuous periodic structures. *Journal of the Optical Society of America a-Optics Image Science and Vision* **13**, 1870-1876 (1996).

120 Moharam, M. G., Grann, E. B., Pommet, D. A. & Gaylord, T. K. Formulation for Stable and Efficient Implementation of the Rigorous Coupled-Wave Analysis of Binary Gratings. *Journal of the Optical Society of America a-Optics Image Science and Vision* **12**, 1068-1076 (1995).

121 Guérout, R., Lussange, J., Chan, H., Lambrecht, A. & Reynaud, S. Thermal Casimir force between nanostructured surfaces. *Physical Review A* **87**, 052514 (2013).

122 Takei, K. *et al.* Nanoscale InGaSb heterostructure membranes on Si substrates for high hole mobility transistors. *Nano Letters* **12**, 2060-2066 (2012).

123 Kim, J. *et al.* Ultra-thin flexible GaAs photovoltaics in vertical forms printed on metal surfaces without interlayer adhesives. *Applied Physics Letters* **108**, 253101 (2016).

124 Liu, X. L., Zhao, B. & Zhang, Z. M. M. Enhanced near-field thermal radiation and reduced Casimir stiction between doped-Si gratings. *Physical Review A* **91**, 062510 (2015).

125 Liu, X. L., Zhang, R. Z. & Zhang, Z. M. Near-field radiative heat transfer with doped-silicon nanostructured metamaterials. *International Journal of Heat and Mass Transfer* **73**, 389-398 (2014).

BIOGRAPHICAL SKETCH

Payam Sabbaghi was born in Tehran, Tehran Province, Iran in 1985. He received his Bachelor's degree from University of Tehran in 2008 in Mechanical Engineering. Next, he received his Master's degree from University of Tehran in 2011 in Mechanical Engineering. Payam entered the School for Engineering of Matter, Transport and Energy at Arizona State University in Spring 2014 as a PhD student, and he has been studying in Dr. Liping Wang's group in the area of nanoscale radiative heat transfer since Spring 2015. His research is concentrated on experimental demonstration of near-field radiation and theoretical modeling of near-field thermophotovoltaic conversion systems. During his PhD study, he has published two first-authored journal papers in *International Journal of Heat and Mass Transfer*, and *Journal of Quantitative Spectroscopy and Radiative Transfer*, with one leading-authored manuscript under review and one to submit, in addition to another three co-authored manuscripts or journal publication. He gave two oral talks at *MRS Spring Meeting & Exhibit* in April 2017 and at *International Mechanical Engineering Congress and Exposition* in November 2019. He has also co-authored over 4 conference presentations, such as *9th International Symposium on Radiative Transfer*, *3rd International Workshop on Nano-Micro Thermal Radiation*, and *ASME 2019 International Mechanical Engineering Congress and Exposition*. As a head graduate teaching assistant, Payam taught the fundamentals of Applied Computational Fluid Dynamics in Fall 2015 and Experimental Mechanical Engineering labs in Spring 2016 and Spring 2018.